Reconstructing Cosmological Density and Velocity Fields

Helen Elizabeth Mary Valentine

Doctor of Philosophy
The University of Edinburgh
2000

This thesis is my own composition except where indicated in the text.

February 6, 2001

My thesis is dedicated to my grandparents, Rimmelion and Derek Valentine.

Acknowledgements

Whilst writing my thesis, I often felt like I was banging my head against a series of small walls. So here I'd like to thank those people who made it that little bit easier.

First of all I had better thank my family for their support during the last 4 years. My Dad also deserves a mention for proof reading my thesis. Special thanks to my sister Becky and my cousin Claire for providing tea, cake and sympathy, often at short notice. Also thanks to Becky for suggesting how to fit the phrase "A series of small walls" into my thesis. I didn't think describing the structures seen in the PSCz as resembling a series of small walls would get past the examiners.

I want to thank everyone in the department for bearing with me whilst I was ill. Thanks to my supervisors Will Saunders and Andy Taylor for their (sometimes contradictory) help and advice. For numerous helpful discussions, I'd like to thank Alan Heavens, Kenton D'Mellow and Peter Watts.

Thanks to Ross McLure, Matthew Horrobin, Lousia Nolan, Ali Higgins and James Manners for being my office mates and sharing many constructive hours with me. R7 is a unique working environment, and I shall certainly miss it.

And last, but not least, thanks to all those who occasionally took my mind off reconstructing velocity fields, particularly Murray and Rachael Gibbins, Craig Grattan, Sarah Heal, and my cats Nicky and Pickles.

"'Well?' said Trillian.

'Er ... what does the Z mean?' said Zaphod.

'Which one?'

'Any one."'

The Hitch-hikers Guide to the Galaxy

Douglas Adams

Contents

List of Figures

List of Tables

Abstract

I present a new quasi–linear method for reconstructing cosmological density and velocity fields from all-sky redshift surveys. The method is used to reconstruct the velocity field, dipole, bulk flows and distortion parameter $\beta = \Omega^{0.6}/b$ from the PSCz survey.

Analytic expressions for the cosmic variance and shot noise uncertainties on the reconstructed velocity field are presented. It is found that the uncertainties are reduced if reconstruction is carried out in the Local Group frame. The uncertainty on the dipole is also found.

A generalized version of the Path Interchange Zel'dovich Approximation (PIZA) is presented. PIZA is a simple Lagrangian reconstruction method based on the Zel'dovich Approximation and the Least Action Principle, which reconstructs cosmological fields given the present day real space positions of galaxies. The generalizations take account of redshift space distortions, incomplete sky coverage, and the selection function. The method can be used to estimate β from radial velocities, bulk flows and the dipole.

Generalized PIZA has been tested using a set of PSCz-like simulations. The reconstructed radial peculiar velocity field is compared with that of the simulation and that reconstructed by linear theory.

The generalized PIZA is applied to the *IRAS* PSCz Survey. The dipole, bulk velocities and peculiar velocity field, and the derived value of β are presented. The Local Group is found to have an average displacement of $1225 kms^{-1}$ in the direction of (l,b)=(264°,42°). From this it is found that $\beta = 0.512 \pm 0.141$.

Chapter 1

Introduction

It is generally believed that the present day structures and motions in the Universe are due to the growth of initially small inhomogeneities present in the early Universe by gravitational instability. The velocities of galaxies in the present Universe can tell us much about the Universe both today and in the past. Running the motions of galaxies backwards into the past, we can study the initial conditions of the Local Universe. The velocities of galaxies may be used to measure the mean density of the Universe Ω_0, or the distortion parameter $\beta = \frac{\Omega_0^{0.6}}{b}$, where b is the bias parameter. The Local Group has a velocity of $627 \pm 22 kms^{-1}$ toward (l,b)=($276° \pm 3°$, $30° \pm 3°$) (e.g. Lineweaver *et al.* 1996). This is known as the cosmological dipole. It is believed that this motion is caused by the gravitational attraction of other galaxies. By studying the dipole we can test this assumption and also measure the value of β.

In this Thesis, I present a generalized reconstruction method, based on the PIZA method of Croft and Gaztañaga (1997), for application to realistic redshift surveys. I discuss some of the errors introduced into the reconstructed velocity field. My new reconstruction method is applied to the PSCz redshift survey, and the results of this reconstruction are presented.

In this Chapter I discuss the background cosmology which will be needed in the rest of this Thesis. I describe the reasons why the reconstruction of cosmological fields is un-

dertaken, and I discuss the results of some previous reconstructions. I will also describe in detail some reconstruction methods which have paved the way for the reconstruction method I have developed for this Thesis.

1.1 Basic Cosmology

The current standard cosmological model is the Hot Big Bang model - a homogeneous, isotropic universe, whose evolution is governed by the Friedmann equations obtained from General Relativity, and which began in a Hot Big Bang some 13 billion years ago. This model rests on four observations: the expansion of the Universe (e.g. Hubble 1929) ; the CMB, whose origin is the hot dense plasma that existed in the Universe at times earlier than 10^{-13} seconds (e.g. Dicke *et al.* 1965; Penzias and Wilson 1965); the isotropy of the CMB (e.g. Smoot *et al.* 1992) ; the primeval abundance of Deuterium, Helium-3, Helium-4 and Lithium (e.g. Schramm 1991).

1.1.1 The Cosmological Principle

The Cosmological Principle is fundamental to cosmology. It states that on average the Universe is statistically homogeneous and isotropic. There are no preferred places in the Universe. The Copernican Principle states that we do not have a privileged place in the Universe. Combined with the isotropy of the Universe, this implies that the Universe is homogeneous (e.g. Peacock 1999), as is shown in Figure 1.1. The density in the sphere centered at point A which passes through C and E has constant density because of the isotropy about A. Due to the isotropy about point B, the sphere centred on B also has constant density. This implies that the shaded region is homogeneous. The point B may be moved along the line which passes through A and D, and the shaded region will again have constant density. Since A and B are random points, they may be placed anywhere in the Universe, thus implying that the Universe as a whole is homogeneous.

The isotropy of the Universes has been demonstrated observationally, for example the

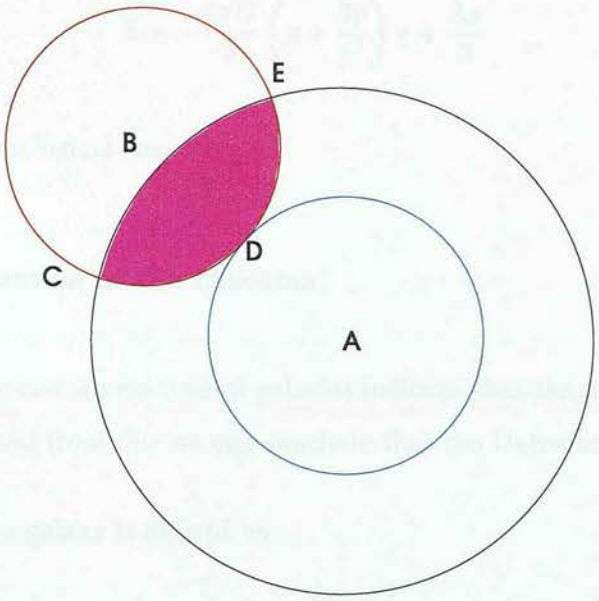

Figure 1.1: Diagram to show how the isotropy of the density about 2 points implies homogeneity in the Universe (Peacock 1999).

deviations from isotropy in the CMB are one part in 10^5. The temperature of the microwave background was found by COBE to be $T = 2.728 \pm 0.004K$ (Smoot *et al.* 1992).

1.1.2 The Robertson-Walker Metric

A universe which is isotropic, homogeneous, expanding and obeys special relativity must be described by a metric whose form can be inferred (up to an arbitrary function) entirely by symmetry arguments. This metric is the Robertson-Walker metric. Its form is

$$ds^2 = c^2dt^2 - a^2(t)\left[\frac{dr^2}{1-kr^2} + r^2(d\theta^2 + \sin^2\theta d\phi^2)\right] \tag{1.1}$$

where a is the expansion factor and k is the curvature constant (e.g. Peebles 1993).

Substituting this into the Einstein equations gives the Friedmann equations, which give the dynamics of the expansion factor:

$$\dot{a}^2 = \frac{8}{3}\pi G\rho a^2 - kc^2 + \frac{\Lambda a^2}{3} \tag{1.2}$$

$$\ddot{a} = -\frac{4\pi G}{3}\left(\rho + \frac{3p}{c^2}\right)a + \frac{\Lambda a}{3} \tag{1.3}$$

where Λ is the cosmological constant.

1.1.3 The Expansion of the Universe

Observations of the radial velocities of galaxies indicate that the majority of them are receding from us, and from this we can conclude that the Universe is expanding.

The redshift, z, of a galaxy is defined as

$$1 + z = \frac{\lambda_0}{\lambda_e} = \frac{1}{a} \tag{1.4}$$

where λ_e is the wavelength of the light emitted by the galaxy and λ_0 is the wavelength of the light observed. This redshift is interpreted as a Doppler shift of the light emitted by the galaxy.

The expansion of the Universe is characterised by the famous Hubble Law (Hubble 1929)

$$v = H_0 d = cz \tag{1.5}$$

where

$$H = \frac{\dot{a}}{a} \tag{1.6}$$

is the Hubble parameter, H_0 its value today, and $a = a(t)$ is the scale factor.

Independent measurements of redshift and distance show that the two are proportional to impressive accuracy. This has been demonstrated with observations of high redshift supernovae which are found to obey the Hubble law from $z = 0.003$ to $z \simeq 1$ (Perlmutter *et al.* 1999).

1.1.4 The Hubble Constant

There has been much controversy about the value of the Hubble constant ever since Hubble first (over-) estimated its value to be around 500kms^{-1}Mpc^{-1}. In the early 1980s H_0 was measured to be either in the range 50 to 60 kms^{-1}Mpc^{-1} (e.g. Sandage and Tammann 1985) or in the range 90 to 110 kms^{-1}Mpc^{-1} (e.g. de Vaucouleurs 1986). The differences were due to discrepancies in the local distance scale, extinction estimates, corrections made for Malmquist bias, and weights given to different methods for estimating H_0.

The Hubble Space Telescope Extragalactic Distance Scale Key Project was set up with the aim of measuring H_0 to $\pm 10\%$ by finding accurate Cepheid distances to galaxies. The latest measurement from the HST Key Project is $H_0 = 71 \pm 6$kms^{-1}Mpc^{-1} (Ferrarese *et al.* 2000).

1.2 The Density of the Universe

1.2.1 Universe with no cosmological constant

In a Universe with no cosmological constant, the factor deciding whether the Universe will expand forever or not is the density ρ. If the density is very low, the Universe will continue expanding forever, in this case the Universe is open. If the density is high enough, gravity will be able to halt the expansion, and the Universe will contract, in which case the Universe is closed. The dividing line between the open and closed universe occurs at the so called critical density, where the curvature K is zero, defined as

$$\rho_{crit} = \frac{3H_0^2}{8\pi G}\,, \tag{1.7}$$

(e.g. Peacock 1999 Chapter 3).

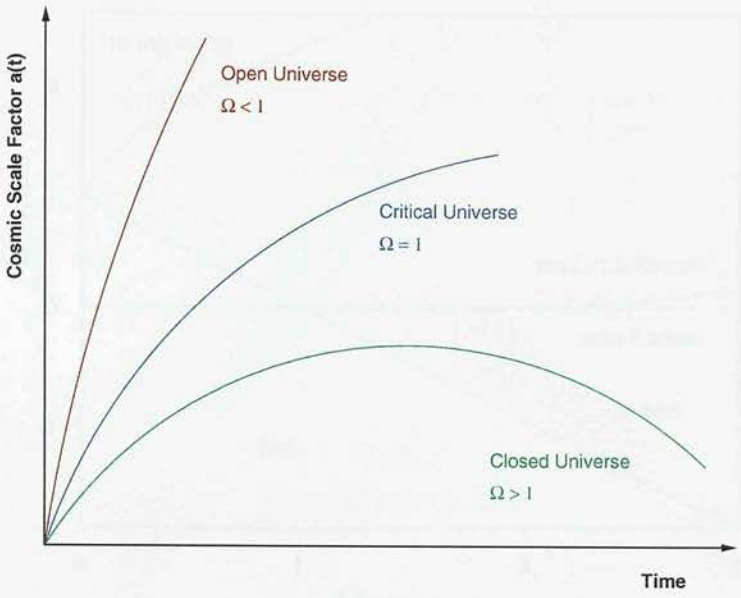

Figure 1.2: The scale factor a as a function of time.

The density parameter is defined as

$$\Omega = \frac{\rho}{\rho_{crit}}. \tag{1.8}$$

The conditions for open and closed universes then become $\Omega < 1$ for an open universe and $\Omega > 1$ for a closed universe (see Figure 1.2).

Using the Friedmann equations, the redshift dependence of Ω may be found,

$$\Omega(z) = \frac{\Omega_0(1+z)}{(1+z\Omega_0)}\,. \tag{1.9}$$

1.2.2 Universe with a cosmological constant

Current observations indicate that the density of matter in the Universe is $\Omega_m \sim 0.3$, with a cosmological constant of $\Omega_\Lambda \sim 0.7$. This has been supported by observations of Type 1a supernovae, e.g. Perlmutter *et al.* 1999 and Riess *et al.* 1998, and the CMB, e.g. Tegmark (1999), Lineweaver (1998).

Figure 1.3 (from Peacock 1999) shows the $\Omega_M - \Omega_\Lambda$ plane. The consequences for the Universe depending on the combination of Ω_M and Ω_Λ are indicated. Figure 1.4

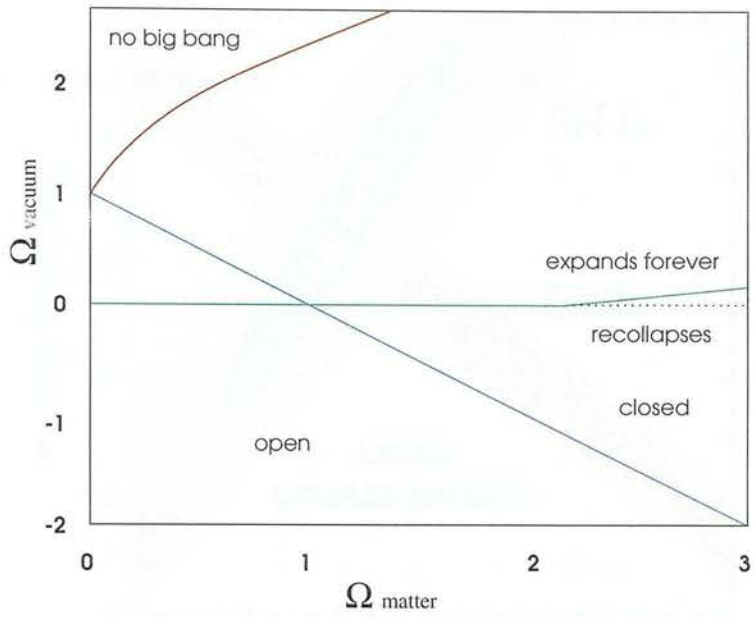

Figure 1.3: The $\Omega_M - \Omega_\Lambda$ plane and the consequences for the Universe (Peacock 1999).

(Tegmark *et al.* 1998) shows the $\Omega_M - \Omega_\Lambda$ plane, with the combination of parameters allowed by observations of supernovae 1a and the CMB indicated.

1.3 Dark Matter

1.3.1 Evidence for Dark Matter

There is evidence that most of the mass density in the Universe is dark and may only be detected through its gravitational attraction (e.g. see review Trimble 1987). For example, the rotation curves of spiral galaxies are flat even in the outer parts of the visible galaxy. This suggests that the mass is less centrally concentrated than the light, with the mass being distributed in a dark halo.

The mass of galaxies may be estimated using their rotation curves or velocity dispersions. For galaxy clusters, the virial theorem may be used to estimate their mass. On larger scales, the mass of superclusters may be estimated using the Cosmic Energy Equation (e.g. Peebles 1993, §20), which relates the velocity dispersion of galaxies to the correlation function. On even larger scales, the velocity field may be used to

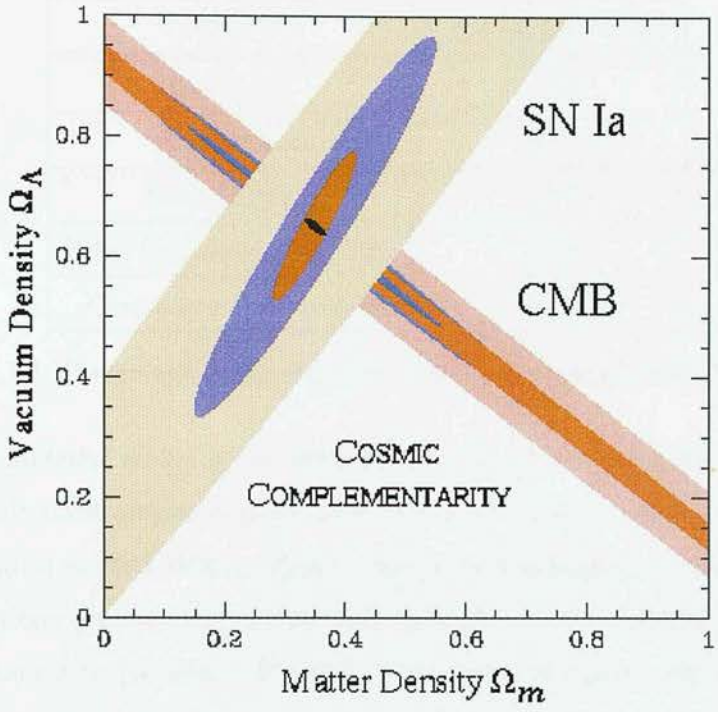

Figure 1.4: Combination of Ω_M and Ω_Λ allowed by observations of SN1a and the CMB (Tegmark *et al.* 1998).

estimate the mass in a given region, and hence find an estimate of Ω.

1.3.2 Dark Matter Candidates

The physical nature of the dark matter remains unknown. Since it is dark, we know that it does not interact strongly with photons. Most of the dark matter is non-baryonic, as nuclear burning limits mean that not enough baryonic matter can be formed to make up all of the dark matter (e.g. Peacock 1999 §12.4).

Baryonic Dark Matter

The abundance of helium rules out all of the dark matter being baryonic. If the baryon density is too large, nucleosynthesis produces too much He and not enough H^2. Nucleosynthesis puts a limit on Ω_b of $0.01 \leq \Omega_b h^2 \leq 0.015$ (Schramm and Turner 1998).

Component	Percentage of Total
Neutrinos	~0.3
Bright Stars	0.5
Total Baryons	5
Relic Elementary Particles	35
Cosmological Constant	60

Table 1.1: Percentage composition of matter and energy in the Universe.

The baryonic material makes up of order 10% or less of the mass density of the universe. Baryonic dark matter may be in the form of brown dwarfs or white dwarfs, collectively known as MACHOs or Massive Astrophysical Compact Halo Objects. Various collaborations are searching for possible MACHOs in the Galactic Halo, e.g. The MACHO collaboration (Alcock *et al.* 1993), which finds only about 20% of the halo can be MACHOs.

Non-baryonic Dark Matter

There are various different candidates for non-baryonic dark matter.

Hot dark matter (HDM) has a dominant particle with a mass of 10 - 100 eV. With hot dark matter, the first structures to form are of supercluster scale, which then fragment to form smaller structures on galaxy scales. Possible HDM candidates are neutrinos and anti-neutrinos, the most popular candidate being the tau neutrino. There has been recent evidence for a non-zero neutrino mass e.g. the Super Kamiokande group (Fukuda *et al.* 1999) found evidence for muon neutrino oscillation, which is the changing of neutrino type as the neutrino passes through space or matter and which can only occur if the neutrino has mass. HDM particles decouple from the radiation when relativistic, and have roughly the same number density as the photons. One drawback with HDM is that galaxy formation simulations using HDM form galaxies too late. This is because galaxy formation with HDM is top-down, forming supercluster scale objects first and then fragmenting to form galaxies. HDM cannot be the only non-baryonic component present at the epoch of galaxy formation.

Cold dark matter (CDM) particles have lower thermal velocities than hot dark matter particles. Possible CDM candidates include black holes and primordial black holes, axions, neutralinos, and WIMPs (Weakly Interacting Massive Particles). CDM particles decouple when they are non-relativistic, and obviously have lower thermal velocities than HDM particles. The particles may have weaker interactions than neutrinos.

Mixed dark matter is a combination of hot and cold dark matter particles (e.g. Taylor and Rowan-Robinson 1992). The HDM suppresses the power spectrum on small scales.

Obviously a non-zero cosmological constant would solve some of the discrepancy between the measured values of Ω and that predicted by inflation, $\Omega = 1$ (see Section 1.5). This, however, cannot solve the entire dark matter problem on all scales as Λ is unable to cluster.

Another less favoured class of dark matter candidate is that of topological defects. These include domain walls, cosmic strings and monopoles (e.g. Peacock 1999, Chapter 10).

1.4 Biasing

Dark matter may dominate the mass density of the universe, but it is the galaxies that we see. Theories of galaxy formation can most easily predict the statistics of the distribution of dark matter; the relative distribution of galaxies and dark matter remains an important unknown in interpreting the observed large-scale structure of galaxies. Comparisons of galaxy velocity and density fields may constrain the parameter β, but this cannot be used to estimate Ω_0 unless the bias parameter is known.

The distribution of galaxies need not trace the underlying density field. We need some way to connect the galaxies and the mass density. Kaiser (1984) suggested that clusters of galaxies could be biased relative to galaxies: galaxy clusters are likely to be produced where the initial density contrast is high - producing higher than average density of clusters and stronger correlation function of clusters than galaxies. It was

then thought that the same might be true of galaxies and the underlying mass density. If the clustering of galaxies is stronger than that of the dark matter this would decrease the measurement of Ω from dynamical studies. The simplest biasing model is that of linear biasing, i.e.

$$\delta_{galaxies}(r) = b\delta_{DM}(r) \tag{1.10}$$

This could of course cause problems with $b > 1$ as the density contrast is bounded by $\delta \geq -1$, and is therefore only really applicable in the linear regime. A more realistic biasing model would give the density of galaxies as an unknown non-linear function of the mass density. Non-linear biasing is discussed in Dekel and Lahav (1999).

Different populations of galaxies must also be biased relative to each other. For example, elliptical galaxies make up about 15% of galaxies in the field but are dominant in cluster cores. Therefore not all galaxy types can be exact tracers of the underlying mass distribution. This relative biasing of different galaxies types has been studied by various authors, for example Kaiser and Lahav (1989) found that $b_{IRAS} = 1.6$ and $b_{optical} = 2.0$.

1.5 Inflation

It is believed that there was a phase in the early Universe when the expansion of the Universe was quasi-exponential. This inflationary period was first suggested by Guth (1981). The basic idea is that in the early Universe there was a phase when the vacuum energy dominates the energy density of the Universe for a time, driving an exponential de Sitter phase of expansion. During this phase, a tiny smooth patch of the Universe can be inflated to an enormous size, and as the curvature radius increases exponentially, the region becomes spatially flat.

Inflation has been reviewed in various papers, including Liddle and Lyth (1993) and Turner (1997).

1.5.1 Problems with the Big Bang Theory

Inflation solves various problems associated with the Big Bang Theory. These problems include the following:

- The Horizon Problem. The horizon at last scattering subtends an angle of about $1°$, meaning that regions further apart than this angle are causally disconnected. However, we know from the isotropy of the CMB that regions much further apart than this have the same temperature. This apparent problem, that regions which have not had time to communicate with each other have the same properties, may be solved by a period of exponential expansion.

- The Flatness/Fine Tuning Problem. To get $\Omega \sim 1$ today requires a fine tuning of Ω in the past. In the matter dominated era,

$$\frac{1}{\Omega(z)} - 1 = (1+z)^{-1}\left[\frac{1}{\Omega_0} - 1\right] \tag{1.11}$$

  At the Planck epoch, the deviation of Ω from 1 is less than 1 part in 10^{60}.

  If $\Omega \neq 1$, then as the curvature is becoming important now, how did the universe know to have a deviation from $\Omega = 1$ so that this would happen?

- The Structure Problem. Obviously the universe is not precisely homogeneous. One of the problems in cosmology is the origin of the structures we observe today. It is generally assumed that these structures grew by gravitational instability from some initial perturbations. But where did these perturbations come from? In the inflationary scenario, quantum fluctuations present in the very early universe are frozen in, and then once inflation has finished they grow by gravitational instability.

- The Expansion Problem. How was the expansion of the Universe set in motion? Classical cosmology gives no reason for the expansion other than the fact that it was expanding in the past and it continues to do so now.

1.5.2 Inflation Theory

The general condition for inflation is $\ddot{a} > 0$. Given the second Friedmann equation (1.3), this means that

$$\rho + 3p < 0 \tag{1.12}$$

This can occur with quantum fields, the simplest being a Scalar Field. The equation of motion of the field is

$$\ddot{\phi} + 3H\dot{\phi} - \nabla^2\phi + V'(\phi) = 0 \tag{1.13}$$

describing the field in a potential well, V.

The energy of the field is

$$\rho = \frac{1}{2}\dot{\phi}^2 + V(\phi) + \frac{1}{2}(\nabla\phi)^2$$

and the pressure of the field is

$$p = \frac{1}{2}\dot{\phi}^2 - V(\phi) - \frac{1}{6}(\nabla\phi)^2$$

These give

$$\rho + 3p = 2\dot{\phi}^2 - 4V(\phi)$$

which satisfies the inflation condition equation (1.12) if $\dot{\phi}^2 < V$. There is no one model of inflation. Each model specifies the shape of the potential.

The slow roll approximation is that $|\ddot{\phi}|$ is negligible in comparison with $|3H\dot{\phi}|$ and $|dV/d\phi|$. The condition that $V \gg \dot{\phi}^2$ may be rewritten as

$$\epsilon \equiv \frac{m_p^2}{16\pi}\left(\frac{V'}{V}\right)^2 \ll 1 \tag{1.14}$$

where $V' = dV/d\phi$ and m_p is the Planck mass. Differentiating this equation and using the slow roll approximation again gives

$$\eta \equiv \frac{m_p^2}{8\pi}\left(\frac{V''}{V}\right) \ll 1 \tag{1.15}$$

The tilt of the spectrum of density fluctuations, the deviation of the spectral index from 1, is defined as

$$\text{tilt} = 6\epsilon - 2\eta \tag{1.16}$$

(e.g. Peacock 1996).

Inflation sets the universe expanding towards an effective k=0 state by using the negative pressure of the vacuum energy. After inflation, some way to return to a radiation dominated Universe is needed. A suggested mechanism is reheating, the conversion of the vacuum energy into radiation (Albrecht *et al.* 1982).

The universe rolls down the potential to the minimum and then undergoes a phase transition back to the normal equation of state and expands as usual. Quantum fluctuations in the scalar field are the seeds of present day structures (Bardeen *et al.* 1983). Most inflationary models generate adiabatic perturbations, and hence density perturbations at the end of inflation. The amplitude of density perturbations at horizon scales is nearly scale invariant.

Expansion damps out initial irregularities, so we get homogeneity and isotropy, and volumes are always causally connected at early times. Inflation also initiates the expansion of the universe and dilutes any monopoles, thus solving the problem that these have never been observed.

1.5.3 Predictions of Inflation

Inflation makes various predictions which may be tested. These include the following.

- A flat universe. Through the Friedmann equation it implies that the total energy density is always equal to the critical density, although it does not say what form the energy takes. Thus we have the condition that

$$\Omega_M + \Omega_\Lambda + \Omega_\gamma = 1 \tag{1.17}$$

- A nearly scale-invariant spectrum of Gaussian density perturbations - they arise from quantum fluctuations in the field that drives inflation and are stretched to

huge size by inflation. Fluctuations in the linear gravitational potential are scale invariant (independent of length scale), as are the horizon crossing amplitudes of the density perturbations.

- A nearly scale-invariant spectrum of gravitational waves which arise from quantum fluctuations in the metric. Waves of all wavelength cross the horizon with the same dimensionless strain amplitude.

1.5.4 Tests of Inflation

The generic predictions of inflation models, such as the spatial flatness of the Universe and Gaussian density perturbations with a scale invariant Zel'dovich power spectrum, may be tested observationally. The anisotropy in the CMB may be used to set limits on the energy scale of inflation, and to measure the power spectrum (e.g. Smoot 1991). Redshift surveys and peculiar velocity surveys may also be used to test predictions of inflation by comparing them with inflationary n-body simulations and by calculating the power spectrum and the mean density of the Universe (e.g. Dekel 1991).

Another prediction of inflation is the background of gravity waves. The coupling between these gravity waves and the tilt contributes to the CMB anisotropy, and observations of this coupling would be evidence that inflation, or something like inflation, occurred. The most convincing test would be a direct detection of the predicted flat spectrum of gravity waves in the local Universe, but currently this is unfeasible (Peacock 1996).

1.6 Growth of Perturbations

The perturbations that survive recombination are either isocurvature or adiabatic. These two types of perturbation are produced in different ways, as follows. Starting with uniform distributions of matter and radiation, one way to perturb the density is to compress or expand volume elements adiabatically. This changes the matter density and the photon number density by the same factor, and so affects the energy densities

of matter and radiation differently,

$$\rho_{radiation} \propto a^{-4} \tag{1.18}$$

$$\rho_{matter} \propto a^{-3} \tag{1.19}$$

and so

$$\delta_r = \frac{4}{3}\delta_m \tag{1.20}$$

These are adiabatic perturbations. Most inflationary models produce adiabatic perturbations.

The alternative is to perturb the entropy density but not the energy density, giving isocurvature perturbations. In this case the total density remains homogeneous, and there is no perturbation to the spatial curvature. This case corresponds to the matter density being perturbed with the radiation density having a very small perturbation.

After decoupling, perturbations of both types grow via gravitational instability. There are two different ways in which structures can form - top-down and bottom-up. With top-down structure formation, the first structures to form are of supercluster size, and these fragment to form smaller structures. In bottom-up structure formation, the first structures to form are small, and these then coalesce to form larger structures. Whether structures form bottom-up or top-down depends on the fluctuation spectrum.

The CMB shows deviations from isotropy which are interpreted as being due to tiny fluctuations in the initial density field. Gravity amplifies the contrast between over- and under-densities, eventually leading to the structures that we see today.

1.6.1 Gravitational Instability

We start with the equations of mass continuity, force and gravitation in proper coordinates. Here we ignore the effects of relativity and pressure.

$$\frac{\partial \rho}{\partial t} + \nabla(\rho \boldsymbol{v}) = 0 \tag{1.21}$$

$$\frac{\partial \boldsymbol{v}}{\partial t} + (\boldsymbol{v} \cdot \boldsymbol{\nabla})\boldsymbol{v} + \nabla\phi = 0 \tag{1.22}$$

$$\nabla^2\phi = 4\pi G\rho \tag{1.23}$$

Here ρ is the mass density field, $\boldsymbol{v}$ is the velocity field, ϕ is the gravitational potential.

In a comoving frame, which moves with the general expansion of the Universe, using linear perturbation theory, the first two equations become

$$\frac{\partial \delta}{\partial t} + \frac{1}{a}\boldsymbol{\nabla} \cdot \boldsymbol{v} = 0 \tag{1.24}$$

and

$$\frac{\partial \boldsymbol{v}}{\partial t} + \frac{\dot{a}}{a}\boldsymbol{v} + \frac{1}{a}\nabla\phi = 0 \tag{1.25}$$

where $\delta = \frac{\rho - \rho_0}{\rho_0}$ is the fractional density contrast.

Eliminating $\boldsymbol{v}$ gives

$$\frac{\partial^2 \delta}{\partial t^2} + 2\frac{\dot{a}}{a}\frac{\partial \delta}{\partial t} = 4\pi G\rho\delta \tag{1.26}$$

The general solution to this equation is

$$\delta = A(\boldsymbol{r})D_1(t) + B(r)D_2(t) \tag{1.27}$$

$D_1(t)$ is the growing mode and $D_2(t)$ is the decaying mode. The growing mode is the case where the velocity and density fields are correlated, with velocities pointing towards over-densities, and the decaying mode the case where the fields are anti-correlated.

In the case where $\Omega_m = 1$ and $\Omega_\Lambda = 0$, we have $D_1(t) \sim t^{2/3}$ and $D_2(t) \sim t^{-1}$.

1.6.2 Relations between Density and Velocity Fields in Linear Theory

We start with Equation (1.27). At late times the growing mode dominates, and in linear theory may be written as $\delta = A(\boldsymbol{r})D_1(t)$. The time derivative of this equation may be written

$$\frac{\partial \delta}{\partial t} = \frac{\delta}{D_1(t)}\dot{D}_1(t) \tag{1.28}$$

Substituting this into Equation 1.24, gives

$$\nabla \cdot \boldsymbol{v} = -a\delta H_0 \frac{d \ln D_1}{d \ln a} \tag{1.29}$$

Note that $\frac{d \ln D_1}{d \ln a} = f(\Omega_0) \simeq \Omega_0^{0.6}$ and we get (e.g. Peebles 1980)

$$\nabla \cdot \boldsymbol{v} = -aH_0 \delta f(\Omega_0) \tag{1.30}$$

We now wish to invert Equation (1.30) to find $\boldsymbol{v}$ in terms of δ. We start with the Laplacian of the gravitational potential,

$$\nabla^2 \phi = 4\pi G a^2 (\rho(\boldsymbol{r}) - \rho_b) \tag{1.31}$$

where ρ_b is the background density. Perturbations to the gravitational potential are caused by perturbations about the background density.

The solution to this is (cf. electrostatics)

$$\phi(\boldsymbol{r}) = -Ga^2 \int d^3r' \frac{\rho(\boldsymbol{r}') - \rho_b}{|\boldsymbol{r}' - \boldsymbol{r}|} \tag{1.32}$$

We also have the gravitational acceleration

$$\boldsymbol{g}(\boldsymbol{r}) = -\frac{\nabla \phi(\boldsymbol{r})}{a} \tag{1.33}$$

which becomes

$$\boldsymbol{g}(\boldsymbol{r}) = Ga \int d^3r' (\rho(\boldsymbol{r}') - \rho_b) \frac{(\boldsymbol{r}' - \boldsymbol{r})}{|\boldsymbol{r}' - \boldsymbol{r}|^3} \tag{1.34}$$

The density may be written as

$$\rho(\boldsymbol{r}) = \rho_b(1 + \delta(\boldsymbol{r})) = \rho_b + \rho_b \delta \tag{1.35}$$

If we substitute this in we get

$$\boldsymbol{g}(\boldsymbol{r}) = Ga\rho_b \int d^3r' \delta(\boldsymbol{r}') \frac{(\boldsymbol{r}' - \boldsymbol{r})}{|\boldsymbol{r}' - \boldsymbol{r}|^3} \tag{1.36}$$

So we have the relation between $\boldsymbol{g}$ and δ, now we need a relation between $\boldsymbol{g}$ and $\boldsymbol{v}$.

Starting again with Equations (1.31) and (1.35) we have

$$\nabla^2 \phi = 4\pi G a^2 \rho_b \delta \tag{1.37}$$

or

$$\nabla \cdot (\nabla \phi) = 4\pi G a^2 \rho_b \delta \tag{1.38}$$

Using Equation (1.33) we get

$$-\nabla \cdot \boldsymbol{g} = 4\pi G a \rho_b \delta \tag{1.39}$$

Substituting in for δ from Equation (1.30) we get

$$\boldsymbol{v}(\boldsymbol{r}) = \frac{H_0 f}{4\pi G \rho_b} \boldsymbol{g}(\boldsymbol{r}) \tag{1.40}$$

and substituting in from Equation (1.36) gives, in proper coordinates,

$$\boldsymbol{v}(\boldsymbol{r}) = \frac{H_0 f}{4\pi} \int d^3 r' \delta \frac{(\boldsymbol{r}' - \boldsymbol{r})}{|\boldsymbol{r}' - \boldsymbol{r}|^3} \tag{1.41}$$

1.7 The Zel'dovich Approximation

The Zel'dovich Approximation (Zel'dovich 1970) is a linear first order Lagrangian perturbation theory with respect to particle displacements, and is an important extension of linear theory.

Zel'dovich made the assumption that the difference between the Lagrangian position $\boldsymbol{q}$ and the Eulerian position $\boldsymbol{x}$ of a particle in a gravitating system is separable in time and space.

$$\boldsymbol{x}(\boldsymbol{q}) = \boldsymbol{q} + D_1(t) \boldsymbol{\psi}(\boldsymbol{q}) \tag{1.42}$$

Here $\boldsymbol{q}$ is the initial position, $D_1(t)$ is the growing mode in linear theory and ψ determines the direction and amplitude of the velocity field and is set by the initial conditions. This mapping between the initial and final positions is unique providing that trajectories do not cross. The Zel'dovich approximation works well when

$$\frac{\delta \rho}{\rho} \ll 1 \tag{1.43}$$

Differentiating Equation (1.42) gives the peculiar velocity

$$\boldsymbol{u} = \dot{D}_1(t) \psi(\boldsymbol{q}) \tag{1.44}$$

We now want to find the perturbed density field $\rho(q,t)$ given that $x = q + D\psi$.

If we let $\rho(x,t) = \bar{\rho}$, we have

$$\rho(q,t) = \bar{\rho}\left|\frac{\partial q_j}{\partial x_k}\right| \tag{1.45}$$

Given Equation (1.42),

$$\frac{\partial}{\partial q_j}(q_k + D\psi_k) = \delta_{jk} + D\frac{\partial \psi_k}{\partial q_j} \tag{1.46}$$

so we have

$$\rho(q,t) = \bar{\rho}\left|\delta_{jk} + D\frac{\partial \psi_k}{\partial q_j}\right|^{-1} \tag{1.47}$$

The Jacobian is a real symmetric matrix and can be diagonalised to give an orthogonal set of principal axes.

The perturbed density field $\rho(q,t)$ is (e.g. Efstathiou 1990)

$$\rho(q,t) = \frac{\bar{\rho}}{(1 - D\lambda_1)(1 - D\lambda_2)(1 - D\lambda_3)} \tag{1.48}$$

where λ_1, λ_2 and λ_3 are eigenvalues describing the contraction and expansion of matter along the principal axes. When one of the 3 brackets becomes zero, the density will become infinite - collapse to a sheet along one of the principal axes. The first non-linear structures to form in an initially linear density field will be sheets or pancakes.

1.8 Redshift Space

The proper distance to a galaxy in terms of the comoving distance is given by $\boldsymbol{r} = a\boldsymbol{x}$. Differentiating this we get,

$$\dot{\boldsymbol{r}} = \dot{a}\boldsymbol{x} + a\dot{\boldsymbol{x}}$$

$$\dot{\boldsymbol{r}} = H\boldsymbol{r} + \boldsymbol{v} \tag{1.49}$$

The first term on the right hand side arises from the expansion of the Universe, the second is the galaxy's peculiar velocity. If we use $\dot{\boldsymbol{r}}$ as the velocity in Hubble's law to estimate the distance to a galaxy, the resulting distance is in *Redshift Space*. Without the peculiar velocity of the galaxy, the distance is in *Real Space*.

1.8.1 Redshift Space Distortions

Within a virialized cluster of galaxies, the galaxies have peculiar velocities around 1000kms^{-1}. Since the cluster members are at approximately the same position in real space, then these peculiar velocities will cause the galaxy positions to be stretched along the line of sight in redshift space. This causes the familiar fingers of god seen in redshift space maps.

Galaxies outside the cluster will have peculiar velocities falling onto the cluster, so galaxies on the far side will have negative peculiar velocities and galaxies on the near side have positive peculiar velocities. This causes a compression along the line of sight in redshift space. The theory of redshift space distortions was reviewed in Hamilton (1998).

Figure 1.5 shows idealised redshift distortions, with the arrows indicating the peculiar velocities of galaxies falling towards a spherical overdensity. The top diagram shows the case on large scales where the peculiar velocity of the infalling shell is small compared to its radius. This leads to the shell appearing to be squashed in redshift space. The middle diagram shows this squashing effect on a smaller scale for a shell at turnaround where the peculiar infall velocity cancels the Hubble expansion. In this case, the shell appears to be collapsed to a single line in redshift space. On even smaller scales shells have turned around and start to collapse, leading to them appearing turned inside out in redshift space. This leads to the familiar fingers of god.

The over-density δ^s in redshift space is related to the over density δ in real space by the linear redshift space operator (Hamilton 1998)

$$\delta^s = \boldsymbol{S}\delta \tag{1.50}$$

where

$$\boldsymbol{S} = 1 + \beta(\partial_r^2 + 2r^{-1}\partial_r)\boldsymbol{\nabla}^{-2} \tag{1.51}$$

where $\partial_r = \frac{\partial}{\partial r}$.

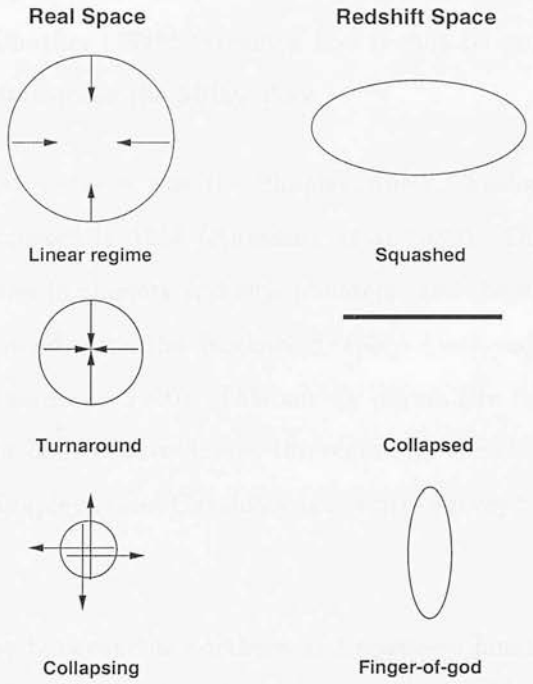

Figure 1.5: Redshift space distortions (Hamilton 1997). On large scales spherical overdensities appear squashed. At turnaround, an overdensity appears to be collapsed. On smaller scales, fingers of god are seen. The observer is located towards the bottom of the page.

1.9 Galaxy Redshift Surveys

1.9.1 History of Galaxy surveys

Hubble and other workers in the 1920s began to realize that the "spiral nebulae" were in fact other galaxies like the Milky Way (e.g. Hubble 1925). Öpik (1922) found that the distance to M31 implied that it was outside the Milky Way, and concluded that it must be another galaxy of stars. This was confirmed by Hubble's (1926) identification of Cepheids in M31. Charlier (1925) explained how it may be concluded that the spiral nebulae are stellar systems like the Milky Way.

One of the first galaxy surveys was the Shapley-Ames Catalog (Shapley and Ames 1932), which was completed in 1956 (Humason *et al.* 1956). This survey revealed the concentration of galaxies in clusters and superclusters, and the empty regions or voids. This survey was extended with the Revised Shapley-Ames catalog (Sandage 1978 , Yahil, Sandage and Tammann 1980). This survey covers the region $cz < 4000 kms^{-1}$ and does not cover the Zone of Avoidance, the region on the sky obscured by our own galaxy. The Revised Shapley-Ames Catalog was the first survey to cover a large fraction of the sky.

There is an asymmetry between the northern and southern hemispheres due to nearby galaxies being preferentially located in the north galactic hemisphere towards the centre of the Local Supercluster in the Supergalactic Plane. The Local Supercluster was first discovered by de Vaucouleurs (1953, 1958).

Galaxy surveys have been successful in mapping the large scales structure in the Universe, and in discovering new superclusters and voids. They also have the power to answer many of the questions in modern cosmology.

1.9.2 Three-Dimensional Redshift Surveys

In this short review of redshift surveys I will concentrate on all-sky surveys at low redshifts $z \leq 0.1$. This subject is reviewed in much more detail in Strauss and Willick (1995). These survey the Local Universe, where distances are small compared with the horizon distance, and look back times are small. At these distances, relativistic effects are mostly unimportant and the Hubble law is a good approximation. However, this situation is complicated by galaxy peculiar velocities.

Galaxy surveys are important for cosmography, for topological studies, and for making dynamical predictions of the peculiar velocity field in the Local Universe. The ideal redshift survey samples a fair volume of the Universe, with a well defined selection function. The selection function is defined as the expected number of galaxies seen at distance r above the flux limit in the absence of clustering, and is used to correct for the fact that galaxies in a flux limited sample represent an increasingly smaller proportion of the parent population at larger distances - we have to do this if we are to use the galaxies as tracers of the general galaxy distribution. The selection function is related to the luminosity function, which gives the number density of galaxies of luminosity L per unit luminosity. We assume that the luminosity function is universal - we assume that the subset of galaxies luminous enough to enter a flux limited sample at a given redshift are fair tracers of the full population of galaxies.

1.9.3 IRAS Redshift Surveys

Redshift surveys require a predefined sample of targets. Many surveys have used one of the IRAS catalogues. The Infra-Red Astronomical Satellite flew in 1983 and undertook a full sky survey with $\sim 1'$ resolution in 4 wave-bands, centred at 12, 25, 60 and 100 μm (Beichman *et al.* 1988).

Samples of galaxies taken from IRAS catalogues are well suited for full sky surveys as far infrared is not impeded by galactic extinction, and they extend the sky coverage down to $\sim 5°$ from the Galactic Plane. At very low galactic latitudes IRAS surveys

are limited by effects in the IRAS catalogues and by confusion with galactic sources. This gives 80% to 90% sky coverage. IRAS surveys have uniform and unmatched sky coverage, and have the advantages of depth, uniformity and completeness, and have reliable almost all-sky coverage which is needed in dynamical studies.

Most galaxies detected by IRAS are late type galaxies whose infrared emission can be accounted for by normal star formation. They avoid dense regions, which is likely because collisions and the ram pressure of intracluster gas have stripped the galaxies of the gas that fuels bursts of star formation and high far infrared luminosity. IRAS samples are deficient in ellipticals and S0 galaxies, which have little dust or star formation. This of course means that the number density of galaxies in the cores of rich clusters of galaxies, where ellipticals predominate, is systematically underestimated. Well known cluster cores such as Virgo and Hydra are less conspicuous in the far infrared than in the optical.

IRAS based redshift surveys include the 2Jy and 1.2 Jy surveys, QDOT and PSCz. The 2Jy Survey (Strauss *et al.* 1992a) contains $\sim$ 2600 galaxies to a flux limit of 1.936 Jy at $60\mu m$ and covers 88% of the sky. The 1.2Jy Survey (Fisher 1992) contains $\sim$ 5300 galaxies. The QDOT survey (Rowan-Robinson *et al.* 1990, Lawrence *et al.* 1999) contains $\sim$ 2300 galaxies selected at random at a rate of 1 in 6 from PSC with a flux limit of 0.6 Jy, and is deeper and sparser than the previous 2 surveys. The most recent IRAS survey is the Point Source Redshift survey (PSCz; Saunders *et al.* 2000). I will discuss this survey in more detail in Chapter 5. A survey that extends in to the Zone of Avoidance is the Behind The Plane survey (Saunders *et al.* 1999) which is an extension to the PSCz survey into the Galactic Plane.

1.10 Reconstruction of Cosmological Fields

Reconstruction methods use the available information about the fields using certain assumptions to find the missing information - they reconstruct the fields from what is known about them. Cosmological velocity and density fields may be reconstructed using the radial velocity information from a galaxy redshift survey. In order to do this,

assumptions must be made about the way the peculiar velocity field is produced, the relations between the velocity and density fields, and the galaxies and the underlying mass distribution.

The study of large scale dynamics started with the confirmation (e.g. Smoot *et al.* 1977) of the dipole in the CMB, and the development of redshift independent distance measurements (e.g. Tully and Fisher 1977). The first models of the large scale velocity field were very simple models of several "attractors", e.g. Virgocentric infall (Aaronson *et al.* 1982) and the Great Attractor (Lynden-Bell *et al.* 1988). These toy models have largely been replaced by non-parametric models where the full velocity field is reconstructed based on gravitational flows properties , and the mass density fluctuation field recovered from the velocity.

1.10.1 Motivation

There are various reasons as to why so much effort has been put into reconstructing velocity and density fields from galaxy surveys.

The reconstructed fields may be compared with those actually observed. In the case of reconstructing a galaxy redshift survey, this will be done by reconstructing the peculiar velocity field and then comparing it with the observed peculiar velocity field. This may place constraints on the parameter $\beta = \frac{\Omega_0^{0.6}}{b}$, the biasing scheme and theories of structure formation. This comparison may also be used to test the assumptions used in the reconstruction.

The peculiar velocities of galaxies are generated by the gravity of all gravitating matter, not just the visible matter, so studying these peculiar velocities is a way of studying the total distribution of matter in the Universe. We may also be able to test whether or not the observed galaxies trace the underlying distribution of matter, i.e. whether light traces mass.

Comparison of the Local Group peculiar velocity with the Cosmic Microwave Background dipole can also put constraints on the value of β. As we believe that the dipole

is caused by the motion of the Local Group due to the surrounding matter, comparing the direction of the dipole with the direction of the Local Group's reconstructed velocity tests the assumption of gravitational instability. Alignment of these directions implies that the CMB dipole is indeed due to the gravitational attraction of nearby galaxies.

We also want to put constraints on the method of structure formation. For example, did the structures we see today form by gravitational instability from initial Gaussian fluctuations? It is possible to reconstruct the initial density field, which may be tested for Gaussianity. This initial density field may then be evolved forward in time and compared with the present day density field to test the assumptions made in the reconstruction.

The Zone of Avoidance may cause problems in dynamical reconstructions. Extinction in the Galactic Plane means that most galaxy surveys are incomplete in this region. We need as complete a map of the density field as possible as we want to test gravitational instability theory or to measure β. If the unsurveyed regions are unfilled there will be systematic errors in the velocity field. No galaxies in the regions does not mean no galaxies in the real world, but most reconstruction methods will treat these regions as voids and produce spurious outflows. There are various methods which have been used to overcome this problem. One option is to fill the empty regions with the average density of the survey. An alternative solution is to interpolate the density field from higher galactic latitudes. For example, Yahil *et al.* (1991) linearly interpolated the density field across the Galactic plane in their reconstruction of the 2 Jy survey. Scharf *et al.* (1992) used a more complex interpolation scheme, where the angular distribution of galaxies was expanded in spherical harmonics and extrapolated into the Galactic plane. Lahav *et al.* (1994) expanded the galaxy distribution in spherical harmonics, used a Wiener filter to recover the harmonics in the Zone of Avoidance and, given these 4π harmonics, reconstructed the 4π density field. In the case of IRAS galaxies, extinction in the Zone of Avoidance is less important, and the region may be surveyed. For example, the BTP survey (Saunders *et al.* 2000) extends the PSCz survey into the Galactic plane.

1.11 Results from previous reconstructions

Early estimations of cosmological parameters from galaxy catalogues used angular data only. For example, Meiksin and Davis (1986) found the gravitational dipole to be around 30° away from the CMB dipole and $\Omega_0 \sim 0.5$.

Other reconstructions of the gravitational dipole used surveys with incomplete sky coverage.

- Davis and Huchra (1982) used the CfA and Revised Shapley-Ames catalogues and found $\beta = 0.38 - 0.74$.
- Yahil *et al.* (1986) used *IRAS* galaxies out to $R = 200h^{-1}Mpc$ and found the dipole to be $26 \pm 10°$ away from the CMB dipole, and $\Omega_0 = 0.85 \pm 0.16$.

More recent reconstructions have used full sky galaxy catalogues.

- Rowan-Robinson *et al.* (1990) reconstructed the gravity dipole using the QDOT survey. They concluded that convergence of the dipole occurred beyond $cz = 10000kms^{-1}$ and that $\beta = 0.82 \pm 0.15$.
- Yahil *et al.* (1991) used the 2Jy Survey to reconstruct the peculiar velocity field and found $\beta = 0.74 \pm 0.15$ at the 2σ level.
- Kaiser *et al.* (1991) used a linear theory reconstruction method applied to QDOT out to $R = 150h^{-1}Mpc$. Comparing the reconstructed field with observed peculiar velocities, they found that $b_{IRAS}\Omega_0^{0.6} = 1.16 \pm 0.21$.
- Strauss *et al.* (1992c) reconstructed the acceleration of the Local Group, and found the dipole to be $18 - 28°$ away from the CMB dipole. With a maximum likelihood fit to the growth of the dipole, they found that $\beta = 0.4 - 0.85$ at the 1σ level.
- Dekel *et al.* (1993) compared *IRAS* galaxies from the 2Jy survey and the mass density field from POTENT (Dekel *et al.* 1999), and found that $\beta_{IRAS} = 1.28^{+0.75}_{-0.59}$.

- Hudson (1993) reconstructed the gravitational dipole using optical galaxies. Assuming that the dipole converges within $cz = 8000 kms^{-1}$ he found $\beta = 0.80^{+0.21}_{-0.13}$, and that the dipole is $28 - 32°$ away from the CMB dipole.

- Davis *et al.* (1996) compared the Mark III peculiar velocity catalogue (Willick *et al.* 1997) and the 1.2Jy survey (Fisher 1992). They found a most likely value of $\beta = 0.4 - 0.6$.

- Webster *et al.* (1997) reconstructed the density and velocity fields of the 1.2 Jy Survey using a Wiener reconstruction method with spherical harmonics and spherical Bessel functions. They made a qualitative comparison of the velocity field with the Mark III catalogue, and found reasonable agreement. They found the reconstructed dipole within $5000 kms^{-1}$ to be 13° away from the CMB dipole.

- Baker *et al.* (1998) reconstructed the peculiar velocity field using the Optical Redshift Survey (Santiago *et al.* 1995). In order to match the reconstructed field with Mark III, they found that $\beta \leq 0.45$.

Reconstructions of the peculiar velocity field and the gravitational dipole using the PSCz survey are discussed in Chapter 5.

1.12 Reconstruction methods

There are various complications in reconstructing the peculiar velocity field from a redshift survey. We have to assume a biasing model to relate the galaxy and underlying mass density fields. The distances of galaxies in the survey are in redshift space rather than real space. Real galaxy surveys also have the problems of incomplete sky coverage and limited depth.

The growth and evolution of structures in the Universe may be studied using two types of methods: Eulerian methods that solve the gravitational instability equations, and Lagrangian methods that follow individual galaxy displacements. These methods may be used to deduce the velocity field from the density field and vice versa.

If gravity is responsible for the growth of large scale structure, then the velocity field contains, in principle, all the information required for recovering the initial conditions. In particular, the linearized large scale mass density field can be extracted from the peculiar velocity field using the continuity equation, and the motions traced back to the initial state using a method such as the Zel'dovich Approximation. It is not possible to simply run the gravitational instability equations back in time as the decaying mode in equation 1.27 will blow up any residual noise in the present day fields.

1.12.1 Linear Theory Methods

A common Eulerian reconstruction method is that which uses linear perturbation theory applied to the gravitational instability equations. This method is used in the following reconstructions.

Yahil *et al.* (1991)

This is an iterative method which may be applied to galaxy redshift surveys. The selection function and density in the sample volume are found first, and then the gravity on the galaxies is calculated. The peculiar velocities of the galaxies and of the Local Group may then be found. The method iterates to find the real space positions and peculiar velocities given the redshift space positions. To damp oscillatory behaviour, after the first iteration the peculiar velocity is the average of that of the present and previous iteration. The galaxy distances are then updated and the process is repeated. It was found that 8 iterations were sufficient for convergence. The method was tested on N-body simulations in Davis *et al.* 1991. The results for the galaxy distribution and the inferred density field were presented in Strauss *et al.* 1992b.

Kaiser *et al.* (1991)

In this method, galaxies are first binned in cells in redshift space. The cell volumes are corrected for parts that are not covered by the survey. The radial selection function

and radial density run are then found, along with the density contrast $\Delta(z)$. This is corrected for the distortion by peculiar velocities using linear theory. $\Delta(z)$ is then transformed to $\Delta(r)$ using a transformation from Kaiser (1987).

Fisher *et al.* (1995)

This is a non-iterative method giving a minimum variance estimate of the density field in real space. The cosmological fields are expanded in orthogonal radial (spherical Bessel) and angular (spherical harmonic) functions. Galaxy peculiar velocities introduce coupling of the radial harmonics in redshift space but leave the angular modes unaffected. In transform space this may be described by a distortion matrix which can be computed analytically with linear theory. Shot noise on the density field is removed using a Wiener filter. The real space density harmonics may then be found from the redshift space harmonics. The minimum variance harmonics of the peculiar velocity and potential fields are related to those of density field by simple linear transformations. The method was applied to the 1.2 Jy survey.

1.12.2 Least Action Methods

Hamilton's principle, that the action is minimized during the evolution of a collection of particles under gravity, has been used in many reconstructions. These methods are known as least action or numerical action methods. They consider relatively few galaxies as they are computationally expensive.

Peebles (1989)

In this paper, the orbits of Local Group members are traced back in time. It is assumed that mass is concentrated around galaxies, that mass concentrations developed at $z \gg 1$ and galaxy motions grew by gravity as they moved away from a roughly uniform initial mass distribution. It is also assumed that galaxies at high redshift have negligible peculiar velocities. Trial orbits are chosen to minimize the action given the observed

positions of the galaxies. It was found that the predicted velocities generally resemble the observations although there were some discrepancies.

Peebles (1990)

This paper concentrates on the motions of very nearby galaxies, and is tested on 6 dwarf galaxies in the Local Group. The orbits are again predicted using the numerical action method. It uses particles with the masses of galaxies to trace the evolution of the mass distribution back in time to an epoch when galaxies could not have existed with their present structures. At higher redshifts, the particles model the early growth of departures from homogeneity on galaxy scales. The method uses well known distances to predict redshifts for the galaxies.

Peebles (1994)

This paper uses the numerical action method to find the relative motions of the nearby galaxies and groups of galaxies treated as tracers of the mass within 4Mpc. This uses more galaxies than previous papers, and studies the motions in more detail. The method works for predicting redshifts given distances or vice versa. This paper predicts redshifts given distances.

Peebles (1995)

In this paper, the numerical action method is used slightly differently. In the above papers, particle orbits were approximated as linear combinations of smooth functions of time. In this paper, the orbits are parametrized at a discrete set of world times. This has the advantages that it is computationally faster and is better adapted to sharply bending orbits. This method is applied to the motions of the outer dwarf spheroidal companions of the Milky Way.

Shaya, Peebles and Tully (1995)

In this paper, action principle solutions for the motions of galaxies within 3000kms^{-1} are found, given the galaxy redshifts. The galaxies are from various sources including the 1.2Jy Survey (Fisher *et al.* 1995) and the Nearby Galaxy Catalog (Tully 1988). The motions are fully non linear solutions for the orbits of mass tracers. As usual it is assumed that the peculiar velocities at high redshift are negligible.

Dunn and Laflamme (1993)

In this paper, it is shown that the method of Peebles underestimates Ω for CDM simulations. It neglects the effect of CDM particles that are not halo members and which are distributed uniformly in the early stages of the Universe, and thus reduces the force on the particles which will eventually form haloes. The method in this paper is used to determine the trajectories of the galaxies in the Local Group and the more massive galaxies in the local neighbourhood. The resulting angular momentum for the Local Group is deduced, and the tidal force on the Local Group and its galaxies is studied.

Branchini and Carlberg (1994)

In this paper, it is found that the least action principle succeeds in qualitatively reconstructing galaxy trajectories, but it fails to describe the dynamics on Local Group scales in an $\Omega_0 = 1$ universe. The authors conclude that the least action principle applied to the Local Group cannot rule out a value of $\Omega_0 = 1$ on Local Group scales, but that it is a powerful reconstruction method for larger systems of galaxies.

Nusser and Branchini (2000)

This paper develops a Fast Action Minimization - a fast method for recovering the past orbits of galaxies using the least action principle given the present distribution of the

galaxies. The orbits are expanded in a set of orthogonal time dependent base functions satisfying the boundary conditions at the initial and final times (i.e. negligible initial peculiar velocities, present day positions). The conjugate gradient method is then used to locate the minimum of the action. As this method is much faster than previous least action methods, the number of galaxies it may be applied to may be increased by more than an order of magnitude. The method is used to reconstruct peculiar velocities.

Weinberg (1992) and Narayanan and Weinberg (1999)

These methods are based on Gaussianization, which is introduced in Weinberg (1992), and they are applied to redshift surveys. This method assumes that the initial density distribution function is Gaussian and that the rank order of densities is likely to be preserved even when non linear effects skew the distribution function. The rank order of the densities at different points is conserved, and the densities are assigned to fit a Gaussian form. The smoothed galaxy density field found from a redshift survey is mapped monotonically to smoothed initial conditions using a Gaussian probability distribution. The resulting initial conditions may be evolved forward in time with an N-Body code and compared with observations to test the assumptions made.

In Narayanan and Weinberg, a hybrid reconstruction method is developed, which combines Gaussianization with the methods of Nusser and Dekel and Gramman (which are described below). This method is then tested on mocks of the PSCz and ORS surveys.

1.12.3 Zel'dovich Approximation Methods

Lagrangian methods include those using the Zel'dovich approximation (Zel'dovich 1970) which was suggested as a way to study the evolution of structure in the weakly nonlinear regime.

Direct numerical integration of the growth of density fluctuation equation fails because the decaying mode amplifies any residual noise present in the final density field - any method for recovering the initial density fluctuations must overcome this problem. To

operate a gravitational time machine one must therefore control the decaying modes or eliminate them altogether. One way to do this is by using the Zel'dovich Approximation, which is naturally restricted to the evolution of the growing mode.

Nusser and Dekel (1992)

This paper introduces a quasi-linear method for recovering the growing mode of the initial fluctuations of a cosmological gravitating system from the present day large scale peculiar velocity or density field. The velocity potential field is extracted from observed velocities or from the density field assuming velocity field is irrotational. Using the Zel'dovich Approximation with no orbit crossing, the potential is traced back in time by integrating the Zel'dovich-Bernoulli equation. The linear velocity and density fields are computed from the linear potential by differentiation. The method was applied to POTENT velocity potential and the density field from the 2Jy Survey.

Taylor and Rowan-Robinson (1993)

This method is based on non-linear non-local transformations of the density field, assuming a curl-free velocity field. It extends the Kaiser *et al.* method of formulating a set of dynamical and continuity equations to describe the formation and distortion of structure in redshift space. The galaxy redshift distribution is used to construct a smooth redshift space density field, which is Fourier transformed. This is used to calculate the potential field, which is used to put boundary conditions on the cube to isolate the density distribution from periodic boundary conditions. The isolated density field is used to calculate the velocity field in Fourier space. The velocity field is radially projected and iteratively used to solve the linear continuity equation and the dynamical equations of motion. This is repeated until a stable solution is found. The method was then applied to QDOT to get a real space density field.

Giavalisco *et al.* (1993)

In this paper, the Zel'dovich Approximation is generalized to a series expansion of arbitrary accuracy in the non linear regime. The coefficients of the expansion are determined from the action principle. The Zel'dovich Approximation and the approach of Peebles are combined to describe the orbits of galaxies for laminar flow in the quasi-linear regime. This method is found to be more rapidly convergent than previous non linear approximations, and to provide a practical means of determining particle orbits even for highly non linear perturbations. However, they found that it is difficult to determine galaxy trajectories when there has been significant orbit mixing, as in the real Universe.

Suspereggi and Binney (1994)

This paper uses the Giavalisco *et al.* Eulerian method to trace backwards in time the cosmic density and velocity fields and to determine accurately the current epoch velocity field from the current epoch density field or vice versa. They conclude that the application of the method to real observational data appears to be feasible but it is computationally costly.

Gramman (1993a,b)

These papers aim to improve on the method of Nusser and Dekel. An Eulerian continuity equation in the Zel'dovich Approximation is derived. This can trace the evolution of the gravitational potential of the universe more exactly than reconstructions based on the Zel'dovich-Bernoulli equation. The gravitational potential is obtained from a redshift survey, and its evolution is traced back in time by integrating the continuity equation in the Zel'dovich Approximation. The initial linear density and velocity fields may then be determined by the differentiation of the initial gravitational potential. In the second paper, second order Lagrangian perturbation theory is used to calculate an analytical expression relating density to velocity in a gravitating system.

Croft and Gaztañaga (1997)

A method combining the Zel'dovich approximation and the least action principle is the Path Interchange Zel'dovich approximation (PIZA). Using the Zel'dovich approximation, the least action solution is that which minimizes the total mean square particle displacements between initial and final galaxy positions. The method takes a final galaxy distribution in real space and reconstructs the initial positions, giving the galaxy displacements and hence peculiar velocities. PIZA is discussed in Chapter 3.

Monaco and Efstathiou (1999)

This paper describes a method called ZTRACE which reconstructs the initial conditions from a full sky survey. It is based on a self consistent solution of the growing mode of gravitational instabilities according to the Zel'dovich Approximation and higher order in Lagrangian perturbation theory. The method is iterative and finds an approximation to the initial density field for any given set of cosmological parameters. It also reconstructs the real space positions and peculiar velocities. They find that it can recover the probability distribution function of the initial conditions to high precision except for the tail at $\delta \geq 1$. They find that going to second order is simple, but, from tests with N-Body simulations, this does not give any significant improvement in reconstruction accuracy.

1.13 Thesis Outline

The outline of this thesis is as follows.

In Chapter 2 I discuss sources of errors on the reconstructed velocity field. Expressions for the cosmic variance and shot noise errors in both the CMB and Local Group rest frames are derived. The error on the cosmological dipole is also derived, again in the CMB and Local Group frames. These errors are found as a function of position in the reconstructed volume, and the results are presented.

In Chapter 3 I introduce the Path Interchange Zel'dovich Approximation reconstruction method. I discuss the problems caused by redshift space distortions, reference frames, incomplete sky coverage, and the survey selection function, which arise when applying PIZA to realistic redshift surveys. I present a generalized version of PIZA, which takes into account these problems and which may be used to reconstruct the cosmological density and velocity fields from realistic redshift surveys. The method is applied to a set of PSCz-like simulations, and the reconstruction of the velocity field and of the distortion parameter β are tested. The PIZA reconstructions are also compared with linear theory reconstructions of the simulations. The results of these comparisons are presented, and the accuracy of the generalized PIZA is discussed.

In Chapter 4 I discuss further problems associated with the survey selection function which arise when applying PIZA to flux limited redshift surveys. An extension to the generalized PIZA method, which takes account of the selection function in detail is presented. This method is tested on the PSCz simulations, and the results are presented. It is found that this method does not improve significantly on the generalized PIZA presented in Chapter 3.

In Chapter 5 I apply the new generalized PIZA method, as described in Chapter 3, to the PSCz redshift survey. I discuss the survey and the results of other reconstructions of the PSCz velocity field, dipole and derived β. The results of the PIZA reconstruction are presented, with the velocity field, the dipole and bulk flows. Values for the distortion parameter β derived from the dipole and the velocity field are presented. The reconstructed PSCz bulk flow and dipole are compared with the MK III data set and the SFI data set, and the results are presented.

In Chapter 6 I present my conclusions.

Chapter 2

Incompleteness in Reconstructed Velocity Fields

In this Chapter I discuss the uncertainties in the reconstruction of the velocity field, from a redshift survey. There are two main sources of uncertainty: shot noise, due to the discrete sampling of galaxies in the survey, and cosmic variance, due to only a finite volume being available.

In Section 2.1 the subject of the uncertainty in the velocity field is introduced, and general expressions for the uncertainty are derived.

In Section 2.2 the uncertainty on the velocity field due to cosmic variance is discussed. Expressions for the radial, transverse and total rms cosmic variance in the CMB and Local Group frames are derived as a function of position within the survey. The effects of structures both internal and external to the survey are studied, and expressions for the cosmic variance in both cases are derived. Cross-correlation terms for the radial and transverse components of the cosmic variance are also derived.

In Section 2.3, the uncertainty due to shot noise is discussed. Expressions for the radial, transverse and total rms shot noise are derived as a function of position in the survey, and in the Local Group and CMB frames.

In Section 2.4 the uncertainty on the dipole is discussed, and the combined uncertainty on the reconstructed dipole due to cosmic variance and shot noise is found.

The results in this Chapter may be used in a maximum likelihood analysis of reconstructed velocity fields. They are used in Chapter 5 to assess the errors on the velocity field reconstructed from the PSCz survey. This work has been published in Taylor and Valentine (1999).

2.1 Uncertainty in $v(r)$

The velocity field as reconstructed from a redshift survey is subject to errors from such effects as incomplete sky coverage, a finite survey radius and the random sampling of survey galaxies from the actual galaxy distribution. The reconstructed field will be unaffected by large mass concentrations beyond the boundary of the survey and within regions not covered by the survey, which will of course affect the actual velocity field. The reconstructed velocity field will also be affected by the random sampling of galaxies.

The errors due to these effects must be quantified in order to find how much we can rely on the reconstructed velocity field, for example for estimating the parameter β. Previously, other authors have estimated these errors using multiple reconstructions and measuring the differences in velocity fields between reconstructions. The galaxies in the Local Group have an average velocity of magnitude around $600 kms^{-1}$, if we assume that the galaxies in the local neighbourhood are typical of galaxies in the rest of the Universe, then we can assume that typical galaxy velocities are of the same order.

In this Chapter, the variance and cross-correlation functions of the velocity field are found. These terms give the difference between the true and reconstructed fields, due to effects such as sampling variance, and internal and external structures not in the survey. The true field is found assuming linear theory and Poisson sampling. When reconstructing the velocity field from a survey, we would obviously wish to minimize these terms.

In Section 2.2 below, the uncertainty on the velocity field due to cosmic variance is derived in terms of spherical harmonics and spherical Bessel functions. This method of expressing cosmological fields in terms of radial and angular functions has been used in various reconstruction methods, for two reasons. Firstly, this makes reconstruction in real space simpler, as redshift distortion by peculiar velocities is a radial effect and will not change the angular functions. Secondly, it makes sense to use spherical coordinates when working with redshift surveys with spherical geometry.

Various authors have used the spherical harmonic formalism in the reconstruction of redshift surveys. Regös and Szalay (1989) applied spherical harmonic analysis to the peculiar velocity field. Fisher, Scharf and Lahav (1994) used spherical harmonics with a Gaussian window function in the radial direction to analyse redshift distortions and measure Ω. Fisher *et al.* (1995) decomposed the density, velocity and potential fields with spherical harmonics and spherical Bessel functions. Heavens and Taylor (1995) used the spherical harmonic method to reconstruct the real space power spectrum and β.

Recently, the spherical harmonic methods have been applied to the PSCz survey. Schmoldt *et al.* (1999a) extended the Fisher *et al.* (1994) method. They applied it to the PSCz survey to reconstruct the density and velocity fields, and found that $\beta = 0.7 \pm 0.5$. Tadros *et al.* (1999) extended the method of Heavens and Taylor (1995) and, applying it to the PSCz, found that $\beta = 0.47 \pm 0.16$.

In Section 2.4 the total error on the dipole due to cosmic variance and shot noise is derived. Cosmological dipoles have been studied in detail by a number of authors. Kaiser and Lahav (1989) calculated the acceleration of the Local Group using both optical and *IRAS* galaxies. They compared these dipoles with CDM linear theory predictions. Lahav *et al.* (1990) studied the convergence of the acceleration of the Local Group and its alignment with the CMB dipole. They calculated the expected dipole given theoretical models of large scale structure, and compared it with the observed acceleration of the Local Group. Similarly, Juszkiewicz *et al.* (1990) compare the observed *IRAS* dipole with that predicted by models of structure formation.

Peacock (1992) showed that when calculating the dipole from a galaxy survey, for Gaussian density fields, neglecting mass outside the survey has a large effect on the reconstructed dipole velocity. Strauss *et al.* (1992c) calculated the acceleration on the Local Group using the 1.2 Jy survey. They estimated the shot noise variance on this reconstructed dipole due to the finite sampling of galaxies in the survey.

2.1.1 Uncertainty in $v(r)$: theory

In linear theory the velocity field is related to the density field by

$$\boldsymbol{v}(\boldsymbol{r}) = \frac{H_0 \Omega_0^{0.6}}{4\pi} \int d^3r' \Delta(\boldsymbol{r}') \frac{(\boldsymbol{r} - \boldsymbol{r}')}{|\boldsymbol{r} - \boldsymbol{r}'|^3} \tag{2.1}$$

where

$$\Delta(\boldsymbol{r}') = \frac{n - \bar{n}}{\bar{n}} \tag{2.2}$$

is the density contrast and n is the number density of galaxies. See Section 1.6.2 for a derivation of this equation.

In order to estimate the uncertainty on the velocity field, the variance on the velocity must be calculated. To simplify things, let

$$\boldsymbol{h}(\boldsymbol{r} - \boldsymbol{r}') \equiv \frac{(\boldsymbol{r} - \boldsymbol{r}')}{|\boldsymbol{r} - \boldsymbol{r}'|^3}. \tag{2.3}$$

The variance on the velocity is then

$$\left\langle v^2(r) \right\rangle = \left\langle \int d^3r' \Delta(\boldsymbol{r}') \boldsymbol{h}(\boldsymbol{r} - \boldsymbol{r}') \cdot \int d^3r'' \Delta(\boldsymbol{r}'') \boldsymbol{h}(\boldsymbol{r} - \boldsymbol{r}'') \right\rangle$$

$$= \int d^3r' d^3r'' \boldsymbol{h}(\boldsymbol{r} - \boldsymbol{r}') \cdot \boldsymbol{h}(\boldsymbol{r} - \boldsymbol{r}'') \left\langle \Delta(\boldsymbol{r}') \Delta(\boldsymbol{r}'') \right\rangle . \tag{2.4}$$

So an expression for $\langle \Delta(\boldsymbol{r}') \Delta(\boldsymbol{r}'') \rangle$ is needed. Using Equation (2.2),

$$\left\langle \Delta(r') \Delta(r'') \right\rangle = \left\langle \frac{n' - \bar{n}}{\bar{n}} \cdot \frac{n'' - \bar{n}}{\bar{n}} \right\rangle = \frac{\left\langle (n' - \bar{n})(n'' - \bar{n}) \right\rangle}{\bar{n}^2}$$

$$= \frac{1}{\bar{n}^2} \left(\left\langle n' n'' \right\rangle - \left\langle n' \bar{n} \right\rangle - \left\langle n'' \bar{n} \right\rangle + \bar{n}^2 \right)$$

but $\langle n'\bar{n}\rangle = \langle n''\bar{n}\rangle = \bar{n}^2$, so

$$\left\langle \Delta(r')\Delta(r'')\right\rangle = \frac{\langle n'n''\rangle}{\bar{n}^2} - 1. \tag{2.5}$$

It is assumed that the distribution of galaxies may be treated as a Poisson process picking galaxies from an underlying galaxy density field. The probability of an event in a Poisson distribution is given by

$$P(n|\lambda) = \frac{\lambda^n e^{-\lambda}}{n!} \tag{2.6}$$

where λ is the mean number of times an event occurs in n trials and is given by

$$\lambda = \langle n\rangle = \bar{n}(1+\delta). \tag{2.7}$$

Thus P is the probability of finding n galaxies given the mean λ.

Start with

$$\left\langle n(\boldsymbol{r}')n(\boldsymbol{r}'')\right\rangle = \bar{n}\delta_D(\boldsymbol{r}'-\boldsymbol{r}'') + \left\langle n(\boldsymbol{r}')\right\rangle\left\langle n(\boldsymbol{r}'')\right\rangle \tag{2.8}$$

and substitute in for $\langle n'\rangle$ and $\langle n''\rangle$ using Equation (2.7),

$$\begin{aligned}\left\langle n(\boldsymbol{r}')n(\boldsymbol{r}'')\right\rangle &= \bar{n}\delta_D(\boldsymbol{r}'-\boldsymbol{r}'') + \bar{n}^2\left\langle(1+\delta(\boldsymbol{r}')(1+\delta(\boldsymbol{r}'')\right\rangle \\ &= \bar{n}\delta_D(\boldsymbol{r}'-\boldsymbol{r}'') + \bar{n}^2(1+\left\langle\delta(\boldsymbol{r}')\delta(\boldsymbol{r}'')\right\rangle).\end{aligned} \tag{2.9}$$

This equation states that the correlation of a set of points consists of an uncorrelated Poisson term (shot noise), and a smooth correlated term due to the density field.

Combining this with Equation (2.5),

$$\begin{aligned}\left\langle \Delta(\boldsymbol{r}')\Delta(\boldsymbol{r}'')\right\rangle &= \frac{1}{\bar{n}^2}\left[\bar{n}\delta_D(\boldsymbol{r}'-\boldsymbol{r}'') + \bar{n}^2(1+\left\langle\delta(\boldsymbol{r}')\delta(\boldsymbol{r}'')\right\rangle) - \bar{n}^2\right] \\ &= \frac{1}{\bar{n}}\delta_D(\boldsymbol{r}'-\boldsymbol{r}'') + \left\langle\delta(\boldsymbol{r}')\delta(\boldsymbol{r}'')\right\rangle.\end{aligned} \tag{2.10}$$

Given Equation (2.4), the variance on the velocity is then

$$\langle v^2 \rangle = \int d^3r' d^3r'' \boldsymbol{h}(\boldsymbol{r}-\boldsymbol{r}')\boldsymbol{h}(\boldsymbol{r}-\boldsymbol{r}'') \left(\frac{1}{\bar{n}} \delta_D(\boldsymbol{r}'-\boldsymbol{r}'') + \langle \delta(\boldsymbol{r}')\delta(\boldsymbol{r}'') \rangle \right). \tag{2.11}$$

The correlation function is given by $\xi(\boldsymbol{r}'-\boldsymbol{r}'') = \langle \delta(\boldsymbol{r}')\delta(\boldsymbol{r}'') \rangle$ and so

$$\langle v^2 \rangle = \int d^3r' d^3r'' \boldsymbol{h}(\boldsymbol{r}-\boldsymbol{r}')\boldsymbol{h}(\boldsymbol{r}-\boldsymbol{r}'') \left(\frac{1}{\bar{n}} \delta_D(\boldsymbol{r}'-\boldsymbol{r}'') + \xi(\boldsymbol{r}'-\boldsymbol{r}'') \right). \tag{2.12}$$

Thus the variance on the velocity has two terms, due to shot noise and density.

The term due to density is

$$\langle v^2 \rangle_\delta = \int d^3r' d^3r'' \left| \boldsymbol{h}(\boldsymbol{r}-\boldsymbol{r}') \right| \left| \boldsymbol{h}(\boldsymbol{r}-\boldsymbol{r}'') \right| \xi(\boldsymbol{r}'-\boldsymbol{r}''). \tag{2.13}$$

This is the cosmic variance term, and will be discussed further in Section 2.2.

The shot noise term is

$$\langle v^2 \rangle_{SN} = \int d^3r' \left| \boldsymbol{h}(\boldsymbol{r}-\boldsymbol{r}') \right|^2 \frac{1}{\bar{n}(r')} \tag{2.14}$$

where $\bar{n}$ is the selection function. The shot noise errors are discussed later in Section 2.3.

2.2 Cosmic Variance

The velocity field may be written in terms of the unsmoothed density field,minus the usual pre-factors and denoting the density contrast by the usual δ, as:

$$\boldsymbol{v}(\boldsymbol{r}) = \frac{1}{4\pi} \int_R d^3r' \delta(\boldsymbol{r}') \frac{(\boldsymbol{r}-\boldsymbol{r}')}{|\boldsymbol{r}-\boldsymbol{r}'|^3} \tag{2.15}$$

where R denotes the survey volume.

$\delta(\boldsymbol{r})$ may be expanded in spherical harmonics:

$$\delta(\boldsymbol{r}) = \sqrt{\frac{2}{\pi}} \sum_{lm} \int_0^\infty dk k^2 \delta_{lm}(k) j_\ell(kr) Y_{\ell m}(\hat{\boldsymbol{r}}) \tag{2.16}$$

where the j_ℓ are spherical Bessel functions and the $Y_{\ell m}$ are spherical harmonics.

Substituting this into the expression for $\boldsymbol{v}(\boldsymbol{r})$ gives

$$\boldsymbol{v}(\boldsymbol{r}) = \frac{1}{4\pi}\int_R d^3r' \left(\sqrt{\frac{2}{\pi}}\sum_{lm}\int_0^\infty dk k^2 \delta_{lm}(k) j_\ell(kr) Y_{\ell m}(\hat{\boldsymbol{r}})\right)\frac{(\boldsymbol{r}-\boldsymbol{r}')}{|\boldsymbol{r}-\boldsymbol{r}'|^3}. \tag{2.17}$$

Then $\frac{(\boldsymbol{r}-\boldsymbol{r}')}{|\boldsymbol{r}-\boldsymbol{r}'|^3}$ must be expanded in spherical harmonics.

It is known that

$$\nabla_r\left[\frac{1}{|\boldsymbol{r}-\boldsymbol{r}'|}\right] = \frac{(\boldsymbol{r}-\boldsymbol{r}')}{|\boldsymbol{r}-\boldsymbol{r}'|^3} \tag{2.18}$$

and in spherical harmonics,

$$\frac{1}{|\boldsymbol{r}-\boldsymbol{r}'|} = 4\pi\sum_{\ell,m}\frac{1}{2\ell+1}\kappa_\ell(r,r')Y_{\ell m}(\hat{\boldsymbol{r}})Y^*_{\ell m}(\hat{\boldsymbol{r}}') \tag{2.19}$$

where

$$\kappa_\ell(r) \equiv \frac{r'^\ell}{r^{\ell+1}}, r > r' \tag{2.20}$$

$$\kappa_\ell(r) \equiv \frac{r^\ell}{r'^{\ell+1}}, r' > r \tag{2.21}$$

Substituting for this into Equation (2.17) gives

$$\boldsymbol{v}(\boldsymbol{r}) = \sqrt{\frac{2}{\pi}}\sum_{\ell\ell' mm'}\int d^3k\delta_{\ell m}(k)\nabla_r\int d^3r' j_\ell(kr')\frac{\kappa_{\ell'}(r)}{(2\ell'+1)}Y_{\ell m}(\hat{\boldsymbol{r}}')Y_{\ell' m'}(\hat{\boldsymbol{r}})Y^*_{\ell' m'}(\hat{\boldsymbol{r}}'). \tag{2.22}$$

Splitting up the r' integral,

$$\int d^3r' = \int dr' r'^2 \int d^2\hat{r}' \tag{2.23}$$

and substituting in gives

$$\boldsymbol{v}(\boldsymbol{r}) = \sqrt{\frac{2}{\pi}}\int d^3k\delta_{\ell m}(k)\nabla_r\sum_{\ell\ell' mm'}\frac{1}{(2\ell'+1)}\left[\int dr' r'^2 j_\ell(kr')\kappa_{\ell'}(r)\right]\times$$

$$Y_{\ell' m'}(\hat{\boldsymbol{r}})\left[\int d^2\hat{r}' Y_{\ell m}(\hat{\boldsymbol{r}}')Y^*_{\ell' m'}(\hat{\boldsymbol{r}}')\right]. \tag{2.24}$$

The orthogonality of the $Y_{\ell m}$s gives

$$\int_{4\pi} d^2\hat{r}' Y_{\ell m}(\hat{\boldsymbol{r}}') Y^*_{\ell' m'}(\hat{\boldsymbol{r}}') = \delta_{\ell\ell'}\delta_{mm'} \tag{2.25}$$

so

$$\boldsymbol{v}(\boldsymbol{r}) = \sqrt{\frac{2}{\pi}} \int d^3k \delta_{\ell m}(k) \nabla_r \sum_{\ell m} \frac{1}{(2\ell+1)} \left[\int_0^R dr' r'^2 j_\ell(kr') \kappa_\ell(r) \right] Y_{\ell m}(\hat{\boldsymbol{r}}). \tag{2.26}$$

Now an expression for ∇_r in spherical harmonics is needed.

$$\boldsymbol{\nabla}_r \equiv \hat{\boldsymbol{r}}(\hat{\boldsymbol{r}} \cdot \nabla) + \frac{i}{r}(\hat{\boldsymbol{r}} \times \boldsymbol{L}) \tag{2.27}$$

where

$$\boldsymbol{L} \equiv -i(\boldsymbol{r} \times \nabla) \tag{2.28}$$

is the classical angular momentum operator (Arfken 1985; §12.11).

So

$$\boldsymbol{\nabla}_r \kappa_\ell(r) Y_{\ell m}(\hat{\boldsymbol{r}}) = \kappa'_\ell(x) \boldsymbol{Y}^L_{\ell m}(\hat{\boldsymbol{r}}) - \kappa_\ell(r) \frac{i\sqrt{\ell(\ell+1)}}{r} \boldsymbol{Y}^M_{\ell m}(\hat{\boldsymbol{r}}) \tag{2.29}$$

where the vector spherical harmonics are defined as (Hill 1954)

$$\boldsymbol{Y}^L_{\ell m}(\hat{\boldsymbol{r}}) \equiv \hat{r} Y_{\ell m}(\hat{\boldsymbol{r}}) \tag{2.30}$$

and

$$\boldsymbol{Y}^M_{\ell m}(\hat{\boldsymbol{r}}) \equiv \frac{1}{\sqrt{\ell(\ell+1)}} (\hat{\boldsymbol{r}} \times \boldsymbol{L}) Y_{\ell m}(\hat{\boldsymbol{r}}) \tag{2.31}$$

Substituting in Equation (2.26) from Equation (2.29) gives the radial and transverse components of the error on the velocity field:

$$v_r(\boldsymbol{r}) = \sqrt{\frac{2}{\pi}} \sum_{\ell m} \int_0^\infty k^2 dk \delta_{\ell m}(k) \frac{1}{(2\ell+1)} \left[\int_R dr' r'^2 \kappa'_\ell(r, r') j_\ell(kr') \right] Y_{\ell m}(\hat{\boldsymbol{r}}) \tag{2.32}$$

and

$$\boldsymbol{v}_t(\boldsymbol{r}) = -\sqrt{\frac{2}{\pi}} \sum_{\ell m} \int_0^\infty k^2 dk \delta_{\ell m}(k) \frac{1}{(2\ell+1)} \left[\int_R dr' r'^2 \kappa_\ell(r) j_\ell(kr') \right] \frac{i\sqrt{\ell(\ell+1)}}{r} \boldsymbol{Y}^M_{\ell m}(\hat{\boldsymbol{r}}). \tag{2.33}$$

Evaluating the integrals in square brackets from R to ∞ gives the error on the velocity field due to structures external to the survey. This is done in Section (2.2.2) below.

Radial Component of the Variance

From Equation (2.32),

$$\left\langle v_r^2(r)\right\rangle = \frac{2}{\pi}\sum_{\ell m\ell' m'}\int dk k^4 \left\langle \delta_{\ell m}(k)\delta^*_{\ell' m'}(k)\right\rangle \frac{1}{(2\ell+1)}\frac{1}{(2\ell'+1)}\times$$

$$\left[\int_R dr' r'^2 \kappa'_\ell(r,r') j_\ell(kr')\right]\left[\int_R dr' r'^2 \kappa'_{\ell'}(r,r') j_{\ell'}(kr')\right] Y_{\ell m}(\hat{\boldsymbol{r}})Y^*_{\ell' m'}(\hat{\boldsymbol{r}}'). \tag{2.34}$$

The ensemble average of $\delta_{\ell m}(k)$ is (Heavens and Taylor 1997)

$$\left\langle \delta_{\ell m}(k)\delta^*_{\ell' m'}(k')\right\rangle = P(k)k^{-2}\delta_D(k-k')\delta^K_{\ell,\ell'}\delta^K_{mm'} \tag{2.35}$$

where $\delta_D(x)$ is the Dirac delta function and δ^K_{ij} is the Kronecker delta.

Substituting this into Equation (2.34) gives

$$\left\langle v_r^2(r)\right\rangle = \frac{2}{\pi}\sum_{\ell m}\int dk k^2 P(k)\frac{1}{(2\ell+1)^2}\left[\int_R dr' r'^2 \kappa'_\ell(r,r') j_\ell(kr')\right]^2 Y_{\ell m}(\hat{\boldsymbol{r}})Y^*_{\ell m}(\hat{\boldsymbol{r}}'). \tag{2.36}$$

Note that (Arfken 1985; §12.6)

$$\sum_m Y_{\ell m}(\hat{\boldsymbol{r}})Y^*_{\ell m}(\hat{\boldsymbol{r}}') = \frac{2\ell+1}{4\pi}\mathcal{P}_\ell(\mu) \tag{2.37}$$

where $\mathcal{P}_\ell(\mu)$ is the Legendre function and $\mu = \hat{\boldsymbol{r}}\cdot\hat{\boldsymbol{r}}'$.

Thus the radial component of the variance in the velocity field is

$$\left\langle v_r^2(r)\right\rangle = \int_0^\infty \frac{k^2 dk}{2\pi^2}P(k)\left|U_\ell(k,r)\right|^2 \tag{2.38}$$

where the effective window function is

$$\left|U_\ell(k,r)\right|^2 = \sum_l \frac{1}{(2\ell+1)}\left[\int_R dr' r'^2\left[\partial_r \kappa_\ell(r,r')\right] j_\ell(kr')\right]^2. \tag{2.39}$$

Transverse Component of the Variance

From Equation (2.33),

$$\left\langle v_t^2(r)\right\rangle = \frac{2}{\pi}\sum_{\ell m\ell' m'}\int dk k^4 \delta_{\ell m}(k)\delta_{\ell' m'}(k)\frac{\sqrt{\ell(\ell+1)}}{(2\ell+1)}\frac{\sqrt{\ell'(\ell'+1)}}{(2\ell'+1)}\frac{1}{r^2}\times$$

$$\left[\int_R dr' r'^2 \kappa_\ell(r,r') j_\ell(kr')\right]\left[\int_R dr' r'^2 \kappa_{\ell'}(r,r') j_{\ell'}(kr')\right] \boldsymbol{Y}^M_{\ell m}(\hat{\boldsymbol{r}})\cdot\boldsymbol{Y}^{*M}_{\ell' m'}(\hat{\boldsymbol{r}}). \tag{2.40}$$

Using Equation (2.35),

$$\left\langle v_t^2(r)\right\rangle = \frac{2}{\pi}\sum_{\ell m}\int dk k^4 k^{-2} P(k)\frac{\ell(\ell+1)}{(2\ell+1)^2}\frac{1}{r^2}\left[\int_R dr' r'^2 \kappa_\ell(r,r') j_\ell(kr')\right]^2 \times$$

$$\boldsymbol{Y}^M_{\ell m}(\hat{\boldsymbol{r}})\cdot\boldsymbol{Y}^{*M}_{\ell m}(\hat{\boldsymbol{r}}) \tag{2.41}$$

and noting that

$$\sum_m \boldsymbol{Y}^M_{\ell m}(\hat{\boldsymbol{r}})\cdot\boldsymbol{Y}^{*M}_{\ell m}(\hat{\boldsymbol{r}}') = \frac{2\ell+1}{4\pi}\mathcal{P}_\ell(\mu) \tag{2.42}$$

gives

$$\left\langle v_t^2(r)\right\rangle = \frac{2}{\pi}\frac{1}{r^2}\sum_\ell \int dk k^2 P(k)\frac{\ell(\ell+1)}{(2\ell+1)^2}\frac{2\ell+1}{4\pi}\left[\int_R dr' r'^2 \kappa_\ell(r,r') j_\ell(kr')\right]^2. \tag{2.43}$$

Therefore the transverse component of the variance is

$$\left\langle v_t^2(r)\right\rangle = \frac{1}{r^2}\int_0^\infty \frac{k^2 dk}{2\pi^2} P(k)\left|W_\ell(k,r)\right|^2 \tag{2.44}$$

where the window function is

$$\left|W_\ell(k,r)\right|^2 = \sum_\ell \frac{\ell(\ell+1)}{(2\ell+1)}\left[\int_R dr' r'^2 \kappa_\ell(r,r') j_\ell(kr')\right]^2. \tag{2.45}$$

2.2.1 Sampling variance from interior structure

In the case of interior structure, obviously $r < R$, where R is the radius of the survey. In this case the integral

$$I_\ell = \int_R dr' r'^2 \kappa_\ell(r, r') j_\ell(kr')$$

may be calculated. For interior structure, $\kappa_\ell(r, r') = r'^\ell / r^{\ell+1}$, and we have

$$I_\ell = \int_0^R dr' r'^2 \frac{r'^\ell}{r^{\ell+1}} j_\ell(kr'). \tag{2.46}$$

Multiplying this expression by $\frac{r^\ell}{r^\ell} \frac{r'^{\ell+1}}{r'^{\ell+1}}$ gives

$$I_\ell = \int_0^R dr' r'^2 \frac{r'^{2\ell+1}}{r^{2\ell+1}} \frac{r^\ell}{r'^{\ell+1}} j_\ell(kr') \tag{2.47}$$

$$= \frac{r^\ell}{r^{2\ell+1}} \int_0^R dr' r'^{(-\ell+1)} r'^{(2\ell+1)} j_\ell(kr').$$

Changing variables from r' to $t = kr'$ in Equation (2.62) gives

$$I_\ell = \frac{r^\ell}{r^{2\ell+1}} \int_0^{kR} \frac{dt}{k^{\ell+3}} t^{(-\ell+1)} t^{2\ell+1} j_\ell(t). \tag{2.48}$$

Two recurrence relations for the spherical Bessel functions are

$$\int_0^z dt t^{-\nu+1} j_\nu(t) = \left[\frac{\sqrt{\pi}}{2^\nu \Gamma(\nu + 1/2)} \right] - z^{-\nu+1} j_{\nu-1}(z) \tag{2.49}$$

and

$$\int_0^z dt t^{\nu+2} j_\nu(t) = z^{\nu+2} j_{\nu+1}(z). \tag{2.50}$$

Using these recurrence relations and integrating by parts then gives

$$I_\ell = \left(\frac{2\ell + 1}{k^2} \right) j_\ell(kr) - \frac{(kr)^\ell}{k^2} \frac{j_{\ell-1}(kR)}{(kR)^{\ell-1}}. \tag{2.51}$$

The radial derivative with respect to r is easily found, and is

$$I'_\ell = \left(\frac{2\ell+1}{k}\right) j'_\ell(kr) - \frac{\ell}{k}\left(\frac{r}{R}\right)^{\ell-1} j_{\ell-1}(kR). \tag{2.52}$$

Here the dash on the spherical Bessel function indicates differentiation with respect to the argument.

Substitute this into the expression for $v_r(\boldsymbol{r})$, Equation (2.32):

$$v_r(\boldsymbol{r}) = \sqrt{\frac{2}{\pi}} \sum_{\ell m} \int dk k^2 \delta_{\ell m}(k) \frac{1}{2\ell+1} \left[\left(\frac{2\ell+1}{k}\right) j'_\ell(kr) - \frac{\ell}{k}\left(\frac{r}{R}\right)^{\ell-1} j_{\ell-1}(kR) \right] Y_{\ell m}(\hat{\boldsymbol{r}}) \tag{2.53}$$

$$= \sqrt{\frac{2}{\pi}} \sum_{\ell m} \int dk k^2 \delta_{\ell m}(k) \left[\frac{1}{k} j'_\ell(kr) - \frac{\ell}{k(2\ell+1)}\left(\frac{r}{R}\right)^{\ell-1} j_{\ell-1}(kR) \right] Y_{\ell m}(\hat{\boldsymbol{r}}).$$

In the limit that $R \to \infty$, the expression for the true peculiar velocity field (Regös and Szalay 1989) is recovered.

$$v_r(\boldsymbol{r}) = \sqrt{\frac{2}{\pi}} \sum_{\ell m} \int dk k^2 \delta_{\ell m}(k) k^{-1} j'_\ell(kr) Y_{\ell m}(\hat{\boldsymbol{r}}). \tag{2.54}$$

Radial Cross-correlation

This is given by

$$\left\langle v_r(\boldsymbol{r}) v_r(\boldsymbol{r}') \right\rangle = \frac{2}{\pi} \sum_{\ell m \ell' m'} \int dk k^4 \delta_{\ell m}(k) \delta_{\ell' m'}(k) k^{-2} j'_\ell(kr) j'_{\ell'}(kr') Y_{\ell m}(\hat{\boldsymbol{r}}) Y^*_{\ell' m'}(\hat{\boldsymbol{r}'}). \tag{2.55}$$

Using Equation (2.35), this becomes

$$\left\langle v_r(\boldsymbol{r}) v_r(\boldsymbol{r}') \right\rangle = \frac{2}{\pi} \sum_{\ell m} \int dk k^4 k^{-2} k^{-2} P(k) j'_\ell(kr) j'_\ell(kr') Y_{\ell m}(\hat{\boldsymbol{r}}) Y^*_{\ell' m'}(\hat{\boldsymbol{r}'}) \tag{2.56}$$

and using Equation (2.37),

$$\left\langle v_r(\boldsymbol{r}) v_r(\boldsymbol{r}') \right\rangle = \frac{2}{\pi} \sum_{\ell} \int dk P(k) j'_\ell(kr) j'_\ell(kr') \frac{(2\ell+1)}{4\pi} \mathcal{P}_\ell(\mu), \tag{2.57}$$

the cross-correlation function of the radial velocities is then

$$\left\langle v_r(\boldsymbol{r}) v_r(\boldsymbol{r}') \right\rangle = \int_0^\infty \frac{dk}{2\pi^2} P(k) \sum_{\ell} (2\ell+1) j'_\ell(kr) j'_\ell(kr') \mathcal{P}_\ell(\mu). \tag{2.58}$$

Radial Variance

This is simply

$$\left\langle v_r^2(r)\right\rangle = \frac{2}{\pi}\sum_{\ell m \ell' m'}\int dk k^4 \delta_{\ell m}(k)\delta_{\ell' m'}(k)k^{-2}j_\ell'^2(kr)Y_{\ell m}(\hat{\boldsymbol{r}})Y^*_{\ell' m'}(\hat{\boldsymbol{r}}). \tag{2.59}$$

Which, using Equations (2.35) and (2.37), becomes

$$\left\langle v_r^2(r)\right\rangle = \int_0^\infty \frac{dk}{2\pi^2}P(k)\sum_\ell (2\ell+1)j_\ell'^2(kr). \tag{2.60}$$

2.2.2 Incompleteness due to external structures

The range of the radial integrals in the window functions determines the source of the uncertainties. One of the main uncertainties in reconstruction is the effect of the density field external to the survey volume. If the sampling variance is due to structures external to the survey volume then the range is $r > R$ where R is the radius of the survey. Thus $r \leq r'$ and so

$$\kappa_\ell(r, r') = r^\ell / r'^{\ell+1}. \tag{2.61}$$

The radial integral in Equation (2.45) may then be evaluated:

$$I_\ell = \int_R^\infty dr' r'^2 \kappa_\ell(r, r') j_\ell(kr')$$

$$= \int_R^\infty dr' r'^2 \frac{r^\ell}{r'^{\ell+1}} j_\ell(kr')$$

$$= \int_R^\infty dr' \frac{r^\ell}{r'^{(\ell-1)}} j_\ell(kr'). \tag{2.62}$$

Again change variables from $r'$to $t = kr'$, and note that

$$\int_R^\infty f(x)dx = \int_0^\infty f(x)dx - \int_0^R f(x)dx$$

$$I_\ell = \frac{r^\ell}{k^{-l+2}} \left[\int_0^\infty t^{-\ell+1} j_\ell(t) dt - \int_0^{kR} t^{-\ell+1} j_\ell(t) dt \right] \tag{2.63}$$

and using the recurrence relation, Equation (2.49),

$$I_\ell = k^{-2} (kr)^\ell \frac{j_{\ell-1}(kR)}{(kR)^{\ell-1}}. \tag{2.64}$$

Given this expression for the integral, the radial derivative of this with respect to r in Equation (2.39) is trivial:

$$I'_\ell = k^{-2} k^\ell \ell r^{\ell-1} \frac{j_{\ell-1}(kR)}{(kR)^{\ell-1}}. \tag{2.65}$$

Given these expressions, the velocity cross-correlations and variance may be found.

Radial Velocity Cross-correlation

The radial velocity is, from Equation (2.32) and using the expression for I'_ℓ,

$$v_r(\boldsymbol{r}) = \sqrt{\frac{2}{\pi}} \sum_{\ell m} \int dk k^2 \delta_{\ell m}(k) \frac{1}{2\ell+1} k^{-2} k^\ell \ell r^{\ell-1} \frac{j_{\ell-1}(kR)}{(kR)^{\ell-1}} Y_{\ell m}(\hat{\boldsymbol{r}}). \tag{2.66}$$

The radial cross-correlation function is then

$$\left\langle v_r(\boldsymbol{r}) v_r(\boldsymbol{r}') \right\rangle = \frac{2}{\pi} \sum_{\ell m \ell' m'} \int \frac{dk k^2}{(2\ell+1)(2\ell'+1)} \left\langle \delta_{\ell m}(k) \delta^*_{\ell' m'}(k) \right\rangle \ell \ell' \times$$

$$\frac{r^{\ell-1} r'^{\ell'-1}}{R^{(-\ell+1)} R^{(-\ell'+1)}} j_{\ell-1}(kR) j_{\ell'-1}(kR) Y_{\ell m}(\hat{\boldsymbol{r}}) Y^*_{\ell' m'}(\hat{\boldsymbol{r}}'). \tag{2.67}$$

Now using Equation (2.35),

$$\left\langle v_r(\boldsymbol{r}) v_r(\boldsymbol{r}') \right\rangle = \frac{2}{\pi} \sum_{\ell m} \int \frac{dk}{(2\ell+1)^2} P(k) \ell^2 \left[\frac{r r'}{R^2} \right]^{\ell-1} j^2_{\ell-1}(kR) Y_{\ell m}(\hat{\boldsymbol{r}}) Y^*_{\ell m}(\hat{\boldsymbol{r}\prime}). \tag{2.68}$$

Using Equation (2.37), this gives

$$\left\langle v_r(\boldsymbol{r}) v_r(\boldsymbol{r}') \right\rangle = \int_0^\infty \frac{dk}{2\pi^2} P(k) \sum_\ell \frac{\ell^2}{(2\ell+1)} \left[\frac{r r'}{R^2} \right]^{\ell-1} j^2_{\ell-1}(kR) \mathcal{P}_\ell(\mu). \tag{2.69}$$

Transverse Velocity Cross-correlation

Given Equation (2.33) and the expression for I_ℓ, the transverse velocity components are

$$\boldsymbol{v}_t(\boldsymbol{r}) = -\sqrt{\frac{2}{\pi}}\sum_{\ell m}\int dk k^2 \delta_{\ell m}(k)\frac{i\sqrt{\ell(\ell+1)}}{(2\ell+1)r}k^{-2}(kr)^\ell\left[\frac{j_{\ell-1}(kR)}{(kR)^{\ell-1}}\right]\boldsymbol{Y}^M_{\ell m}(\hat{\boldsymbol{r}}). \tag{2.70}$$

The cross-correlation is then

$$\left\langle \boldsymbol{v}_t(\boldsymbol{r})\cdot\boldsymbol{v}_t(\boldsymbol{r}')\right\rangle = \frac{2}{\pi}\sum_{\ell m\ell' m'}\int dk k^4 \delta_{\ell m}(k)\delta_{\ell' m'}(k)\frac{\sqrt{\ell(\ell+1)}}{(2\ell+1)r}\frac{\sqrt{\ell'(\ell'+1)}}{(2\ell'+1)r'}\times$$

$$k^{-4}(kr)^\ell(kr')^{\ell'}\frac{j_{\ell-1}(kR)}{(kR)^{\ell-1}}\frac{j_{\ell'-1}(kR)}{(kR)^{\ell'-1}}\boldsymbol{Y}^M_{\ell m}(\hat{\boldsymbol{r}})\cdot\boldsymbol{Y}^{*M}_{\ell' m'}(\hat{\boldsymbol{r}}'). \tag{2.71}$$

Once again using Equation (2.35),

$$\left\langle \boldsymbol{v}_t(\boldsymbol{r})\cdot\boldsymbol{v}_t(\boldsymbol{r}')\right\rangle = \frac{2}{\pi}\sum_{\ell m}\int dk k^4 k^{-2}P(k)\frac{\ell(\ell+1)}{(2\ell+1)^2}\frac{1}{rr'}k^{-4}k^{2\ell}\frac{r^\ell r'^\ell}{k^{2\ell-2}}\frac{j^2_{\ell-1}(kR)}{R^{2\ell-2}}\times$$

$$\boldsymbol{Y}^M_{\ell m}(\hat{\boldsymbol{r}})\cdot\boldsymbol{Y}^{*M}_{\ell' m'}(\hat{\boldsymbol{r}}') \tag{2.72}$$

and using Equation (2.42),

$$\left\langle \boldsymbol{v}_t(\boldsymbol{r})\cdot\boldsymbol{v}_t(\boldsymbol{r}')\right\rangle = \frac{2}{\pi}\sum_{\ell}\int dk k^4 P(k)\frac{\ell(\ell+1)}{(2\ell+1)^2}\frac{1}{rr'}k^{-4}k^{2\ell-2}\frac{r^\ell r'^\ell}{k^{2\ell-2}}\frac{j^2_{\ell-1}(kR)}{R^{2\ell-2}}\frac{(2\ell+1)}{4\pi}\mathcal{P}_\ell(\mu) \tag{2.73}$$

which gives the cross-correlation,

$$\left\langle \boldsymbol{v}_t(\boldsymbol{r})\cdot\boldsymbol{v}_t(\boldsymbol{r}')\right\rangle = \sum_{\ell}\int\frac{dk}{2\pi^2}P(k)\frac{\ell(\ell+1)}{2\ell+1}\left[\frac{(rr')}{R^2}\right]^{\ell-1}j^2_{\ell-1}(kR)\mathcal{P}_\ell(\mu). \tag{2.74}$$

In the case of an all sky survey, as orthogonal projections have been chosen there are no cross terms.

Radial Component of the Variance

Using the expression for I'_ℓ with Equations (2.39) and (2.38), the radial component of the variance on the velocity is found to be

$$\langle v_r^2(r)\rangle = \int_0^\infty \frac{k^2 dk}{2\pi^2} P(k) \sum_\ell \frac{1}{2\ell+1} \left[k^{-2} k^\ell \ell r^{\ell-1} \frac{j_{\ell-1}(kR)}{(kR)^{\ell-1}} \right]^2$$

$$= \int_0^\infty \frac{dk}{2\pi^2} P(k) \sum_\ell \frac{1}{2\ell+1} \left[k^2 k^{-4} k^{2\ell} \ell^2 r^{2\ell-2} \frac{j_{\ell-1}^2(kR)}{k^{2(\ell-1)} R^{2(\ell-1)}} \right]$$

$$\langle v_r^2(r)\rangle = \int_0^\infty \frac{dk}{2\pi^2} P(k) \sum_\ell \frac{1}{2\ell+1} \left[\ell^2 \left(\frac{r}{R}\right)^{2\ell-2} j_{\ell-1}^2(kR) \right]. \tag{2.75}$$

Transverse Component of the Variance

Substituting for I_ℓ in Equation (2.45), and using Equation (2.44), the transverse component of the velocity variance is

$$\langle v_t^2(r)\rangle = \int_0^\infty \frac{k^2 dk}{2\pi^2} P(k) \sum_\ell \frac{\ell(\ell+1)}{2\ell+1} \left[k^{-2} (kr)^\ell \frac{j_{\ell-1}(kR)}{(kR)^{\ell-1}} \right]^2$$

$$= \int_0^\infty \frac{dk}{2\pi^2} P(k) \sum_\ell \frac{\ell(\ell+1)}{2\ell+1} k^2 k^{-4} k^{2\ell} \frac{r^{2\ell}}{r^2} \frac{j_{\ell-1}^2(kR)}{k^{2\ell-2} R^{2\ell-2}}$$

$$\langle v_t^2(r)\rangle = \int_0^\infty \frac{dk}{2\pi^2} P(k) \sum_\ell \frac{\ell(\ell+1)}{2\ell+1} \left(\frac{r}{R}\right)^{2\ell-2} j_{\ell-1}^2(kR). \tag{2.76}$$

Total Variance

The total sample variance due to external structure is found using $\langle v_{cv}^2(r)\rangle = \langle v_r^2(r)\rangle + \langle v_t^2(r)\rangle$ and is

$$\langle v_{cv}^2(r)\rangle = \int_0^\infty \frac{dk}{2\pi^2} P(k) \sum_{\ell=1}^\infty \ell (r/R)^{2(\ell-1)} j_{\ell-1}^2(kR). \tag{2.77}$$

The summation is only non-zero from $\ell = 1$ since external structure cannot affect the monopole term.

The above expression is for the total cosmic variance in the CMB rest frame. To calculate the cosmic variance in the Local Group frame, first the total cosmic variance is written as

$$\left\langle (\boldsymbol{v}(\boldsymbol{r}) - \boldsymbol{v}(\boldsymbol{0}))^2 \right\rangle = \left\langle \boldsymbol{v}^2(\boldsymbol{r}) \right\rangle + \left\langle \boldsymbol{v}^2(\boldsymbol{0}) \right\rangle - 2 \left\langle \boldsymbol{v}(\boldsymbol{r}) \cdot \boldsymbol{v}(\boldsymbol{0}) \right\rangle . \tag{2.78}$$

The first term in this equation is given by Equation (2.77). The second term is found from Equation (2.77) by setting $r = 0$ and $l = 1$:

$$\left\langle \boldsymbol{v}^2(\boldsymbol{0}) \right\rangle = \int_0^\infty \frac{dk}{2\pi^2} P(k) j_0^2(kR). \tag{2.79}$$

The third term in Equation (2.78) is found using the radial and transverse cross-correlation cosmic variance terms found above. The radial cross-correlation is given by

$$\left\langle v_r(\boldsymbol{r}) v_r(\boldsymbol{r}') \right\rangle = \int_0^\infty \frac{dk}{2\pi^2} P(k) \sum_\ell \frac{\ell^2}{(2\ell+1)} \left[\frac{rr'}{R^2} \right]^{\ell-1} j_{\ell-1}^2(kR) \mathcal{P}_\ell(\mu).$$

Setting $\boldsymbol{r}' = 0$ and $l = 1$ gives

$$\left\langle v_r(\boldsymbol{r}) v_r(\boldsymbol{0}) \right\rangle = \frac{1}{3} \int_0^\infty \frac{dk}{2\pi^2} P(k) j_0^2(kR). \tag{2.80}$$

The transverse cross-correlation is given by

$$\left\langle \boldsymbol{v}_t(\boldsymbol{r}) \cdot \boldsymbol{v}_t(\boldsymbol{r}') \right\rangle = \sum_\ell \int \frac{dk}{2\pi^2} P(k) \frac{\ell(\ell+1)}{2\ell+1} \left[\frac{(rr')}{R^2} \right]^{\ell-1} j_{\ell-1}^2(kR) \mathcal{P}_\ell(\mu).$$

Again setting $\boldsymbol{r}' = 0$ and $l = 1$, we get

$$\left\langle \boldsymbol{v}_t(\boldsymbol{r}) \cdot \boldsymbol{v}_t(\boldsymbol{0}) \right\rangle = \frac{2}{3} \int \frac{dk}{2\pi^2} P(k) j_0^2(kR). \tag{2.81}$$

We then find the third term in Equation (2.78) by writing $\left\langle \boldsymbol{v}(\boldsymbol{r}) \cdot \boldsymbol{v}(\boldsymbol{0}) \right\rangle = \left\langle v_r(\boldsymbol{r}) v_r(\boldsymbol{0}) \right\rangle + \left\langle \boldsymbol{v}_t(\boldsymbol{r}) \cdot \boldsymbol{v}_t(\boldsymbol{0}) \right\rangle$:

$$\left\langle \boldsymbol{v}(\boldsymbol{r}) \cdot \boldsymbol{v}(\boldsymbol{0}) \right\rangle = \left[\frac{1}{3} \int_0^\infty \frac{dk}{2\pi^2} P(k) j_0^2(kR) \right] + \left[\frac{2}{3} \int \frac{dk}{2\pi^2} P(k) j_0^2(kR) \right]$$

$$= \int_0^\infty \frac{dk}{2\pi^2} P(k) j_0^2(kR). \tag{2.82}$$

Substituting for these terms into Equation (2.78) gives the total cosmic variance:

$$\left\langle (\boldsymbol{v}(\boldsymbol{r}) - \boldsymbol{v}(\boldsymbol{0}))^2 \right\rangle = \left[\int_0^\infty \frac{dk}{2\pi^2} P(k) \sum_{\ell=1}^{\infty} \ell (r/R)^{2(\ell-1)} j_{\ell-1}^2(kR) \right] +$$

$$\left[\int_0^\infty \frac{dk}{2\pi^2} P(k) j_0^2(kR) \right] - 2 \left[\int_0^\infty \frac{dk}{2\pi^2} P(k) j_0^2(kR) \right]. \tag{2.83}$$

The total cosmic variance in the Local Group frame is then

$$\left\langle v_{cv,LG}^2(r) \right\rangle = \int_0^\infty \frac{dk}{2\pi^2} P(k) \left[\sum_{\ell=1}^{\infty} \ell (r/R)^{2(\ell-1)} j_{\ell-1}^2(kR) - j_0^2(kR) \right]. \tag{2.84}$$

This is equivalent to the summation in Equation (2.77) going from $\ell = 2$ to $\ell = \infty$.

In this work the power spectrum of Peacock and Dodds (1994) is used:

$$\Delta^2(k) = \frac{k^3 P(k)}{2\pi^2} = \frac{(k/k_0)^\alpha}{1 + (k/k_1)^{\alpha-\beta}} \tag{2.85}$$

where $\alpha = 1.50$, $\beta = 4.0$, $k_0 = 0.29$, $k_1 = 0.039$.

Figure 2.1 shows the cosmic variance due to external structure in the CMB and Local Group frames for a survey with radius $R = 100h^{-1}Mpc$. In the CMB frame, the cosmic variance components rise from a minimum of just under $100kms^{-1}$ at the origin to a maximum of around $270kms^{-1}$ at the edge of the survey. In the Local Group frame the cosmic variance terms rise from zero at the origin to around $260kms^{-1}$ at the edge of the survey.

At the origin in the CMB frame the uncertainty is about $100kms^{-1}$ which is the dipole uncertainty for a survey of radius $R = 100h^{-1}Mpc$. The main effect with increasing distance is a rise in uncertainty from the centre of the survey to the edges, but even on the survey boundary the error is finite.

2.3 Shot Noise Errors

Shot noise is introduced into the reconstructed velocity field due to the discreteness of the survey data used.

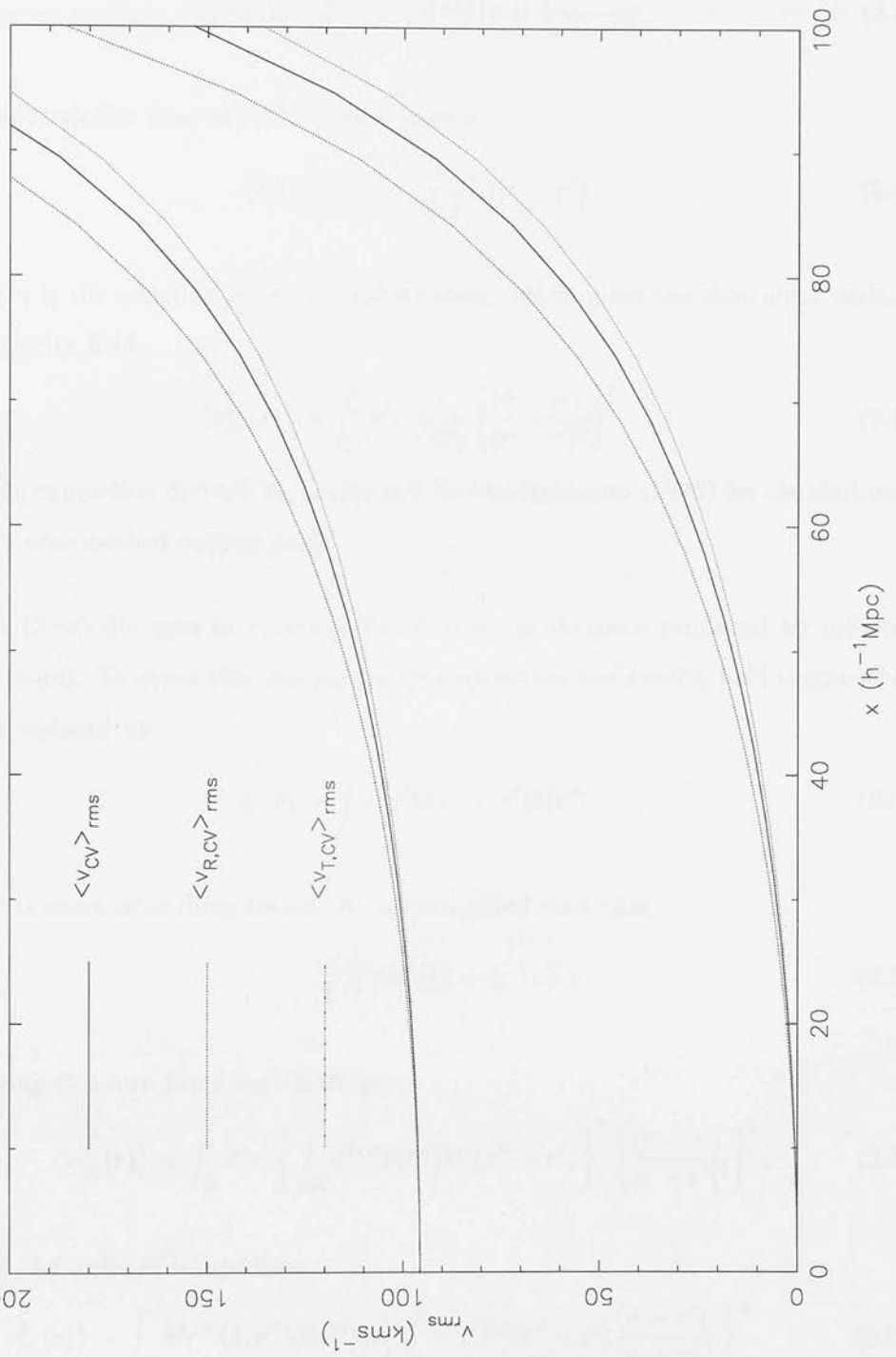

Figure 2.1: Cosmic variance on the reconstructed velocity field for a survey of radius $R = 100h^{-1}Mpc$ due to external structures. The upper curves are for the CMB frame, and the lower curves for the Local Group frame.

The variance on the velocity field is

$$\left\langle v_{sn}^2(r) \right\rangle = \int_R d^3r' \left\langle \delta(r)\delta(r') \right\rangle \frac{(r - r')}{|r - r'|^3}. \tag{2.86}$$

The autocorrelation function for Poisson noise is

$$\left\langle \delta(r)\delta(r') \right\rangle = \frac{1}{\phi(r)} \delta_D(r - r') \tag{2.87}$$

where $\phi(r)$ is the selection function. Substituting this in gives the shot noise variance on the velocity field:

$$\left\langle v_{sn}^2(r) \right\rangle = \int_R d^3r' \frac{1}{\phi(r)} \left[\frac{(r - r')}{|r - r'|^3} \right]^2. \tag{2.88}$$

This is the expression derived by Taylor and Rowan-Robinson (1993) for the shot noise due to an unsmoothed density field.

Equation (2.88) diverges as r approaches r' (infinite variance produced by infinitely close particles). To avoid this, during the reconstruction the density field is smoothed. Here δ is replaced by

$$\delta_s(r) = \int d^3r' W(r - r')\delta(r') \tag{2.89}$$

where W is some smoothing kernel. W is normalized such that

$$\int d^3r W(r) = 1. \tag{2.90}$$

Substituting this into Equation (2.86) gives

$$\left\langle v_{sn}^2(r) \right\rangle = \int_R d^3r' \left\{ \int_R d^3r'' \delta(r'') W(r'' - r') \right\}^2 \left[\frac{(r - r')}{|r - r'|^3} \right]^2. \tag{2.91}$$

Changing the order of integration,

$$\left\langle v_{sn}^2(r) \right\rangle = \int_R d^3r'' \left\langle \delta(r'')\delta(r''') \right\rangle \left\{ \int_R d^3r' W(r'' - r') \frac{(r - r')}{|r - r'|^3} \right\}^2. \tag{2.92}$$

Note that

$$\int_R d^3r' W(r'' - r') \frac{(r - r')}{|r - r'|^3} \tag{2.93}$$

is the velocity around a source with density distribution W.

Now,

$$\int_R d^3r' W(\boldsymbol{r}'' - \boldsymbol{r}') \frac{(\boldsymbol{r} - \boldsymbol{r}')}{|\boldsymbol{r} - \boldsymbol{r}'|^3} = G(\boldsymbol{r} - \boldsymbol{r}'') \tag{2.94}$$

where G is a Green function. So the equation for the shot noise variance becomes

$$\left\langle v_{sn}^2(r) \right\rangle = \int_R d^3r'' \left\langle \delta(\boldsymbol{r}'') \delta(\boldsymbol{r}''') \right\rangle \left| G(\boldsymbol{r} - \boldsymbol{r}'') \right|^2 . \tag{2.95}$$

Using Equation (2.87) this becomes

$$\left\langle v_{sn}^2(r) \right\rangle = \int_R \frac{d^3r''}{\phi(r'')} \left| G(\boldsymbol{r} - \boldsymbol{r}'') \right|^2 \tag{2.96}$$

or

$$\left\langle v_{sn}^2(r) \right\rangle = 2\pi \int_0^R \frac{dr'' r''^2}{\phi(r'')} \int_{-1}^{+1} d\mu \left| G(\boldsymbol{r} - \boldsymbol{r}'') \right|^2 . \tag{2.97}$$

If we pick a Gaussian smoothing kernel,

$$W(r) = \frac{\exp -\frac{1}{2}\frac{r^2}{R_s^2}}{(2\pi)^{3/2} R_s^3} \tag{2.98}$$

then the Green function is

$$\boldsymbol{G}(\boldsymbol{r}) = \hat{\boldsymbol{r}} \left[\frac{erf(\frac{r}{\sqrt{2}R_s})}{r^2} - \sqrt{\frac{2}{\pi}} \frac{e^{\frac{-r^2}{2R_s^2}}}{rR_s} \right] . \tag{2.99}$$

In this work $R_s = 5h^{-1}Mpc$.

The radial component of the shot noise may be calculated by projecting the shot noise along the line of sight:

$$\left\langle v_{sn,r}^2(r) \right\rangle = \int_0^R \frac{r'^2 dr'}{\phi(r')} \int_{-1}^{+1} d\mu \left| \hat{\boldsymbol{r}} \cdot \boldsymbol{G}(\boldsymbol{r} - \boldsymbol{r}') \right|^2 . \tag{2.100}$$

In this work, the PSCz selection function (equation 5.1) was used.

The tangential component may be found from the relation

$$\left\langle v_{sn,TOT}^2 \right\rangle = \left\langle v_{sn,r}^2 \right\rangle + \left\langle v_{sn,t}^2 \right\rangle . \tag{2.101}$$

The above expressions are for the shot noise in the CMB rest frame. The shot noise in the Local Group frame was found by evaluating Equations (2.97) and (2.100) at the origin and subtracting them in quadrature from the shot noise terms evaluated in the CMB frame.

Figure 2.2 shows the shot noise as a function of radius calculated in the Local group frame and the CMB frame, for a survey of radius $100h^{-1}Mpc$. The upper three lines correspond to the CMB frame and the lower lines to the Local Group frame. At radii smaller than about $40h^{-1}Mpc$, the shot noise in the CMB frame is larger than that in the Local Group frame, but at larger radii this effect becomes negligible. In the CMB frame, the components of the shot noise rise from around $55kms^{-1}$ at the origin to a maximum of around $160kms^{-1}$ at a radius of $R = 90h^{-1}Mpc$. The fall in shot noise at radii greater than this is an artifact due to the calculation being cut off at $100h^{-1}Mpc$. In the Local Group frame the shot noise components rise from zero at the origin to a maximum of again around $160kms^{-1}$ at a radius of $R = 90h^{-1}Mpc$. Therefore from the point of view of minimizing shot noise errors there is little to be gained in moving to the Local Group rest frame.

2.4 Incompleteness in the Cosmological Dipole

The cosmic variance on the velocity at radius r is given by Equation (2.77). As $r \to 0$, only the $\ell = 1$ term survives and we get

$$\langle v_{cv}(0) \rangle = \int_0^\infty \frac{dk}{2\pi^2} P(k) j_0(kR). \tag{2.102}$$

This gives the cosmic variance on the dipole. To calculate the cosmic variance again the power spectrum of Peacock and Dodds (1994) is used.

Figure 2.3 shows the cosmic variance from external structure and shot noise on the dipole, and the total rms uncertainty on the dipole added in quadrature, as a function of survey scale. The cosmic variance has been calculated for the case of structures external to the survey, as in Section (2.2.2), for a survey of radius $R = 300h^{-1}Mpc$.

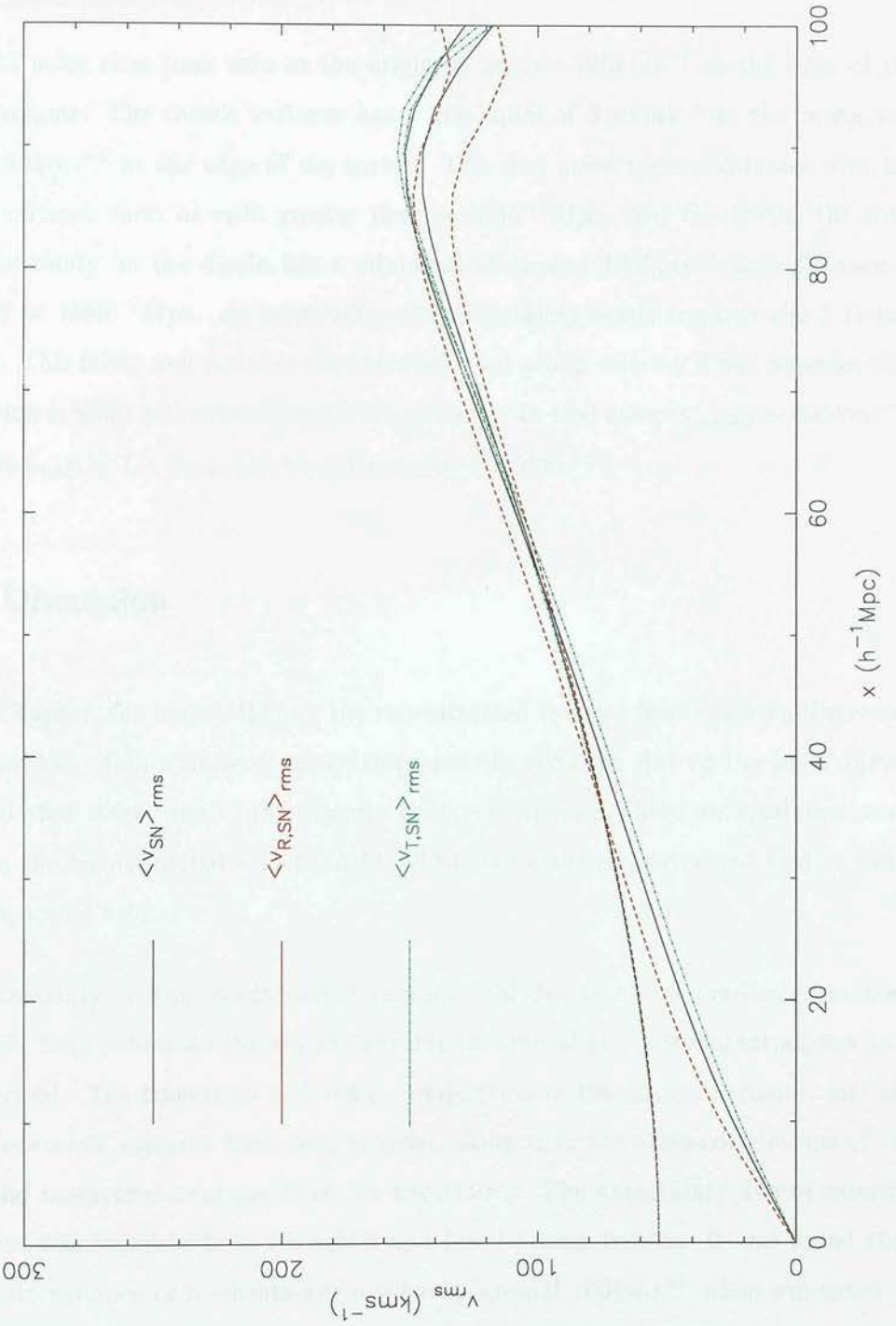

Figure 2.2: Shot noise on the reconstructed velocity field for a survey of radius $R = 100h^{-1}Mpc$. The upper curves are for the CMB frame, the lower curves for the Local Group frame.

The shot noise has been calculated using the PSCz selection function, again for a survey of radius $R = 300h^{-1}Mpc$.

The shot noise rises from zero at the origin to around $190kms^{-1}$ at the edge of the survey volume. The cosmic variance has a maximum of $340kms^{-1}$ at the origin and falls to $40kms^{-1}$ at the edge of the survey. The shot noise term dominates over the cosmic variance term at radii greater than $\sim 150h^{-1}Mpc$. For the PSCz, the total rms uncertainty on the dipole has a minimum of around $100kms^{-1}$ at a distance of about $R = 150h^{-1}Mpc$. At zero radius the uncertainty tends towards the 1 D rms velocity. This fairly well matches the observed local group velocity if one assumes that our motion is a fair estimate of the 3D rms velocity. In that case, $v_{rms,3D} \sim 606kms^{-1}$, and as $v_{rms,1D} = 1/\sqrt{3}v_{rms,3D}$, we get $v_{rms,1D} = 350kms^{-1}$.

2.5 Discussion

In this Chapter, the uncertainty on the reconstructed velocity field has been discussed. There are two main sources of uncertainty, cosmic variance, due to the finite survey size, and shot noise, due to the discrete galaxy sampling. These uncertainties cause errors in the reconstructed velocity field, which cause the reconstructed field to differ from the actual field.

The uncertainty on the reconstructed velocity field due to cosmic variance has been discussed. Expressions for the uncertainty due to internal and external structures have been derived. The transverse and radial components of the cosmic variance, and the total rms cosmic variance have been derived, along with the cross-correlations of the radial and transverse components of the uncertainty. The uncertainty due to external structures was found in both the CMB and Local Group frames. It was found that the cosmic variance components are smaller by around $100kms^{-1}$ when evaluated in the Local Group frame than in the CMB frame. Thus the velocity field relative to the motion of an observer can be calculated far more accurately than absolute velocities. Hence one should work in the Local Group rest frame when comparing velocities.

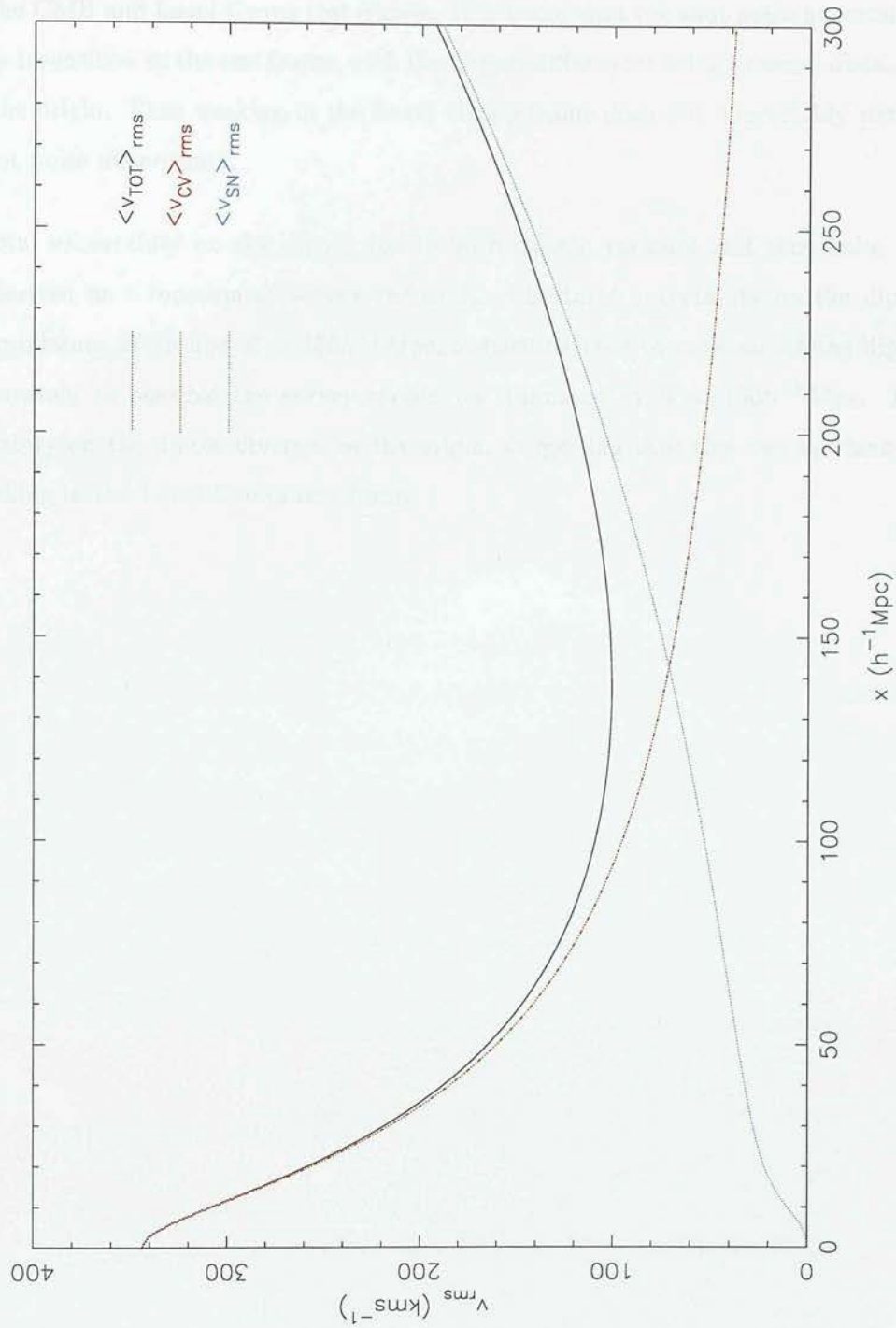

Figure 2.3: Incompleteness on the dipole, for a survey of radius $R = 300h^{-1}Mpc$. The cosmic variance, shot noise and total rms uncertainties are shown.

The shot noise uncertainty on the reconstructed velocity field has been discussed. The radial and transverse components of the shot noise uncertainty have been derived, in both the CMB and Local Group rest frames. It is found that the shot noise uncertainty is fairly insensitive to the rest frame, with the largest differences being at small distances from the origin. Thus working in the Local Group frame does not appreciably reduce the shot noise uncertainty.

The total uncertainty on the dipole due to both cosmic variance and shot noise has been derived as a function of survey radius R. The total uncertainty on the dipole has a minimum at around $R = 150h^{-1}Mpc$, suggesting that to reconstruct the dipole as accurately as possible the survey should be truncated at $R = 150h^{-1}Mpc$. The uncertainty on the dipole diverges at the origin, suggesting that this can be removed by working in the Local Group rest frame.

Chapter 3

PIZA with Realistic Galaxy Redshift Surveys

In this chapter I will discuss the Path Interchange Zel'dovich Approximation. In Section 3.1 I will introduce the basic PIZA method, as outlined in Croft and Gaztañaga (1997), hereafter CG97, and its application to real space galaxy surveys. In Section 3.2 I introduce the idea of generalizing PIZA for use with realistic galaxy surveys and discuss the problems which must be addressed. In Section 3.6 I describe the tests which I have applied to PIZA in order to gauge the accuracy of its reconstructions, and present the results from these tests. This work has been submitted to MNRAS (Valentine, Saunders and Taylor 2000).

3.1 Introduction to PIZA

3.1.1 The Least Action Principle and the Zel'dovich Approximation

In this Section it is shown how the least action principle when combined with the Zel'dovich Approximation requires the minimization of the mean square particle displacement. This is taken from CG97.

Consider a set of nonrelativistic particles of mass m_i and comoving coordinate x_i. The action for this set of particles is given by the integral of the particles' Lagrangian over time

$$L = \int_0^t \mathcal{L}\, dt \tag{3.1}$$

The Lagrangian is given by

$$\mathcal{L} = K - W \tag{3.2}$$

where K is the kinetic energy and W the potential energy of the set of particles.

An expression for the action for the particles in terms of their masses and positions is needed. The kinetic energy of the set of particles is given by

$$K = \frac{1}{2}\sum_i m_i a^2 \dot{x}_i^2 \tag{3.3}$$

where a is the universal expansion factor.

Using the Zel'dovich Approximation, the position of a particle may be written as

$$x_i(t) = x_i(0) + D(t)\Psi_i \tag{3.4}$$

where D is the linear growth factor and Ψ is some small displacement. Assuming the initial velocities are negligible, the comoving velocity of each particle is

$$\dot{x}_i = \dot{D}(t)\Psi_i = \frac{\dot{D}(t)}{D(t)}\Delta x_i \tag{3.5}$$

where

$$\Delta x_i = x_i(t) - x_i(0) = D(t)\Psi_i \tag{3.6}$$

Substituting this expression for $\dot{x}$ into Equation (3.3) gives

$$K = \frac{1}{2}a^2\dot{D}^2\sum m_i\Psi_i^2 \tag{3.7}$$

The mean square particle displacement is now defined to be

$$\Psi_0^2 = \sum m_i\Psi_i^2 \tag{3.8}$$

Having found an expression for the kinetic energy, an expression for the potential energy is needed.

The energy conservation equation for the Lagrangian is

$$\frac{d}{dt}a(K+W) = -K\dot{a} \tag{3.9}$$

The potential energy of the set of particles is then

$$W = -K - \frac{1}{a}\int_0^a K da \tag{3.10}$$

Substituting for K gives

$$W = -\frac{1}{2}\Psi_0^2\left[a^2\dot{D}^2 + \frac{1}{a}\int_0^a a^2\dot{D}^2 da\right] \tag{3.11}$$

Now using Equations (3.1) and (3.2) and noting that $dt = da/\dot{a}$. The expression for the action is then

$$L = \Psi_0^2\int_0^1 \frac{da}{\dot{a}}\left[a^2\dot{D}^2 + \frac{1}{2a}\int_0^a a^2\dot{D}^2 da\right] \tag{3.12}$$

In this situation the kinetic and potential energy, the Lagrangian and the action are proportional to the mean square particle displacement Ψ_0^2. The least action principle therefore requires the minimization of the mean square particle displacement. From Equation (3.6), $\Psi_i \propto \Delta x_i$. Combining this with Equation (3.8) gives

$$\Psi_0^2 \propto \sum m_i \Delta x_i^2 = S \tag{3.13}$$

Therefore minimizing the mean square particle displacement is equivalent to minimizing the mass times the particle displacement squared.

It is this minimization of the mean square particle displacement that is the basis of the PIZA reconstruction method. The set of Δx_i that minimize Ψ_0 for a given final particle distribution may be estimated with the assumption that the initial distribution is homogeneous.

3.1.2 Applying PIZA to a Galaxy Distribution

In this section I will describe how PIZA may be applied to a galaxy distribution.

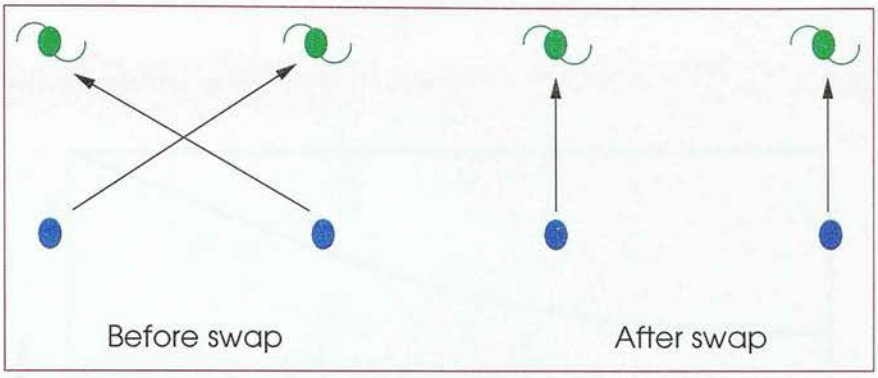

Figure 3.1: A typical PIZA interchange.

In the previous section it was shown that to reconstruct galaxy displacements from their present day positions, the mean square particle displacement, Equation (3.13), is minimized. CG97 simplify things further by assuming all the galaxies have equal mass, so the quantity to minimize becomes

$$S = \sum \Delta x_i^2 \tag{3.14}$$

The final positions used in PIZA are simply the present day galaxy positions. The initial positions are drawn from a homogeneous distribution of points, and are assigned at random to the galaxies. Hereafter these initial positions will be referred to as PIZA particles.

Once the initial and final distributions have been defined, applying PIZA is very simple. Two galaxies are picked at random, and their PIZA particles are interchanged. S is calculated before and after the swap. If the swap results in S decreasing, the swap is kept, and if not, the particles are swapped back again. See Figure 3.1 for a typical PIZA swap.

The expected value for S is approximately equal to the number of particles times the expected magnitude of a displacement squared, i.e.

$$\langle S \rangle = N_p \langle \Delta x^2 \rangle \tag{3.15}$$

where N_p is the total number of particles. If we assume that a typical trajectory is of

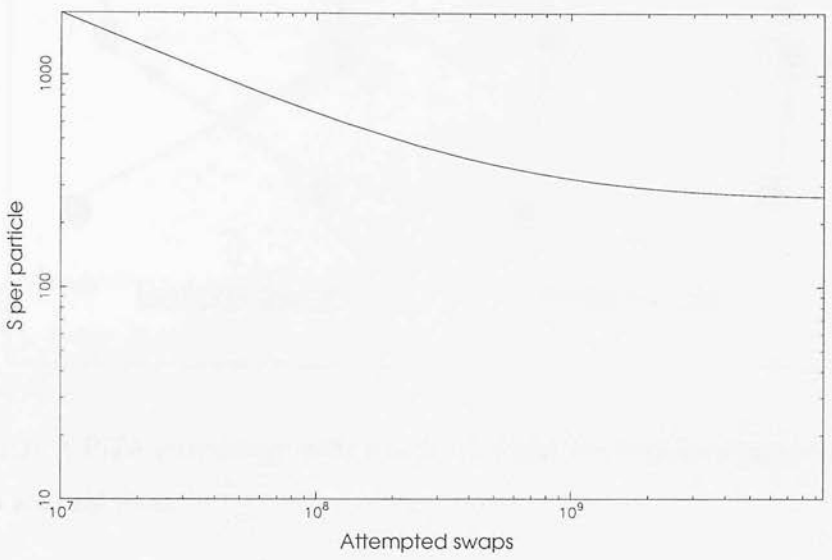

Figure 3.2: A typical PIZA cooling curve.

order $6h^{-1}Mpc$, we have

$$\langle S \rangle \sim 36 N_p h^{-2} Mpc^2 \tag{3.16}$$

Swaps are attempted until the rate of change of S with attempted swaps has become very low. This is referred to as the cooling rate. A typical cooling curve is shown in Figure 3.2. It is not necessary to continue until S has actually reached its minimum. In CG97, it was found that the number of swaps needed for the system to have cooled sufficiently is approximately 500 times the number of particles.

***'It is of course possible to use more than one PIZA particle per galaxy. CG97 found that this increased the accuracy of the reconstruction. PIZA using ν particles per galaxy is applied in a similar way to that described above for $\nu = 1$. Each galaxy is assigned ν particles at random, and then reassignments are attempted. Again galaxy pairs are picked at random. One of the particles from each of these galaxies is then picked at random to be reassigned, the swap is attempted, and as before it is accepted if it decreases S. The remaining $\nu - 1$ particles assigned to each galaxy do not have

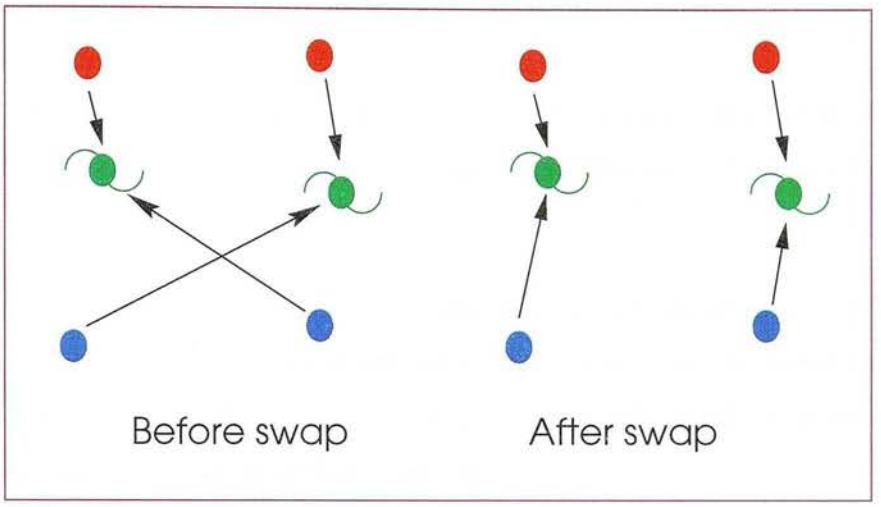

Figure 3.3: A PIZA interchange with $\nu = 2$. The blue particles are swapped, and the red particles are held fixed.

their galaxy assignment changed during the swap, see Figure 3.3. Once PIZA has been run, each galaxy's trajectory is found by averaging the trajectories of its particles.

Narayanan and Croft (1999) have tested a variety of methods for the reconstruction of the initial density fluctuation field. The reconstruction methods they have tested are: linear theory; the Gaussianization method of Weinberg (1992); the quasi-linear dynamical schemes of Nusser and Dekel (1992) and Gramman (1993a); The hybrid dynamical Gaussianization method of Narayanan and Weinberg (1998); PIZA. They found that PIZA has the best recovery of all the reconstruction schemes tested, that it is able to reproduce the true initial density on a point by point basis very well even at small smoothing scales. However, they found that there are not enough peaks in the reconstructed density field.

3.1.3 Redshift Space PIZA in CG97

CG97 tackle the problem of applying PIZA to a redshift survey in Section 3.6 of their paper. Here I will describe their method, which is similar to that which I have developed.

3.1.3 Redshift Space PIZA in CG97

CG97 tackle the problem of applying PIZA to a redshift survey in Section 3.6 of their paper. Here I will describe their method, which is similar to that which I have developed.

The problem is that PIZA minimizes particle displacements squared in real space but from a redshift survey only the redshift space displacements may be found. Some way of deprojecting the redshift positions into real space is needed. This is simple using the Zel'dovich approximation, as will be shown below.

In CG97, the method of finding the real space displacements from the redshifts is as follows: If the observer is at the origin then the redshift space position of a particle may be written as

$$s_i = x_i + \hat{s}_i \left(\frac{\dot{x}_i}{H} \cdot \hat{s}_i \right) \tag{3.17}$$

where $\hat{s}_i = s_i/|s_i|$ is the unit vector along the line of sight and x_i is the real space position. Using Equation (3.5), $H = \dot{a}/a$ and $f = \frac{d \ln D}{d \ln a} \simeq \Omega^{0.6}$, the peculiar velocity of a particle is

$$\dot{x}_i = H f \Delta x_i \tag{3.18}$$

Combining this with Equation (3.17) gives, in terms of the initial position and the displacement,

$$s_i = x_i(0) + \Delta x_i + \hat{s}_i (f \Delta x_i \cdot \hat{s}_i) \tag{3.19}$$

This set of linear equations may then be solved to obtain the three components of the real space displacement in terms of the initial and redshift space positions. These real space displacements are then used in PIZA along with an assumed value for f, with swaps being attempted as usual.

CG97 found that when using redshifts in PIZA, the scatter in the reconstruction is increased. They also found that the reconstructed real space density field can be recovered fairly well when smoothed on large scales.

CG97 did not try applying their method on either a real redshift survey or a simulation with spherical redshift distortions. In fact they took real space simulations and created redshift space simulations using the distant observer approximation.

Having reviewed PIZA, I will now move on to describe how I have adapted PIZA to use with realistic redshift surveys with a selection function.

3.2 Generalized PIZA

There are a few reasons as to why I have attempted to generalize PIZA for use with galaxy redshift surveys.

As mentioned in Chapter 1, other least action based methods are computationally intensive. As a result they have not been applied to cosmologically interesting volumes. PIZA is less computationally intensive than these methods, and is simple to use even when applied to large numbers of galaxies. Therefore a PIZA which may be used in reconstructions of large volumes would be very useful.

As mentioned above, CG97 only applied PIZA to n-body simulations, so another reason to generalize PIZA was to apply it to real galaxy surveys, specifically for this project the PSCz survey . At the outset of this project, PIZA had never been applied to real galaxies.

In CG97 it was stated that "In principle it should be simple to make a Lagrangian procedure work in redshift space", and "The method ... also works directly in redshift-space with minimal modification." I have found that generally this is the case, although there are problems in the application of PIZA to redshift surveys which will be discussed later in this Chapter. The main problem in generalizing PIZA came with the selection function. In CG97, they said "The method will need some modification to deal with observed samples of galaxies with a selection function". Indeed, "some" is a bit of an understatement. The problem of the selection function will be discussed in the next Chapter.

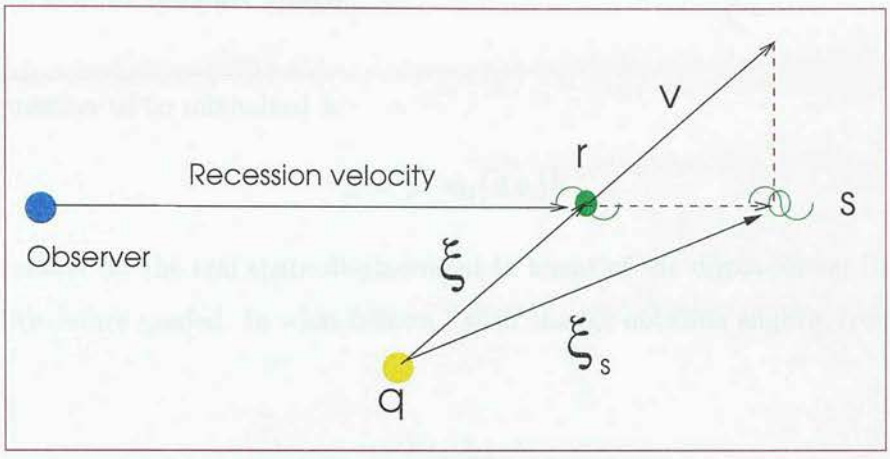

Figure 3.4: Real and redshift space positions

3.2.1 Redshift space PIZA

The problems associated with applying PIZA to a redshift survey are as follows:

1. PIZA minimizes the displacements of galaxies in real space. Using a redshift survey gives the displacements in redshift space, so some relation between the two is needed.

2. If a flux limited survey is used, the number density of objects in the survey decreases with increasing redshift. This is quantified by the selection function. A uniform distribution of PIZA particles would be unsuitable in this case.

3. The survey redshifts are in the Local Group rest frame. To convert between these redshifts and the real space galaxy positions, the velocity of the Local Group is needed.

4. In a galaxy survey there are likely to be regions, such as the Galactic Plane, that are not covered.

The first of these difficulties was tackled by CG97 §3.6 (see Section 3.1.3). The approach I have taken is slightly different.

3.2.2 PIZA in redshift space

The expression to be minimized is

$$S = \sum m_i (\Delta x_i)^2 \tag{3.20}$$

An expression for the real space displacement in terms of the displacement in redshift space is therefore needed. In what follows I shall change notation slightly from that of CG97.

$$\xi = \Delta x \tag{3.21}$$

The real space position of the galaxy may be written in terms of its initial position and its displacement in real space ξ

$$\boldsymbol{r} = \boldsymbol{q} + \boldsymbol{\xi} \tag{3.22}$$

The position of a galaxy in redshift space may be written as

$$\boldsymbol{s} = \boldsymbol{r} + \hat{\boldsymbol{r}}(\hat{\boldsymbol{r}} \cdot \boldsymbol{v}) \tag{3.23}$$

or

$$s = \boldsymbol{q} + \boldsymbol{\xi} + \hat{\boldsymbol{r}}(\hat{\boldsymbol{r}} \cdot \boldsymbol{v}) \tag{3.24}$$

where $\boldsymbol{v} = \frac{d\boldsymbol{\xi}}{dt}$ is the galaxy's peculiar velocity, $\hat{\boldsymbol{r}}$ the unit vector along the line of sight to the galaxy, and distances are measured in units of $h^{-1}Mpc$ where $h = H_0/100$. See Figure 3.4.

Using linear theory, the peculiar velocity in terms of the displacement is

$$\boldsymbol{v} = \beta \boldsymbol{\xi} \tag{3.25}$$

where $\beta \approx \frac{\Omega_0^{0.6}}{b}$ is the linear distortion parameter and b the linear bias parameter.

Therefore

$$\boldsymbol{s} = \boldsymbol{r} + \beta \hat{\boldsymbol{r}}(\hat{\boldsymbol{r}} \cdot \boldsymbol{\xi}) \tag{3.26}$$

or

$$s = q + \xi^s \tag{3.27}$$

where ξ^s is the redshift space displacement. (Superscripts 's' denote a variable measured in redshift space.)

Following Taylor and Hamilton (1996), the redshift space displacement field is related to the real space displacement field by

$$\xi_i^s = \mathcal{P}_{ij}\xi_j \tag{3.28}$$

where

$$\mathcal{P}_{ij} \equiv \delta_{ij}^K + \beta\hat{r}_i\hat{r}_j \tag{3.29}$$

is the redshift space projection tensor, and δ_{ij}^K is the Kronecker tensor.

Inverting Equation 3.28 gives the inverse relation (Taylor and Valentine 1999):

$$\xi_i = \mathcal{P}_{ij}^{-1}\xi_j^s \tag{3.30}$$

where

$$\mathcal{P}_{ij}^{-1} \equiv \delta_{ij}^K - \frac{\beta}{1+\beta}\hat{r}_i\hat{r}_j \tag{3.31}$$

is the inverse redshift space projection tensor.

Squaring Equation (3.30),

$$\xi^2 = \xi^{s^2} - (1 - \frac{1}{(1+\beta)^2})\xi_r^{s^2} \tag{3.32}$$

Here ξ_r^s is the displacement vector in redshift space projected along the line of sight. This is an expression for the real space displacement squared in terms of the redshift space displacement squared. To use this expression in PIZA, an a priori value for β must be assumed.

3.2.3 Frames of Reference

The redshifts in a galaxy survey are obviously measured in the rest frame of the Earth. These may be converted to heliocentric redshifts, and then transformed to the Local Group rest frame using the transformation of Yahil *et al.* (1977), by adding $300 \sin b \cos l$ where l and b are the galactic longitude and latitude respectively.

The transformation from real to redshift space in the Local Group frame is found by subtracting the Local Group displacement from the redshift displacement vector found above (Equation (3.28)):

$$\xi_i^{s,LG} = \mathcal{P}_{ij}\xi_j - \beta\hat{r}_i\hat{r}_j\xi^{LG} \tag{3.33}$$

or

$$\xi_i^{s,LG} = \mathcal{P}_{ij}\xi_j - (\mathcal{P}_{ij} - \delta_{ij}^K)\xi^{LG} \tag{3.34}$$

Here the superscript LG denotes a variable measured in the Local Group frame.

Inverting this equation gives the real space displacement in terms of the Local Group frame redshift displacement:

$$\xi_i = \mathcal{P}_{ij}^{-1}\xi_j^{s,LG} + (\delta_{ij}^K - \mathcal{P}_{ij}^{-1})\xi^{LG} \tag{3.35}$$

The displacement squared is then:

$$\xi^2 = \xi^{s^2} - \xi_r^{s^2} + \frac{(\beta\xi_r^{LG} + \xi_r^s)^2}{(1+\beta)^2} \tag{3.36}$$

In the remainder of this work, this expression will be used for the displacement squared.

Therefore to find the real space displacements, the displacement of the Local Group is needed. To find this displacement, a galaxy representing the Local Group is placed at the origin. Hereafter, this galaxy will be referred to as the "Local Group galaxy". It should be noted that the Local Group galaxy's position is the same in all frames, and in real and redshift space. Once the minimization has been carried out, the trajectory of this galaxy may be used to estimate the dipole.

3.2.4 Sky Coverage

The incomplete sky coverage of a galaxy survey may cause problems with PIZA, as with other reconstruction methods, since in these regions we do not know the true galaxy distribution. If PIZA particles were picked in the empty regions of the survey, the lack of galaxies in those regions would lead to spurious outflows as the particles had to move out to look for galaxies. Therefore the sky coverage of the PIZA particles was chosen to be the same as that of the galaxies.

A number of choices for filling in the empty regions present themselves. One could populate the incomplete regions randomly on the sky, assuming no information, or leave the regions empty of both particles and galaxies. These are equivalent except for particles adjacent to the mask. Alternatively, one could interpolate across the regions using correlations in the density field to fill in the gaps. In reconstructing PSCz the Fourier Interpolation Scheme of Saunders and Ballinger (2000) is used, which allows optimal, nonlinear interpolation across these regions (see Chapter 5).

PIZA will pick trajectories that cross the empty regions. In the case of PSCz it will pick trajectories which cross the galactic plane since there are more galaxies in the survey above the plane than below it. Obviously these trajectories are incorrect, and they are not included in the analysis.

3.2.5 PIZA with a Selection Function

All flux limited redshift surveys have the property that the number density of survey objects decreases with increasing distance. This must be taken account of when applying PIZA, because a lack of galaxies in the survey at large distances does not necessarily mean a lack of galaxies in the Universe at those distances.

In order to account for this change in the number density with distance, initial PIZA particles are picked with the same selection function as the galaxies, with normalization depending on the particle to galaxy ratio.

Galaxies that fall below the flux limit at a given distance must also be taken into account. Galaxies at greater distances have to represent a larger fraction of the underlying distribution of galaxies. To take account of those galaxies and particles that fall below the flux limit, each galaxy is assigned a weight of $1/\phi(r)$ and each PIZA particle a weight of

$$m_i = 1/(\nu\phi(r_i)), \tag{3.37}$$

where ν is the number of particles assigned per galaxy. In this work $\nu = 10$ was used in order to reduce the shot noise in the reconstruction. These weights are used in the generalized PIZA as the masses of the galaxies and particles. Obviously they are not the actual masses, but effective masses used to take account of the selection function. It should be noted that in the remainder of this Chapter, 'mass' is taken to mean 'effective mass'. Equations (3.36) and (3.37) are used in Equation (3.20) to minimize the displacement squared.

The problems associated with the selection function are discussed in more detail in the next Chapter.

3.3 Problems with Generalizing PIZA

Having come up with possible solutions to the problems of generalizing PIZA, the next step is obviously to take these solutions and apply them. In Section 3.5 I will describe my final version of PIZA in redshift space. In this Section I will discuss two significant problems I had when trying to generalize PIZA.

3.3.1 Trajectories which increase in length

In this new generalized PIZA the mass-weighted mean square particle displacement is minimized. It is possible for PIZA to pick swaps that decrease S but actually increase the length of one of the particles' trajectories. This happens to the very light particles at the centre of the survey, and results in these particles having very long trajectories

to galaxies at the edge of the survey volume. Unlike normal long trajectories, these will tend to become even longer with more attempted swaps.

Initially I decided to simply try minimizing

$$S = \sum_i \xi_i^2. \tag{3.38}$$

This is the minimization that CG97 carry out for particles of equal mass. However, this does not work and can cause PIZA to get stuck in a false minimum. The reason why this does not work may be to do with the selection function and the fact that there are fewer particles and galaxies at greater distances.

An alternative solution to this problem is to add a constant to all the particle masses. This should remove the problem of the very small particle masses and hence the problem of displacements increasing. However I rejected this method, as the value for the constant would be another variable to add to PIZA.

My solution to this problem was to minimize Equation (3.20) as normal and also to minimize the displacements squared in redshift space. The reason why I chose to also minimize the displacements squared in redshift space rather than in real space is that doing the latter can cause PIZA to get stuck in a false minimum. This method is similar to the above method of minimizing Equation (3.38). A possible reason for my alternative solution not working may be that more swaps are accepted in this case than when also minimizing the displacements in redshift space, and it is these swaps that cause PIZA to reach a false minimum.

3.3.2 Increasing S

Having solved the above problems with generalizing PIZA, it was slightly disturbing to find that the mean square particle displacement, S, would occasionally increase.

This may occur because of the way in which my PIZA algorithm works. Rather than calculating S for the entire ensemble of galaxy - particle pairs, S for the two galaxy -

particle pairs being interchanged is calculated and minimized, i.e.

$$S_2 = \sum_{i=1}^{2} m_i \Delta x_i^2 \tag{3.39}$$

This is done for reasons of speed. It is possible that S_2 is decreased by an interchange but the total S is not. This can occur due to the Local Group displacement term in Equation (3.36). Obviously when the Local Group galaxy is interchanged, its trajectory will change, and this will change the total value of S, so while S_2 decreases it is possible for the total S to increase.

At first glance this appears to be undesirable, as the whole point of PIZA is to minimize S. The solution would appear to be simply to make sure that when the Local Group galaxy is swapped, the total S as well as S_2 is minimized. However, in practice this does not work so well, as once again this can cause PIZA to become stuck in a false minimum.

My solution to this problem was to leave it and let the S increase when the Local Group galaxy is interchanged. In practice the increase is only small, and it does not affect the minimization of S overall.

3.4 Other methods which were investigated

3.4.1 Holding ξ_{LG} fixed

This method was developed in order to leave ξ_{LG} constant throughout a number of PIZA swaps, and hence avoid the problem of S increasing as described in the previous Section. In this method, ξ_{LG} was not estimated from the trajectory of the Local Group galaxy, but was kept fixed. Of course the Local Group galaxy is still included in PIZA. In this method PIZA was run in stages with each beginning where the last finished. The first stage has $\xi_{LG} = 0$. At the beginning of each successive stage, ξ_{LG} is increased until the true value of ξ_{LG} is reached. This method obviously avoids the problem of ξ_{LG} changing and increasing the value of S, but it has the disadvantage that the value of ξ_{LG} must be known beforehand. Since ξ_{LG} is used to estimate the dipole and β from

the reconstruction, I chose not to use this method.

An alternative method that I tried was similar to the above method, except that in this case the value of ξ_{LG} used in Equation 3.36 was taken from the Local Group trajectory at the end of the previous PIZA stage. This has the advantage over the previous method that the true value of ξ_{LG} is not needed. However, I decided that it is better to allow ξ_{LG} to vary freely within PIZA than to hold it fixed for some arbitrary amount of swaps.

3.4.2 Increasing β

Another method that I tried was to run PIZA in stages as above, but this time increasing β slowly from $\beta = 0$ with each stage until it reaches the true value. This has the advantage of introducing the redshift space distortions slowly, but it was found that this did not improve PIZA significantly, if at all. This method also has the disadvantage that it is relatively slow. For these reasons I have not used this method.

3.4.3 Ordering trajectories

Although PIZA is a much faster reconstruction method than other least action methods, it is still computationally expensive, and any ways to speed PIZA up are advantageous. One method which I used to speed PIZA up was to order the trajectories according to their lengths, starting with the longest. The particles and galaxies to swap were then chosen starting with those with the longest trajectories. It was thought that this would work because the longest trajectories would be swapped first and so S would be minimized quickly. However, this method had the drawback that the ordering of the trajectories took a very long time to do. There are two reasons for this. Firstly, there are on average 15,000 galaxies and 10 times as many particles in PIZA, and the trajectories of all these galaxy - particle pairs had to be ordered. Secondly, this list of trajectories had to be reordered when swapping made some of the trajectories smaller. In practice it was found that this method was too time consuming and it was rejected in favour of picking galaxy-particle pairs at random.

3.5 Final version of PIZA

Having described the obstacles needed to be overcome in order to generalize PIZA, and some of the problems that I encountered whilst attempting to do this, I will now describe the final working version of PIZA for use with redshift surveys.

First the galaxies from the survey or simulation are picked out to a radius R. If the survey or simulation is to have the empty regions filled, this is done now. The particle to galaxy ratio is chosen, and PIZA particles are then drawn at random from the same volume, obeying the same sky coverage and selection function as the galaxies. The particles' masses are calculated using the inverse of their selection function. Each galaxy is then assigned particles at random. The final positions of the galaxies are their redshift space positions in the Local Group rest frame. An a priori value for β must be assumed.

Once each galaxy has been assigned particles, swapping can begin in order to minimize Equation (3.13). The masses used in this expression are those of the particles. Each time two galaxy-particle pairs are picked, S and the redshift space trajectories for before and after the swap are calculated. To prevent any trajectories getting longer, the redshift space displacements are also minimized. To speed things up further, only those swaps where the redshift space displacement squared after the swap is less than $(1+\beta)^2$ times that before the swap are attempted. This is equivalent to having a variable search radius, and means that time is not wasted trying swaps which have no chance of being accepted. As described in Section 3.3.2, if the Local Group galaxy is swapped, S is allowed to increase. Swaps are attempted until S has reached a suitable minimum, the required number of attempted swaps being of the order of the number of particles squared.

Once PIZA has been run, the reconstructed peculiar velocity and displacement fields may be found. The galaxy real space displacements are found using the inverse redshift space operator P_{ij}^{-1}. The peculiar velocities may then be found from the real space displacements using $v = \beta\xi$. The reconstructed β may be estimated from the Local Group trajectory assuming the CMB dipole magnitude and using $v = \beta\xi$.

3.6 Tests on PIZA

In order to test the new PIZA method, it has been applied to a set of PSCz-like mock catalogues. The catalogues were extracted from N-body simulations of CDM universes performed by Cole *et al.* (1997). Details of these mock catalogues are given in Branchini *et al.* (2000). Simulations of two CDM cosmologies have been used, a critical model , $\Omega_m = 1$ with $\Gamma = 0.25$, which I shall denote by $\Gamma 0.25$, and a flat model with $\Omega_m = 0.3$ and $\Omega_\Lambda = 0.7$, which I shall denote by $\Lambda 0.7$. There are 3 critical models and 5 flat models. When using the simulations the analytic selection function of Yahil *et al.* (1991) has been used.

$$\phi(r) = Ar^{-2\alpha}\left(\frac{1+r^2}{r_*^2}\right)^{-\gamma} \tag{3.40}$$

if $r > r_*$. Each simulation used has a different set of parameters.

PIZA was tested on the simulations in a variety of ways. PIZA was run on simulations with complete and incomplete sky coverage to ascertain what effect this has on the reconstructed fields, and to test whether the reconstructed dipole was affected by the lack of galaxies in the Galactic Plane. This is important for the PSCz as there are large structures in the Plane, for example the Great Attractor, which are not in the survey but which will affect the motion of the Local Group due to their large mass. When testing PIZA on simulations with incomplete sky coverage, the simulations were given the same sky coverage as PSCz using the PSCz mask (see Chapter 5). When filling the masked regions, galaxies from the simulation are used, as these have 4π sky coverage.

PIZA was also tested with different input values of β to test whether this has an effect on the reconstructions. The actual value of β, which is known for the simulations, was used to test whether in this case PIZA can reconstruct the fields correctly. PIZA was also run on the simulations using a different value for β to see whether it is possible to reconstruct the actual value of β from the resulting reconstructed fields. This is very important as I wish to reconstruct the value of β from the PSCz survey.

To test PIZA, the reconstruction of the radial peculiar velocities of galaxies was tested. This was done, rather than testing the reconstruction of the full 3d velocity field as the

radial peculiar velocities are all that is available from the simulations. The reconstruction of the dipole, as estimated from the trajectory of the Local Group galaxy, was also tested, as this is used to estimate the value of β. The value of β may be inferred from the reconstructed trajectory of the Local Group galaxy using the expression $v = \beta\xi$ and the actual value for the Local Group velocity. To find the radial velocities from the PIZA reconstruction, the inverse redshift space operator is used, along with the *input* value of β.

The PIZA reconstructions for the simulations were also compared with linear theory reconstructions, which were provided by Enzo Branchini (Branchini *et al.* 1999). This was done to test whether PIZA is a more accurate reconstruction method than linear theory, which would be hoped as PIZA is a quasi-non-linear method.

In order to compare the PIZA radial peculiar velocity field with those of the simulations and linear theory, the fields were smoothed as follows. First the galaxies were binned in real space according to their final positions, and the average radial peculiar velocity in each bin was found. These binned velocities were then smoothed using a Gaussian smoothing kernel of radius $20h^{-1}Mpc$. The smoothed radial velocities were then compared, and the slope of the best fit line, and the scatter about the best fit line and about the $x = y$ line, were found. In the figures showing the comparisons, the dotted line indicates the least squares fit to the data. In calculating the least squares fit, the errors used were calculated using the analytic expression for the shot noise error as given in Chapter 2 and in Taylor and Valentine (1999).

It was found that the accuracy of the reconstruction of a simulation varies between different sets of initial conditions (PIZA particles), between different initial assignments of particles to galaxies and also between PIZAs run with different interchanges attempted. This is probably due to the intrinsic randomness of PIZA, the fact that the picking of PIZA particles, assignment of particles to galaxies and choice of interchange attempts are all random processes. The variation in the reconstructed fields may be used as a way to estimate the errors on them. Occasionally PIZA will produce a particularly bad reconstruction. These may be picked out by the large misalignment angle between the reconstructed and CMB dipoles, and by the inferred value of β, which will tend to be

Simulation	Median slope	Median scatter about best fit (kms^{-1})	Median scatter about x=y (kms^{-1})
$\Lambda 0.7$	0.836 ± 0.070	3.493 ± 1.243	7.322 ± 1.591
$\Gamma 0.25$	0.738 ± 0.143	5.689 ± 0.418	11.650 ± 0.873
All	0.807 ± 0.201	5.104 ± 2.974	7.322 ± 6.299

Table 3.1: Comparison between simulations and linear theory reconstructions (from Branchini *et al.* 1999).

either ridiculously large or small.

In what follows, I have quoted the median results. The median is used as a more robust estimator due to the occasional way out answer.

Linear Theory Results

I have compared the linear theory reconstructions of Branchini *et al.* with the simulations in the same way as the PIZA reconstructions and simulations. This then enables a comparison between the two reconstruction methods. The slope and scatter of the linear theory – simulation comparisons are shown in Table 3.1. Two scatters are shown, the scatter of the radial peculiar velocities about the best fit line and the scatter of the radial peculiar velocities about the $x = y$ line. These values may then be compared with the slopes and scatters produced by PIZA for each simulation.

Note that the random errors in these results are calculated from the interquartile range over all the simulations.

3.7 PIZA Results for Empty Mask

The results for PIZA tested on simulations with the masked regions empty are presented in this Section. The values of β reconstructed for each of the simulations are shown in Table A.2, along with the average β and the error due to different initial conditions. The

Simulation	ξ_{LG} (kms^{-1})	θ_{CMB} $(^\circ)$	β_R	β_R/β_T
$\Lambda 0.7$	1386 ± 237	19 ± 7	0.419 ± 0.070	0.843 ± 0.136
$\Gamma 0.25$	641 ± 209	15 ± 3	0.953 ± 0.270	0.953 ± 0.270
All	-	17 ± 8	-	0.880 ± 0.198

Table 3.2: Median dipole results for all simulations with empty mask.

Simulation	Median slope	Median scatter about best fit (kms^{-1})	Median scatter about x=y (kms^{-1})
$\Lambda 0.7$	0.773 ± 0.116	5.010 ± 1.963	6.747 ± 2.094
$\Gamma 0.25$	0.617 ± 0.211	5.845 ± 6.043	10.28 ± 6.712
All	0.682 ± 0.184	5.641 ± 1.702	8.890 ± 4.922

Table 3.3: Median results for PIZA-simulation comparison with empty mask.

fraction of β_{true} reconstructed is shown in Table A.3, again with the average and random error due to different initial conditions. The reconstructed dipole misalignment angle θ_{CMB} is shown in Table A.4. The parameters for the PIZA – simulation comparison are shown in Tables A.5, A.6 and A.7. Note that the random errors for these results are due to the PIZA random initial conditions. The median values for the results over all the simulations are shown in Tables 3.2 and 3.3.

Figure 3.5 shows the distribution of dipole directions with respect to the simulation dipole direction. The simulation dipole is indicated by the red star. It may be seen that there is a fairly wide spread of dipole directions, with the majority of directions being at greater galactic longitudes and latitudes than the simulation dipole. This is likely to be due to the incomplete sky coverage, with structures in the empty regions affecting the simulation dipole but not the reconstructed dipole.

Figure 3.6 shows a histogram of the ratio $\beta_{reconstructed}/\beta_{true}$.

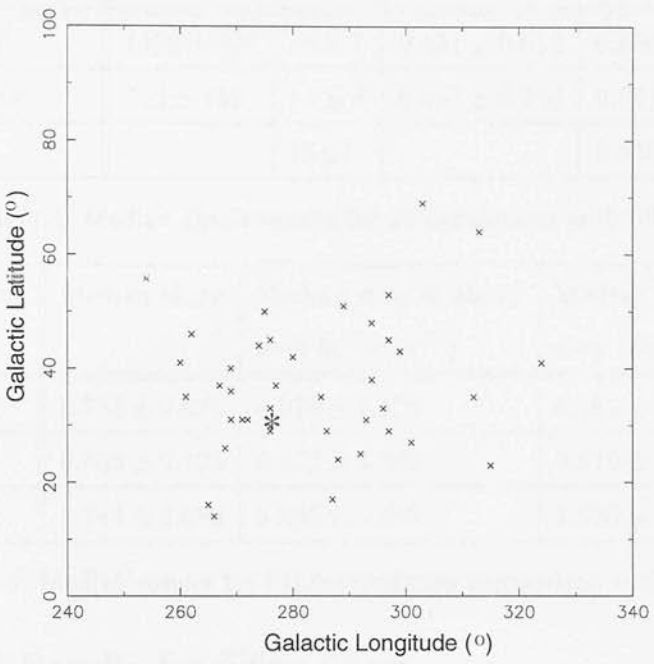

Figure 3.5: Scatter of reconstructed dipole directions about simulation dipole direction for empty mask. The red star shows the position of the simulation dipole.

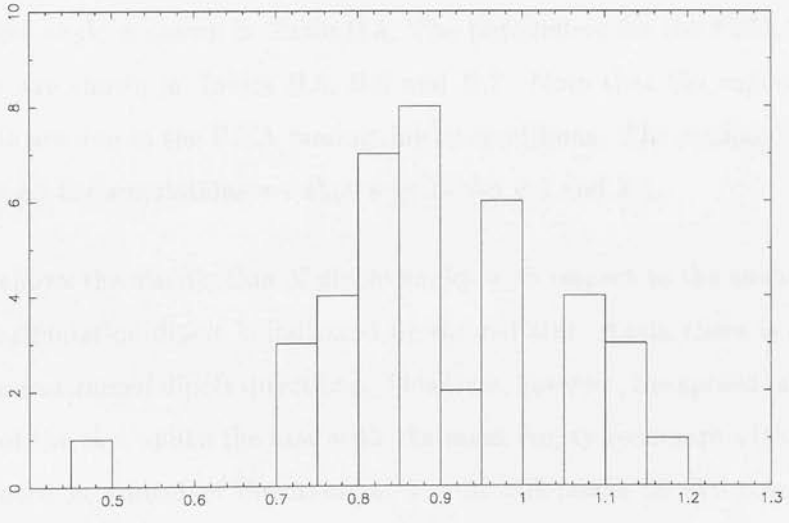

Figure 3.6: Histogram of $\beta_{reconstructed}/\beta_{true}$ for empty mask.

Simulation	ξ_{LG} (kms^{-1})	θ_{CMB} (°)	β_R	β_R/β_T
$\Lambda 0.7$	1409 ± 220	16 ± 7	0.431 ± 0.052	0.850 ± 0.104
$\Gamma 0.25$	715 ± 152	14 ± 8	0.841 ± 0.183	0.841 ± 0.183
All	-	15±7	-	0.850 ± 0.116

Table 3.4: Median dipole results for all simulations with filled mask.

Simulation	Median slope	Median scatter about best fit (kms^{-1})	Median scatter about x=y (kms^{-1})
$\Lambda 0.7$	0.755 ± 0.079	4.978 ± 1.125	6.482 ± 0.218
$\Gamma 0.25$	0.653 ± 0.125	6.452 ± 2.589	9.619 ± 1.952
All	0.744 ± 0.083	5.802 ± 1.835	7.998 ± 2.204

Table 3.5: Median results for PIZA-simulation comparison with filled mask.

3.8 PIZA Results for Filled Mask

The results for PIZA applied to simulations with full-sky coverage are presented in this Section. The values of β reconstructed for each of the simulations are shown in Table B.2, with the average β and the scatter due to different initial conditions. The fraction of β_{true} reconstructed in shown in Table B.3. The reconstructed dipole misalignment angle is shown in Table B.4. The parameters for the PIZA – simulation comparison are shown in Tables B.5, B.6 and B.7. Note that the random errors for these results are due to the PIZA random initial conditions. The median values for the results over all the simulations are shown in Tables 3.4 and 3.5.

Figure 3.7 shows the distribution of dipole angles with respect to the simulation dipole angle. The simulation dipole is indicated by the red star. Again there is a fairly wide spread in reconstructed dipole directions. This time, however, the spread of directions is over more of the sky, unlike the case with the mask empty (compare with Figure 3.5). This difference in spread of directions is due to differences in sky coverage. With galaxies in the plane, the gravitational attraction of these galaxies may pull the dipole direction further towards the plane than if the plane was empty.

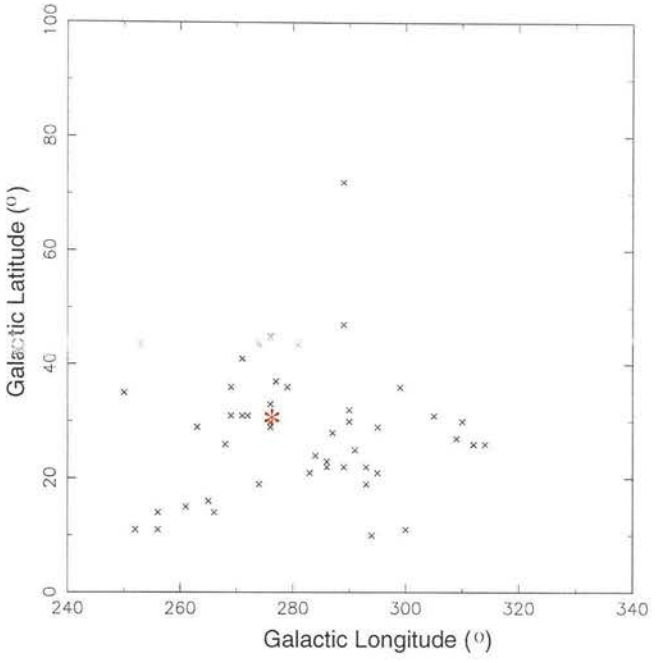

Figure 3.7: Scatter of reconstructed dipole directions about CMB dipole direction for filled mask.

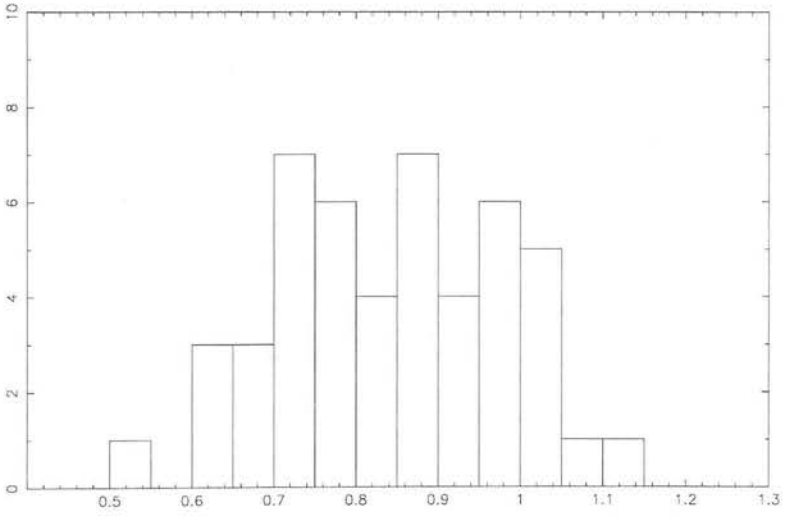

Figure 3.8: Histogram of $\beta_{reconstructed}/\beta_{true}$ for filled mask.

Figure 3.8 shows a histogram of the ratio $\beta_{reconstructed}/\beta_{true}$.

Figures 3.9, 3.10 and 3.11 show the comparison between PIZA, simulation and linear theory radial peculiar velocities for 3 PIZA runs. The left hand panel shows the PIZA–simulation comparison and the right hand panel shows the PIZA–linear theory comparison. The solid line is the $x = y$ line, and the dotted line shows the best fit line to the data. These three figures are typical of the PIZA reconstructions, with the slope and scatters varying about the linear theory values.

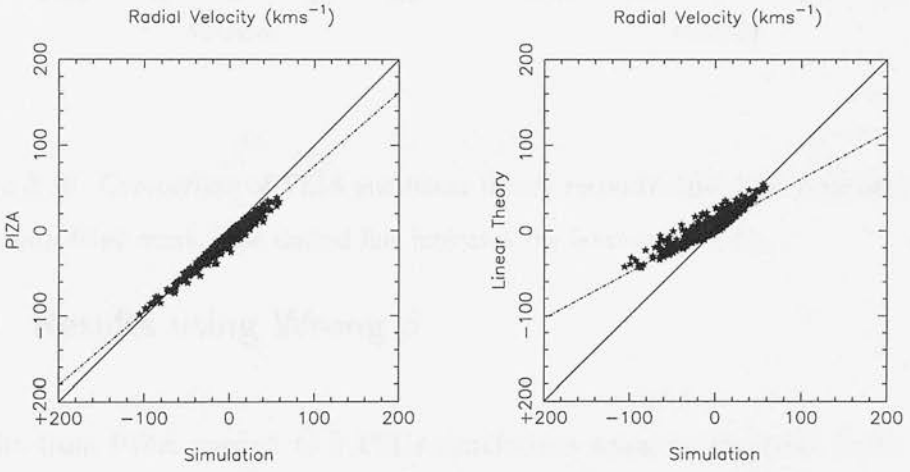

Figure 3.9: Comparison of PIZA and linear theory reconstructions for simulation $\Gamma 0.25/3$ run 4 with filled mask. The dotted line indicates the least-squares fit.

Figures 3.12 and 3.13 show typical PIZA reconstructed velocity fields. The arrow heads indicate the present day real space positions of the galaxies, and the arrow length shows the magnitude of the velocity. The red arrow shows the direction and magnitude of the dipole, as reconstructed from the trajectory of the Local Group galaxy.

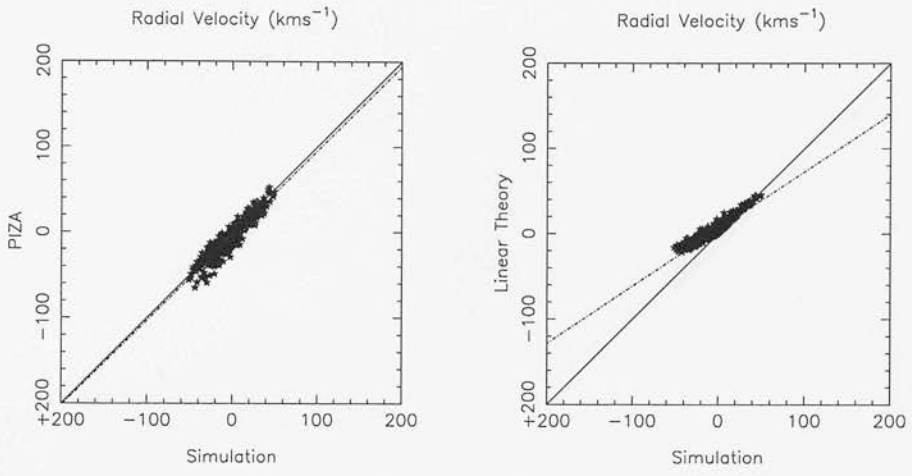

Figure 3.10: Comparison of PIZA and linear theory reconstructions for simulation $\Lambda 0.7/1$ run 1 with filled mask. The dotted line indicates the least-squares fit.

3.9 Results using Wrong β

Results from PIZA applied to 2 PSCz simulations using an incorrect input value of β are presented in this Section. For the $\Gamma 0.25$ simulation, a value of $\beta = 0.497$ was used, and for the $\Lambda 0.7$ simulation a value of $\beta = 1$ was used. Tables showing the reconstructed β, the ratio $\beta_{reconstructed}/\beta true$, the dipole misalignment angle, and the parameters for the comparison with simulation, are shown in Appendix C.

It can be seen by comparing Table B.1 with table C.1 that the reconstructed ξ_{LG} does not depend on the value of the input β. This is very good news, because it means that we can reconstruct the value of β using PIZA with any sensible value for the input β. From Tables C.2 and C.3, it can be seen that the values for β reconstructed using the "wrong" input β is comparable to those reconstructed using the "correct" input β.

I thus conclude that, for sensible values of β, the reconstructed β is insensitive to the input β, and that when reconstructing real redshift surveys, PIZA may be used to reconstruct the true value of β.

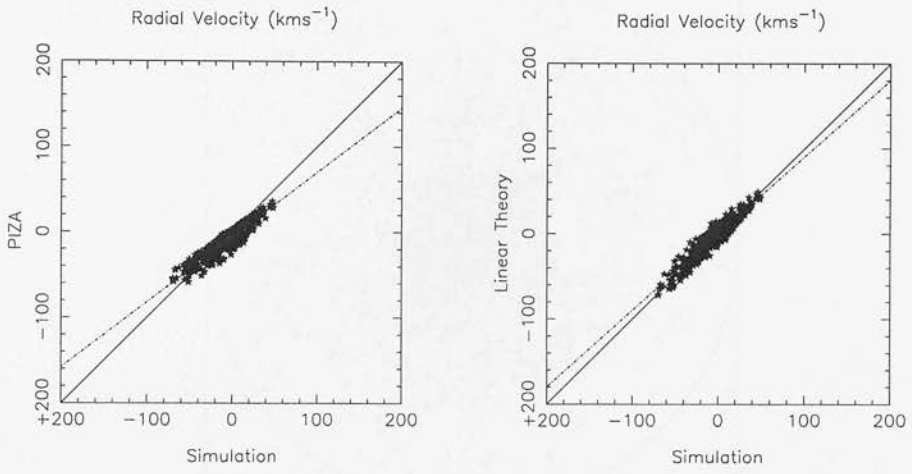

Figure 3.11: Comparison of PIZA and linear theory reconstructions for simulation $\Lambda 0.7/2$ run 4 with filled mask. The dotted line indicates the least-squares fit.

3.10 Discussion

I have tested PIZA on a set of PSCz-like simulations, both with and without the masked regions filled, and with varying values for the input β. I have compared the resulting radial velocity field both with the simulation velocity field and the field reconstructed from the simulation using linear theory.

I have found that the reconstructed β from the dipole is insensitive to the input β, meaning that PIZA may be used to estimate β from the dipole reconstructed from redshift survey.

In studying the effects of sky coverage, I have found that the value of the reconstructed β appears to be unaffected by the lack of galaxies in the plane. The misalignment angle between the reconstructed and CMB dipoles is affected by sky coverage, as might be expected if part of the dipole is caused by structure within the plane. I have found that with the mask empty, the average misalignment angle is $17 \pm 8°$. With the mask filled, the average misalignment angle is $15 \pm 9°$.

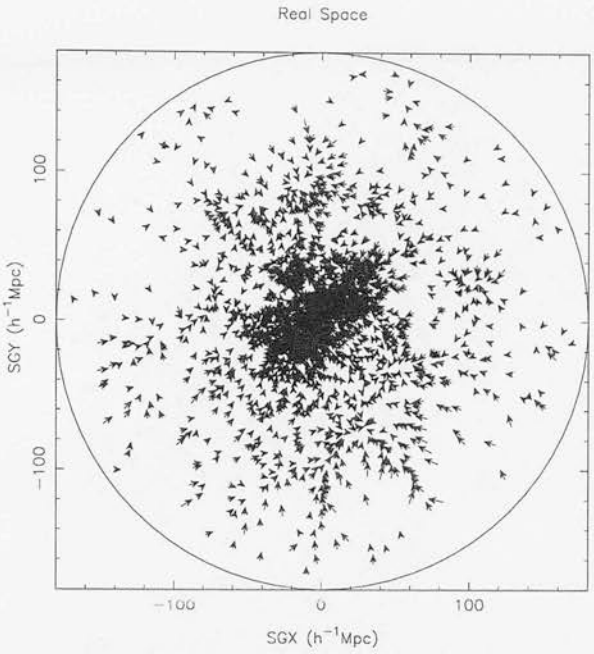

Figure 3.12: Reconstructed velocity field for simulation $\Lambda 0.7/1$ run 1. The arrow heads indicate the present day galaxy positions, the length of the arrow shows the magnitude of the velocity. The red arrow shows the velocity of the Local Group.

It was also found that the slope and scatter in the comparison between reconstructed and simulation velocity fields was better with more complete sky coverage. With the mask empty, the results are: average slope $= 0.682 \pm 0.184$, average scatter about the best fit line $= 5.641 \pm 1.702 kms^{-1}$ and average scatter about $x = y$ line $= 8.890 \pm 4.922 kms^{-1}$. With the mask filled, the results are: average slope $= 0.744 \pm 0.083$, average scatter about the best fit line $= 5.802 \pm 1.835 kms^{-1}$ and average scatter about $x = y$ line $= 7.988 \pm 2.204 kms^{-1}$. Obviously, as β is underestimated by PIZA, the peculiar velocities of galaxies are also underestimated by PIZA. This may also be seen in the comparisons between PIZA and simulations, as the gradients of the slopes are generally less than 1. Of course, for a perfect reconstruction, the gradient of the slope would be equal to 1.

With incomplete sky coverage, the average reconstructed β for $\Lambda 0.7$ simulations is 0.419 ± 0.070 and the average reconstructed β for the $\Gamma 0.25$ simulations is 0.953 ± 0.270. For full sky coverage, the average reconstructed β for $\Lambda 0.7$ simulations is 0.431 ± 0.052 and the average reconstructed β for the $\Gamma 0.25$ simulations is 0.841 ± 0.183.

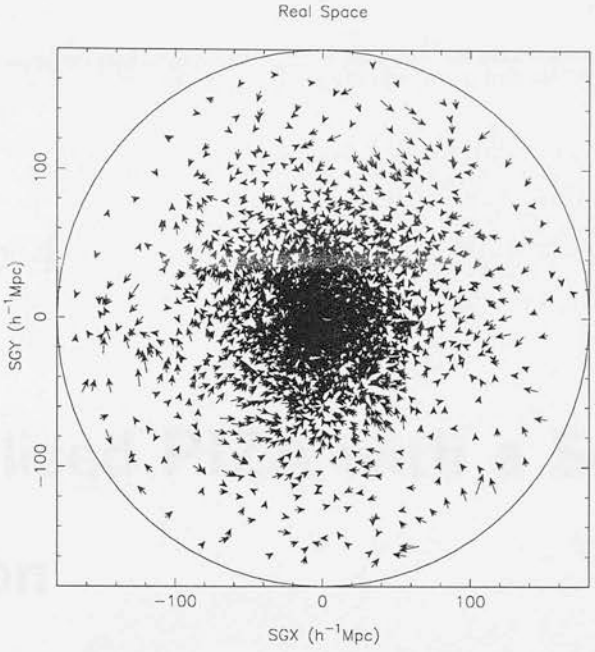

Figure 3.13: Reconstructed velocity field for simulation $\Gamma 0.25/1$ run 1. The arrow heads indicate the present day galaxy positions, the length of the arrow shows the magnitude of the velocity. The red arrow shows the velocity of the Local Group.

In reconstructing the value of β, I have found that PIZA underestimates β by between 10 and 20%. This is most likely to be due to the effects of the selection function, which has not been taken into account in this method so far. The effects of the selection function will be discussed in the next chapter. This could also be due to the fact that the peaks of the density field are underestimated in PIZA, and that the ZA underestimates the velocities.

I have found that the scatter, both about the least squares fit line and the simulation values, is slightly worse in PIZA than in linear theory. This is in agreement with CG97, who found that the scatter in their version of redshift space PIZA was not as good as that in real space PIZA.

Chapter 4

Generalized PIZA with a Selection Function

In the previous Chapter I discussed how to generalize PIZA for use with redshift surveys and presented a generalized method for application to realistic surveys. One problem which I did not discuss in great detail was the inclusion of the selection function. In the previous Chapter it was found that PIZA tended to underestimate β, and this is possibly due to the effects of the selection function which have not been explicitly taken into account. In this Chapter I will discuss the selection function, the problems it can cause when applying PIZA to a flux limited redshift survey, and I will present a generalized PIZA which attempts to take account of the selection function.

Generalizing PIZA for use with surveys with a selection function is not an easy task, for various reasons which will be described in this Chapter. It should be noted here that generalizing PIZA to take account of the selection function has never before been attempted. I have developed a two stage method for applying PIZA to redshift surveys with a selection function. Two separate stages are necessary because there are two possibly conflicting conditions to satisfy – the action S must be minimized and the mass of each galaxy should be as close as possible to the sum of the mass of its particles. To do this, in stage two the constraint of equal numbers of particles per galaxy has been removed. The first stage of the method is PIZA as described in Section 3.5 of

Chapter 3, and will not be described further in this Chapter.

In Section 4.1 the selection function is discussed in more detail. Section 4.2 discusses the problems of taking account of the selection function in PIZA. In Section 4.3 I introduce my new two stage PIZA method, MASSPIZA, and discuss the main parts of the method in some detail. In Section 4.5 I describe the final version of MASSPIZA that I have chosen to use to reconstruct velocity fields from redshift surveys. Section 4.6 presents the results of tests on MASSPIZA using the PSCz-like simulations. In Section 4.7 the conclusions drawn from these tests are presented. This work is briefly discussed in Valentine, Saunders and Taylor (2000).

4.1 The Selection Function

Many redshift surveys are flux limited, with the number density of survey objects decreasing with increasing redshift. This occurs as galaxies at greater distances must be brighter to be seen above the flux limit. This decrease in objects with distance is quantified by the survey selection function, $\phi(r)$.

The decrease in survey objects with increasing distance is clearly seen in Figure 4.1, which shows the n(z) histogram for one of the PSCz simulations, the number of objects in redshift bins as a function of redshift. This Figure shows that, after a peak at around a redshift of $5000 kms^{-1}$, the number of objects decreases with increasing redshift.

When reconstructing the velocity field from a flux limited survey, account must be taken of those galaxies that fall below the flux limit of the survey. Obviously those galaxies will affect the velocity field through their gravitational attraction whether they are seen or not. The galaxies in the survey at greater distances have to represent a larger fraction of the underlying galaxy distribution. To do this, each galaxy is assigned a weight of

$$M_{\text{galaxy}} = \frac{1}{\phi(r)} \tag{4.1}$$

These weights are then used in this method as effective galaxy masses.

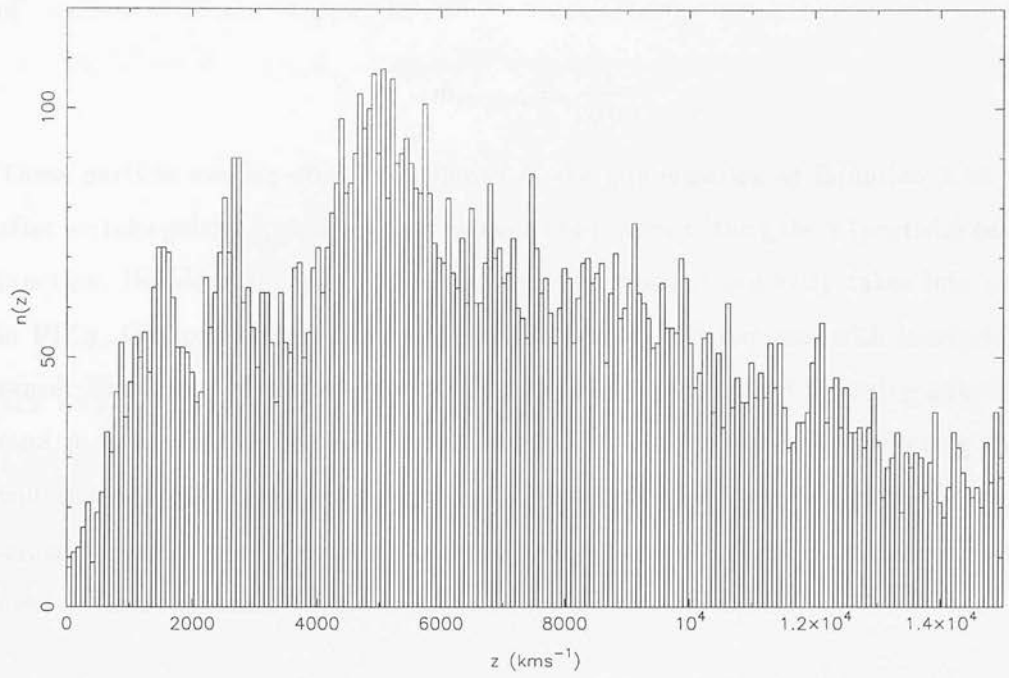

Figure 4.1: n(z) histogram for one of the PSCz simulations.

The distance r used in the expression 4.1 must be the real space distance of the galaxy and not the redshift space distance. If the redshift space positions are used in the expression, the rocket effect (Kaiser 1987) becomes a problem. This occurs because out flowing galaxies, which have redshift positions greater than their real space positions, are assigned weights that are too large. The real space positions of the galaxies are found using the inverse redshift space operator.

4.2 PIZA with a selection function

In the generalized PIZA described in the previous Chapter, the selection function was taken account of in two ways. First, the PIZA particles obey the same selection function as the galaxies, with normalization such that

$$\phi_{particles} = \nu \phi_{galaxies} \tag{4.2}$$

where ν is the particle to galaxy ratio. Second, the PIZA particles are assigned weights of

$$m_{particle} = \frac{1}{\nu\phi(r)} \tag{4.3}$$

These particle weights are then included in the minimization of Equation 3.20. Hereafter we take galaxy (particle) mass to mean the inverse of the galaxy (particle) selection function. However, the galaxy selection function was not explicitly taken into account in PIZA. Obviously the galaxy and particle masses will increase with increasing distance. The effects of the selection function in PIZA are: a) that inflowing galaxies will tend to have particles mapped onto them that are too heavy, and outflowing galaxies will have particles that are too light; and b) that galaxies at greater distances are heavier, so that they need heavier particles to be mapped onto them. It is these effects that need to be overcome.

As we assign particles of variable mass to galaxies of variable mass, we must try to get

$$M_{\text{galaxy}} = \sum m_{\text{particles}} \tag{4.4}$$

for each galaxy.

One possible method to do this would be to add an extra constraint to S of the form

$$S_{mass} = \lambda \sum_{\text{galaxies}} \left(\frac{1}{\phi(r_{galaxies})} - \sum_i m_i \right)^2 \tag{4.5}$$

where λ is a Lagrange multiplier. The inner sum is over particles assigned to a galaxy, and the outer sum is over all galaxies.

The expression to be minimized then becomes

$$S_{TOT} = S + S_{mass} \tag{4.6}$$

It should be obvious that setting $\lambda = 0$ gives the usual minimization of S. For most other values of λ the action cools to a false minimum. Too small a value of λ will not give any weight to the mass minimization, and will lead to similar results as those from the normal PIZA minimization. Too large a value will give the mass minimization too

much weight and the minimization of S will become unimportant. In this case all the reconstructed galaxy trajectories will be purely radial, with the selection function of the galaxy and the sum of the particles' selection functions being exactly equal.

Choosing a suitable value for λ is difficult, as described above, and PIZA using this method tends to converge to false minima. For these reasons, I have rejected this method and separated the procedure into two steps.

The first step of the new method concentrates on minimizing the action, and is the new PIZA method as described in Chapter 3. It will not be discussed further in this Chapter. The second step of the new method attempts to improve on the results of the first step by equalizing the galaxy and particle masses whilst continuing to minimize the action. It is this second step that is the subject of the remainder of this Chapter.

4.3 PIZA Step two – MASSPIZA

As I mentioned above, the aim of this step is to achieve the equality in Equation 4.4 for each galaxy. In order to do this, the constraint of equal particles per galaxy used in PIZA has been removed. MASSPIZA then assigns heavier galaxies more particles than light galaxies, whilst continuing to minimize S.

MASSPIZA takes as its starting point the results of the generalized PIZA of the previous Chapter, assuming that those results have reached somewhere close to the minimum of S. It then attempts to improve on those results by taking the selection function into account.

For this step, both the particle and galaxy masses are needed. These masses are found as described above using their inverse selection functions. The particle masses are then rescaled such that

$$\sum M_{galaxies} = \sum m_{particles} \tag{4.7}$$

This rescaling of masses does not change them significantly, but it hopefully means that achieving the equality in Equation (4.4) will be easier as the total masses in particles

and galaxies will be the same.

I shall now describe the method I have devised to implement the idea of equating particle and galaxy masses.

4.3.1 Basic Method

In an ideal world it would be possible to get the mass of each galaxy exactly equal to the mass of its particles. Unfortunately, this is far from an ideal world, and instead we have to be content to get the masses as close as possible. Some way is needed to decide how close is "close enough". To do this, first the mass ratio

$$R_m = \frac{M_{galaxy}}{m_{particles}} \tag{4.8}$$

is evaluated for each galaxy. Of course, $R_m = 1$ is equivalent to the equality in Equation (4.4). We then need to decide which galaxies have R_m close enough to 1.

To decide which galaxies have R_m close enough to 1, a region of values of R_m, the *mass tolerance region* is defined. The region obviously contains the value $R_m = 1$. The size of the tolerance region is discussed in more detail in Section 4.3.2.

The tolerance region is shown schematically in Figure 4.2. It can be seen that for those galaxies with R_m outside the tolerance region, they have either

$$M_{galaxy} < m_{particles} \tag{4.9}$$

or

$$M_{galaxy} > m_{particles}. \tag{4.10}$$

Those galaxies with $M_{galaxy} < m_{particles}$ or $R_m < 1$ have too many particles assigned to them, and those with $M_{galaxy} > m_{particles}$ or $R_m > 1$ have too few particles. Those galaxies with R_m far from 1 are said to have a large *mass discrepancy*. In MASSPIZA, particles are then reassigned from galaxies with $R_m < 1$ to galaxies with $R_m > 1$. The method used to reassign the particles is described below in Section 4.3.3.

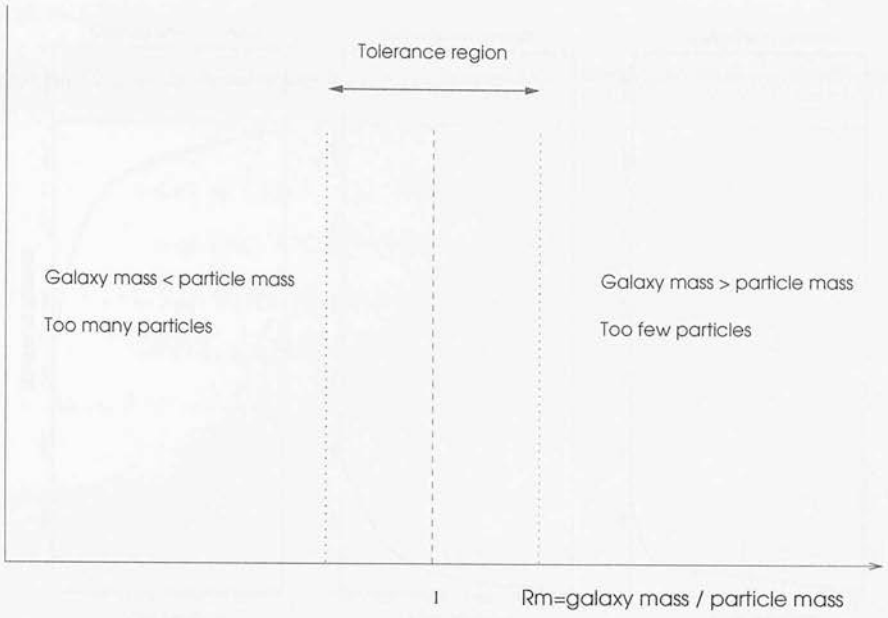

Figure 4.2: Schematic diagram of the MASSPIZA mass tolerance region.

The exception to this particle reassignment is the Local Group galaxy. The selection function is undefined at the origin, and instead of calculating the mass ratio we simply hold the number of particles fixed for the Local Group galaxy.

After particle reassignment, the minimization of S is carried out again until a suitable minimum in S is reached. This minimization is the same as that described in the previous Chapter, but conserving the new individual particle to galaxy ratios. The number of swaps needed here should be less than that needed in the first PIZA step since by the time MASSPIZA is carried out S should be somewhere near the minimum, and so fewer trajectories will need minimizing. The particle reassignment will tend to introduce a few long trajectories, but these should be minimized fairly quickly. The procedure of calculating the mass ratios, reassigning particles and then minimizing S is termed a *Mass Iteration*. Mass iterations are repeated until as many galaxies as possible have R_m within the tolerance region, which I shall term *mass convergence*. Figure 4.3 shows how the numbers of galaxies with the right mass, too many and too few particles changes with mass iteration.

The next step is to decide upon the specifics of the method: the size of the tolerance

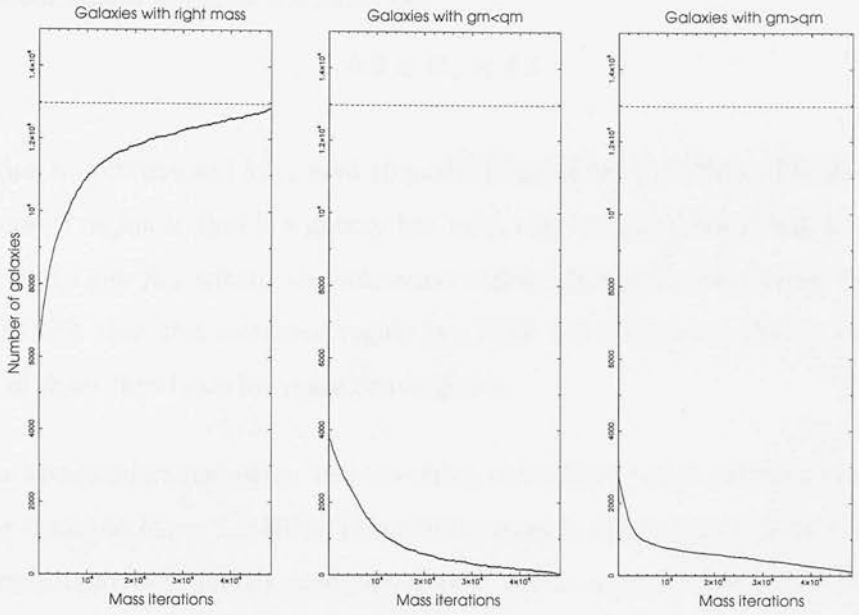

Figure 4.3: Typical mass curves for a PSCz simulation. The curves show how the number of galaxies with mass convergence, with too few and too many particles changes with mass iteration. The red line indicates the total number of galaxies.

region, the method of reassigning particles and the amount of swaps attempted per mass iteration. These will be discussed in the following Sections.

4.3.2 Mass Tolerance Region

The tolerance region is an important part of MASSPIZA, and its size is crucial to the accuracy of the reconstruction. If the tolerance region is thin, it will be hard for galaxies to get into it as the range of acceptable values of R_m is small. It will take a large number of mass iterations to reach mass convergence, perhaps of order of the number of galaxies in the reconstruction. The advantage of a thin tolerance region is that those galaxies within it will hopefully have accurate trajectories. The converse is true for a wider tolerance region. In this case, it will be easier for galaxies to get into the region, and fewer mass iterations will be needed for mass convergence, at the expense of less accurate trajectories.

In developing MASSPIZA, a variety of tolerance regions have been tried. Initially I

tried a fixed region of $R_m = 1 \pm 10\%$. i.e.

$$0.9 < R_m < 1.1 \tag{4.11}$$

This region was chosen as I have used 10 particles per galaxy in PIZA. The disadvantage of this size of region is that if a galaxy has only, say, two particles it will be extremely hard for it to get R_m within the tolerance region. It was found during the running of MASSPIZA that this tolerance region is a little too strict, and that it took a large number of mass iterations for mass convergence.

Since the above tolerance region was too strict, other fixed width tolerance regions were tried, for example $R_m = 1 \pm 50\%$. This wide tolerance region was used as it gives mass convergence relatively quickly, and therefore could be used to check that MASSPIZA was working correctly. Once it was concluded that MASSPIZA was indeed working as it should, this wide tolerance region was rejected.

It was decided to abandon the fixed width tolerance region in favour of a variable width tolerance region whose size depends upon the number of particles assigned to the galaxy in question. This then bypasses the problem outlined above for fixed width tolerance regions, with the tolerance region being larger for galaxies assigned with fewer galaxies.

The first variable width mass tolerance region that I used is defined by

$$\frac{1}{1+\frac{1}{\nu}} \leq R_m \leq 1 + \frac{1}{\nu} \tag{4.12}$$

where again ν is the number of particles assigned to that galaxy. For galaxies with $\nu = 10$, this is approximately the same as the fixed $R_m = 1 \pm 10\%$ region used above.

Again it was found that this tolerance region was a bit too strict. A less harsh tolerance region was defined such that

$$\frac{1}{1+\frac{1}{\sqrt{\nu}}} \leq R_m \leq 1 + \frac{1}{\sqrt{\nu}} \tag{4.13}$$

With this tolerance region, the error on the mass of a galaxy is equal to the shot noise on the number of particles assigned to that galaxy. This tolerance region appears to

work much better, and it is used in the rest of this work. Figure 4.4 shows two views of the PIZA displacement field in the Supergalactic Plane for one of the PSCz simulations. The left hand panel shows the displacement field for all the galaxies in a slice between $SGZ = -15h^{-1}Mpc$ and $SGZ = 15h^{-1}Mpc$. As usual, the red arrow shows the trajectory of the Local Group galaxy, and indicates the direction of the dipole. The right hand panel shows the same displacement field, but this time showing only those galaxies with masses outside the tolerance region. The red arrows in this case indicate those galaxies with too many particles and the green arrows indicate those galaxies with too few particles. For simplicity, the trajectories of galaxies with mass convergence have been omitted. It can be seen that those galaxies with too many particles all have inflowing trajectories and those with too few particles all have outflowing trajectories. This is what would be expected, as the inverse of the selection function increases with increasing distance. Thus the mass of a galaxy that is outflowing will be larger than the mass of its particles, leading it to need more particles, and the mass of an inflowing galaxy will be smaller than the mass of its particles, leading it to need fewer. It may be seen by comparing the two panels of Figure 4.4 that there is a minimum length of trajectory for those galaxies without mass convergence, and that all the galaxies with shorter length trajectories have mass convergence. As the mass discrepancy between galaxy and particle mass gets larger, the length of the galaxy's trajectory will become larger, due to the inverse selection function. As there is a cut-off in mass discrepancy due to the tolerance region, there will also be a cut-off in trajectory length, with galaxies having trajectories below that cut-off having mass convergence.

4.3.3 Particle Reassignment

The main idea of MASSPIZA is to reassign particles from galaxies with too many to those with too few, in order to give them the right amount of mass. Thus it is important that an suitable reassignment method is found. Since particle reassignment is carried out at the beginning of each mass iteration, it is vital that a quick and efficient method is used.

Particle reassignment is carried out once the mass ratios have been calculated and the

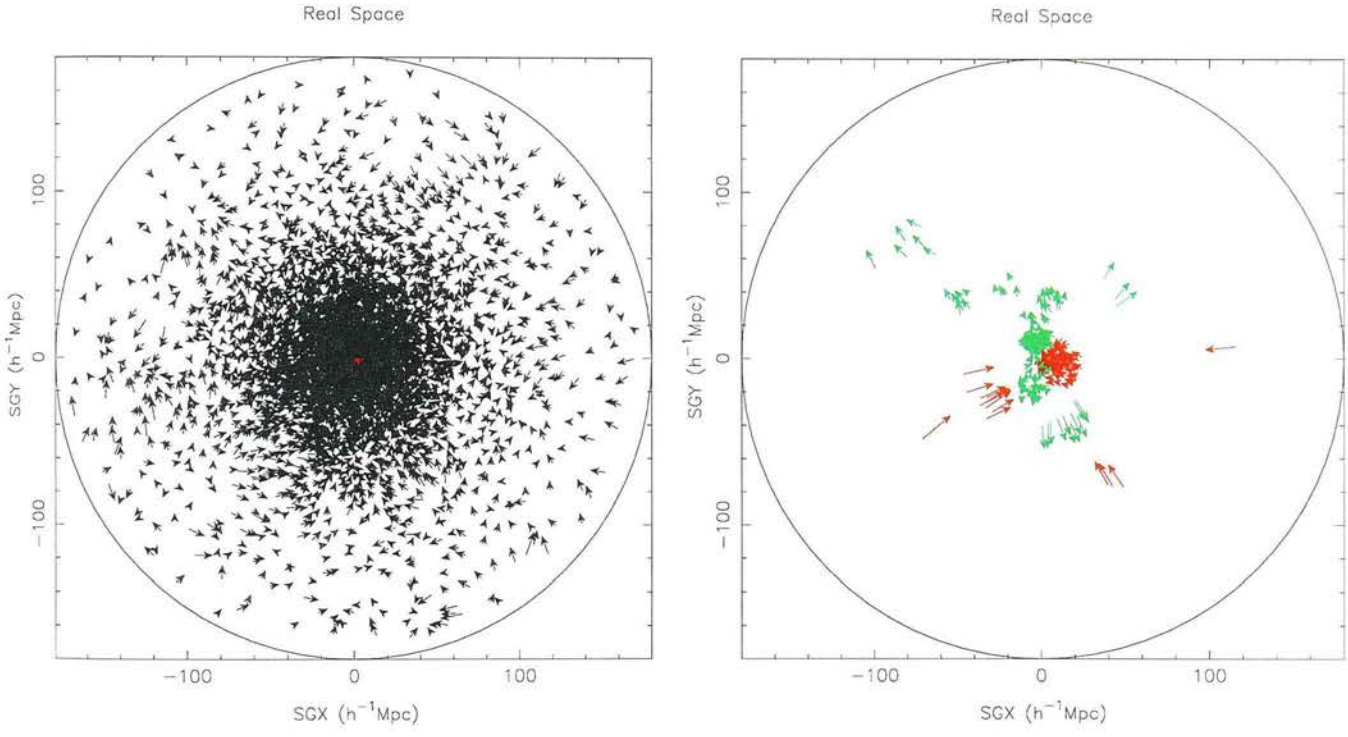

Figure 4.4: Two views of the PIZA displacement field in the Supergalactic Plane for a PSCz simulation. The left hand panel shows those galaxies in a slice between $SGZ = -15$ and $15h^{-1}Mpc$, the red arrow indicates the trajectory of the Local Group galaxy. The right hand panel shows those galaxies in the same slice with masses outside the tolerance region. Red indicates that the galaxy has too many particles, green indicates that the galaxy has too few particles.

galaxies needing reassignment have been found. Two lists of galaxies, one of galaxies needing fewer particles and one of galaxies needing more particles, are formed. A one–to–one mapping between these two lists must then be found, such that one particle from a galaxy with too many particles is mapped to a galaxy with too few particles.

Producing galaxy lists

The one–to–one mapping between galaxies can obviously only be done between pairs of galaxies, say n galaxy pairs. In general the two galaxy lists produced after the R_ms are calculated will be of different lengths, and therefore the longer list must be shortened in order to produce two lists of length n. There are various options for reducing the longer list, as follows:

The simplest method is to pick the first n galaxies in the longer list. Although this method has the advantage that it is easy to implement, it has the drawback that the galaxies neglected in one mass iteration are likely to be neglected again in the subsequent mass iterations, and hence never undergo particle reassignment and never achieve mass convergence

A better method is to select the n galaxies at random from the longer list. This of course has the advantage over the previous method that each galaxy has an equal chance of having particle reassignment.

The method I have chosen to use is to pick the n galaxies from the longer list with R_m furthest from 1. This means that the galaxies in the longer list with the worst discrepancy between galaxy and particle mass are involved in particle reassignment.

Galaxy to galaxy mapping

Having produced the two lists of n galaxies, the mapping between the galaxies in the two lists must be chosen. Once this mapping has been chosen, particles may then be taken from the galaxy in the list of those with too many particles and assigned to the

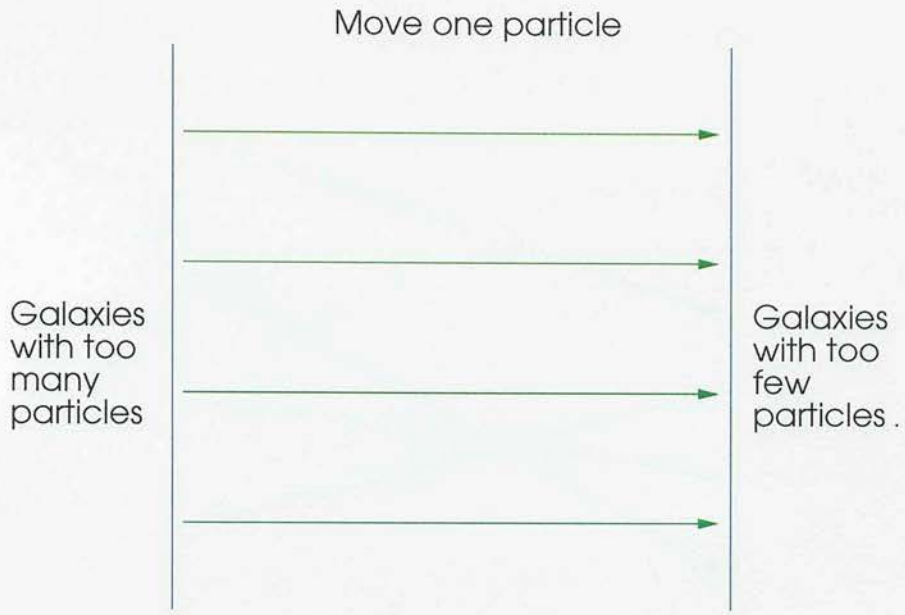

Figure 4.5: Particle reassignment method 1: map galaxies from first list to galaxies in corresponding position in second list.

galaxy it is mapped to in the other list.

The simplest mapping method that I used was to map from a galaxy in the "too many" list to the galaxy at the corresponding position in the "too few" list, i.e. the first galaxy from one list mapped to the first galaxy in the other list, the second to the second and so on. This mapping method is shown schematically in Figure 4.5. Whilst this method is simple and easy to implement, it has the disadvantage that the mapping will tend to reassign particles between the same galaxies in consecutive mass iterations. For this reason, I have chosen not to use this method.

An alternative mapping method which I have used is to choose the mapping at random, as shown in Figure 4.6. This method of course has none of the disadvantages of the above method. This method is ideal for particle reassignment, but I experimented with other methods in order to find a method which achieved mass convergence more rapidly.

A more complex mapping method which I developed was to order the two galaxy lists according to their R_m. The "too many particle" list was ordered in descending order

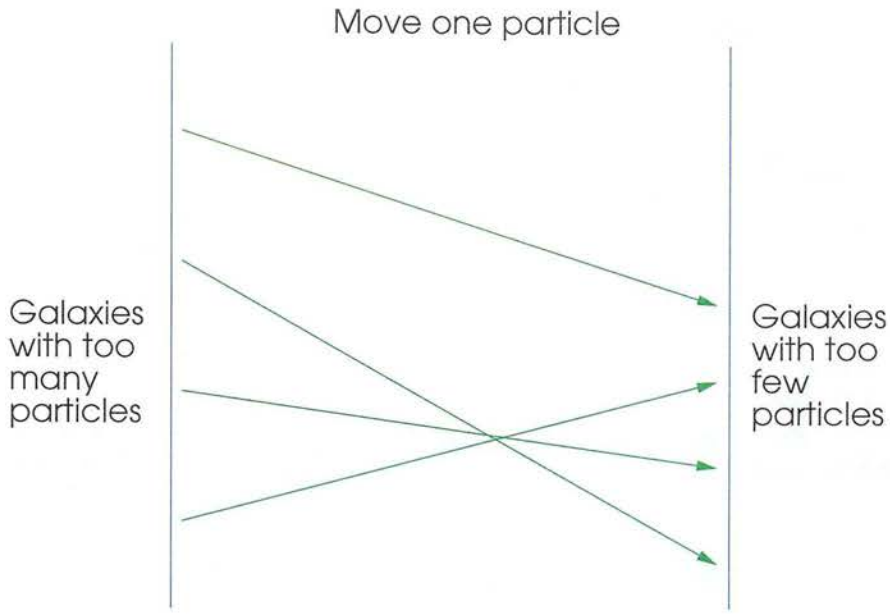

Figure 4.6: Particle reassignment method 2: map galaxies from first list at random to those in second list.

and the "too few particle" list was ordered in ascending order. Then the galaxy with the smallest R_m in the "too many" list was mapped to the galaxy with the largest R_m in the "too few" list, and so on down the lists. This method is shown schematically in Figure 4.7. This method assumes that galaxies with mass discrepancies of a similar magnitude, whether larger or smaller than $R_m = 1$, will be mapped together, and that this will help achieve mass convergence quickly. This method, and the other two above, all produce mass curves similar to that shown in Figure 4.3.

The above three mapping methods work fairly well, and mass convergence is achieved with them for the majority of galaxies. However, the drawback of these methods is that they may introduce large trajectories across the survey volume as particles are reassigned between galaxies at large distances from each other. Whilst these trajectories should be removed once S is minimized again, it would obviously be better if these trajectories could be kept as short as possible during reassignment. Therefore I developed another method that maps each galaxy with $R_m > 1$ to the closest possible galaxy with $R_m < 1$. This method is shown schematically in Figure 4.8. This way the lengths of trajectories introduced by particle reassignment are kept to a minimum. Unfortunately this mapping method does not achieve mass convergence. The number of galaxies with

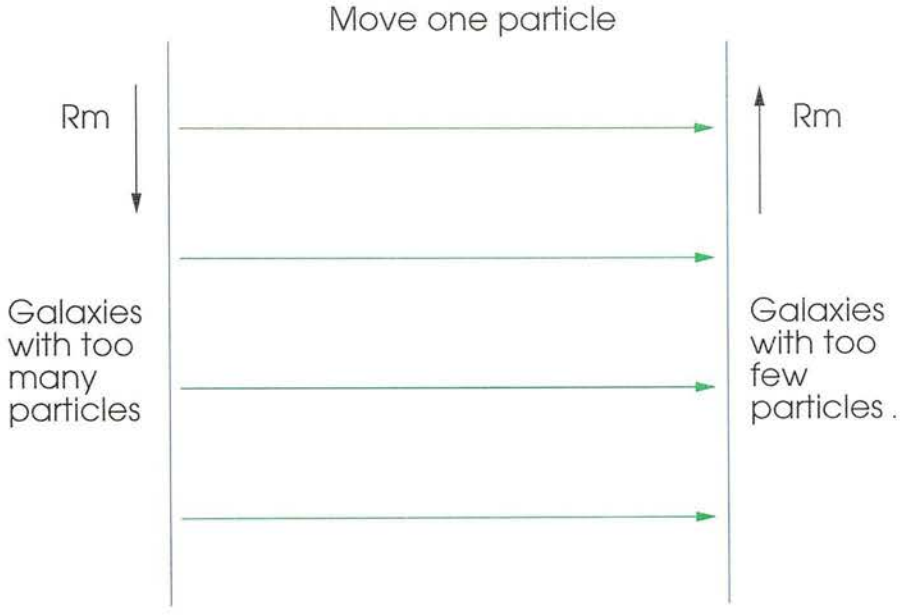

Figure 4.7: Particle reassignment method 3: map galaxies with similar sized mass discrepancies from both lists together.

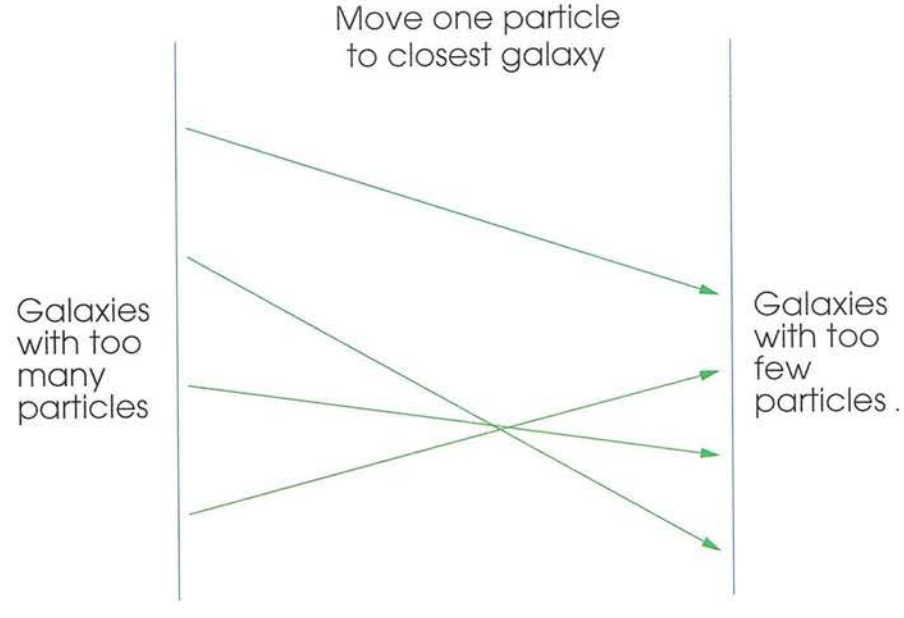

Figure 4.8: Particle reassignment method 4: map galaxies from first list to closest galaxy in second list.

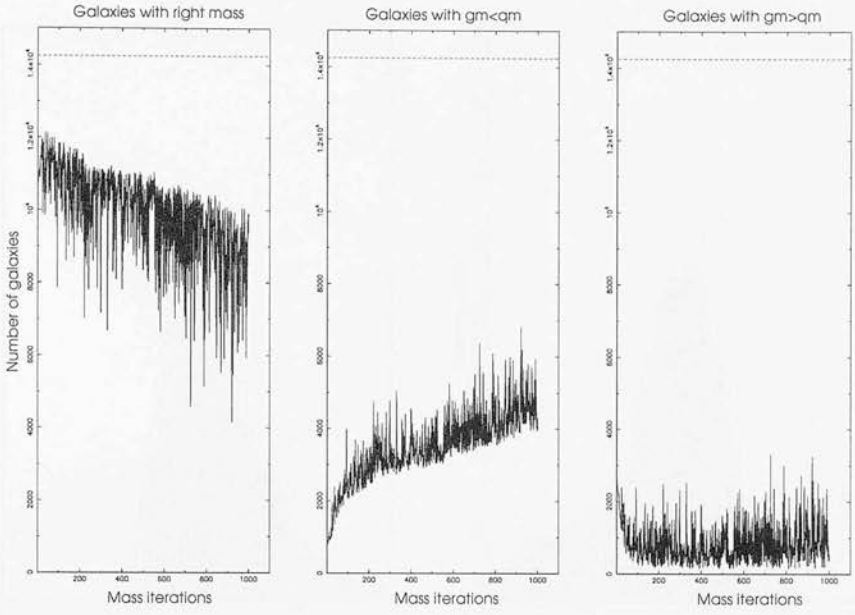

Figure 4.9: Mass curves for MASSPIZA using particles reassignment method 4. The red line indicates the total number of galaxies.

mass convergence fluctuates widely with mass iterations and the general trend is for this number to decrease. This is shown in Figure 4.9. For this reason I have chosen not to use this method.

Having experimented with the 4 particle reassignment methods described above, I have chosen to use the method which maps galaxies with similar sized mass discrepancies together, as shown in Figure 4.7, as it seems to be the best method for achieving mass convergence. This is the method used in the remainder of this work.

Once the mapping between the galaxies in each list has been chosen, the particle reassignment may be done. This is done simply by choosing one of the particles at random from each galaxy with too many particles and reassigning it to the galaxy's partner in the other list. It is of course possible to reassign particles for all n galaxy pairs or any other number of galaxy pairs per mass iteration. For reasons of speed of mass convergence I have chosen to carry out reassignment for all n galaxies per mass iteration. Once reassignment has been done, it is then possible to again minimize S.

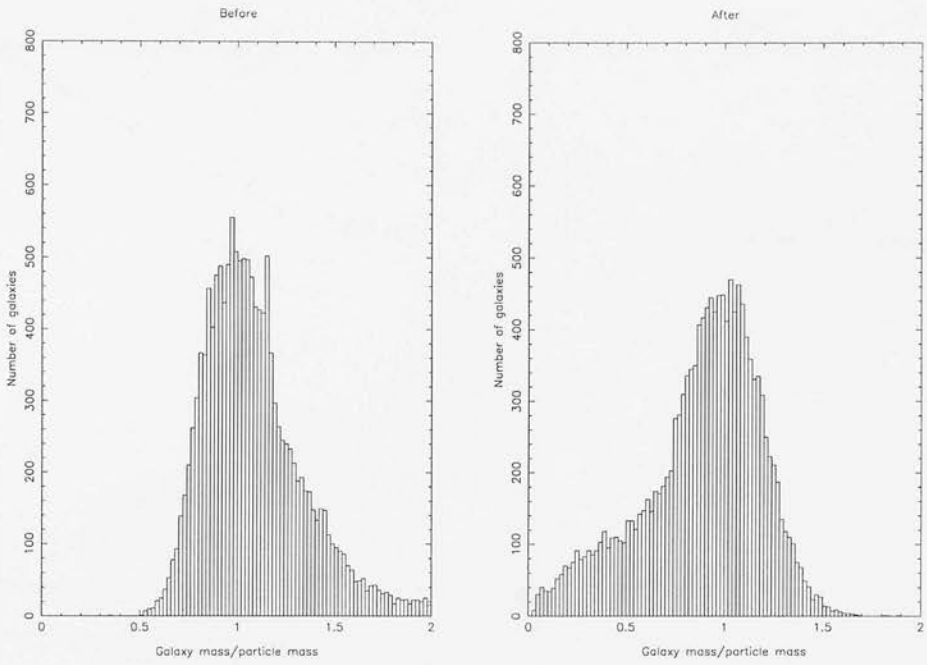

Figure 4.10: Histograms of mass ratios of galaxies in a PSCz simulation before (left hand panel) and after (right hand panel) MASSPIZA using particles reassignment method 4 has been applied.

4.3.4 Minimizing S

The main idea behind PIZA is to reconstruct galaxy trajectories by minimizing S. Therefore S must also be minimized in MASSPIZA. This is done once particle reassignment has been carried out. Hopefully PIZA will have reached a point somewhere near the minimum of S, and the particle reassignment is designed to introduce trajectories as short as possible, so the number of swaps needed in a mass iteration should be much less than the number needed in the first PIZA stage.

Whilst developing MASSPIZA I have experimented with using different numbers of attempted swaps per mass iteration. I have chosen to use $10 \times np$ attempted swaps per mass iteration, where np is the total number of particles. This value is used in the remainder of this work. I have found that attempting more swaps than this per mass iteration does not appreciably improve the reconstruction and only increases the time taken for the reconstruction to run.

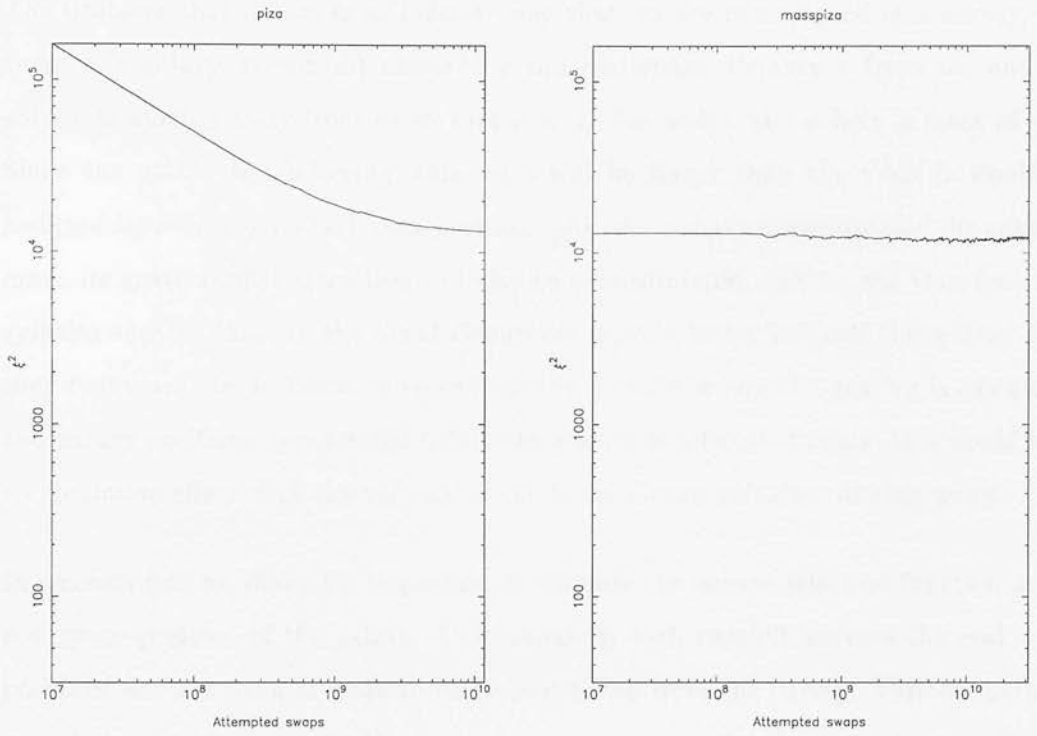

Figure 4.11: Cooling curves for PIZA (left hand panel) and MASSPIZA (right hand panel) applied to a PSCz simulation.

After particle reassignment, some long trajectories are introduced due to particles being reassigned between galaxies with some distance between them. This results in an increase in S. This increase in S is generally fairly small, and in any case the long trajectories will be removed by again minimizing S. A typical cooling curve produced by MASSPIZA is shown in the right hand panel of Figure 4.11, with the cooling curve for the stage 1 of PIZA shown in the left hand panel.

4.4 The Rocket Effect

The rocket effect (Kaiser 1987) causes problems when reconstructing velocity and density fields from flux limited redshift surveys due to the way the selection function is used to weight the galaxies, as in Equation 4.1. The problem arises when the redshift distance is used to evaluate the selection function rather than the real space distance.

The problem that occurs is as follows. Say that we are reconstructing a survey, and there is a galaxy at redshift distance s and real space distance r from us, and the galaxy is moving away from us so that $r < s$. We assign the galaxy a mass of $\frac{1}{\phi(s)}$. Since the galaxy is outflowing, this mass will be larger than the mass it would be assigned according to its real space position, $\frac{1}{\phi(r)}$. As we have overestimated the galaxy's mass, its gravitational attraction will also be overestimated, and we will thus find that galaxies such as those in the Local Group are moving faster towards this galaxy than they really are. In an iterative reconstruction method where the gravity is calculated and galaxy positions are updated before the gravity is calculated again, this would have a cumulative effect with the velocity of the Local Group galaxies running away.

In reconstructions, then, it is important to evaluate the inverse selection function at the real space position of the galaxy. Unfortunately, with redshift surveys the real space positions are unknown and are to be reconstructed from the survey. Various methods have been used to estimate the real space positions as the reconstruction method is applied, for example Yahil *et al.* (1991) use an iterative linear theory method where the real space positions are estimated using the results of the previous iteration. The method I use in MASSPIZA is similar, with the first iteration using the results of the PIZA reconstruction to find the real space positions with the inverse redshift space operator (Equation 3.35), and successive iterations using the results of the previous iteration.

4.5 Final version of MASSPIZA

In this Section I will describe the final version of MASSPIZA which I have used for reconstructing cosmological fields from redshift surveys.

MASSPIZA starts with the results from PIZA. The real space positions of the galaxies are found, and then the galaxy masses are evaluated using Equation 4.1. The total mass of particles assigned to each galaxy is found, and the mass ratio R_m is calculated. Using R_m, those galaxies needing more or less particles are found, and n of each type of galaxy are chosen. The mapping between the two lists of n galaxies is chosen, and

Simulation	l	b	ξ_{LG}	$\angle_{CMB}$	Inferred β	β_R/β_T
Λ0.7/1	247	41	2276	26	0.240	0.483
Λ0.7/2	301	34	1819	22	0.309	0.622
Λ0.7/3	288	28	2321	11	0.268	0.539
Λ0.7/4	300	43	2102	23	0.278	0.559
Λ0.7/5	247	14	2084	31	0.280	0.563
Γ0.25/1	288	22	659	13	0.861	0.861
Γ0.25/2	292	14	602	22	1.025	1.025
Γ0.25/3	272	43	1977	13	0.281	0.281

Table 4.1: MASSPIZA reconstructed dipole directions and magnitudes, and reconstructed β for all simulations with mask filled.

particles are then reassigned. Once particle reassignment has been done, S is again minimized. Mass iterations are then repeated until as many galaxies as possible have mass convergence. Typically MASSPIZA can achieve mass convergence for $\sim 95\%$ of the galaxies.

4.6 MASSPIZA Test Results

MASSPIZA has been tested on the PSCz simulations in the same way as PIZA, as described in Section 3.6. The MASSPIZA method is that as described in the previous Section. The input β was the true value for the simulation. I have applied MASSPIZA to the results of PIZA with the mask filled. For each simulation I have used the PIZA results from run number 1. Table 4.1 shows the reconstructed dipoles for all the simulations. Table 4.2 shows the parameters for the MASSPIZA-simulation comparisons. Note that the random errors for these results are due to the PIZA random initial conditions. The medians of the results are shown in Tables 4.3 and 4.4.

Simulation	Gradient of slope	Scatter about best fit line (kms^{-1})	Scatter about x=y (kms^{-1})
$\Lambda 0.7/1$	1.140	7.398	8.014
$\Lambda 0.7/2$	0.845	6.200	7.338
$\Lambda 0.7/3$	0.816	4.650	5.150
$\Lambda 0.7/4$	0.780	3.754	6.126
$\Lambda 0.7/5$	0.886	3.577	3.833
$\Gamma 0.25/1$	0.613	10.82	12.30
$\Gamma 0.25/2$	0.605	5.566	10.34
$\Gamma 0.25/3$	0.880	5.070	7.361

Table 4.2: Comparison between MASSPIZA and simulations with mask filled.

Simulation	ξ_{LG} (kms^{-1})	θ_{CMB} (°)	β_R	β_R/β_T
$\Lambda 0.7$	2102 ± 198	23 ± 7	0.258 ± 0.025	0.559 ± 0.050
$\Gamma 0.25$	659 ± 640	13 ± 5	0.861 ± 0.391	0.861 ± 0.391
All	-	22 ± 7	-	0.561 ± 0.230

Table 4.3: Median dipole results for all simulations with filled mask.

Simulation	Median slope	Median scatter about best fit (kms^{-1})	Median scatter about x=y (kms^{-1})
$\Lambda 0.7$	0.845 ± 0.143	4.650 ± 1.645	6.126 ± 1.676
$\Gamma 0.25$	0.613 ± 0.157	5.566 ± 3.186	10.34 ± 2.487
All	0.831 ± 0.170	5.318 ± 2.357	7.350 ± 2.732

Table 4.4: Median results for PIZA-simulation comparison with filled mask.

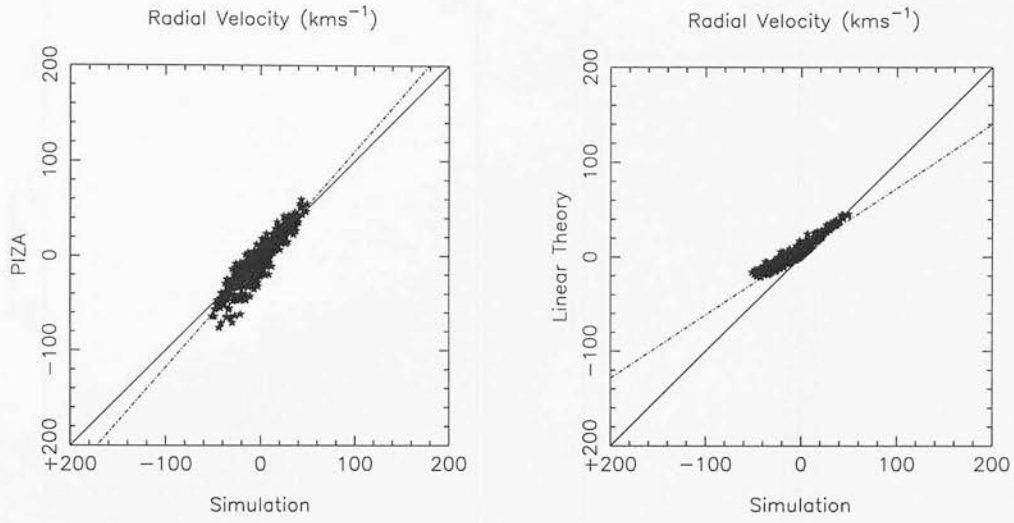

Figure 4.12: Comparison of MASSPIZA and linear theory reconstructions for simulation $\Lambda 0.7/1$ run 1 with filled mask. The dotted line indicates the least-squares fit.

4.6.1 Mass ratios after MASSPIZA has been applied

Once MASSPIZA has been carried out, the mass ratio R_m for each galaxy may again be calculated. This may be done in order to test whether the mass ratios have indeed been improved by reassigning particles. Figure 4.13 shows histograms of the mass ratios for galaxies in a PSCz simulation both before and after MASSPIZA has been applied. Clearly the distribution of mass ratios becomes thinner and more peaked about the value $R_m = 1$ after MASSPIZA has been applied, which is the aim of MASSPIZA.

4.6.2 The reconstructed dipole

Figure 4.14 shows how the Local Group trajectory and the dipole misalignment angle change with mass iteration. The values for both the trajectory and angle at a mass iteration value of 0 are those found by PIZA. For this case, the dipole remains constant after mass iteration 4. The general trend is for both the trajectory and the misalignment

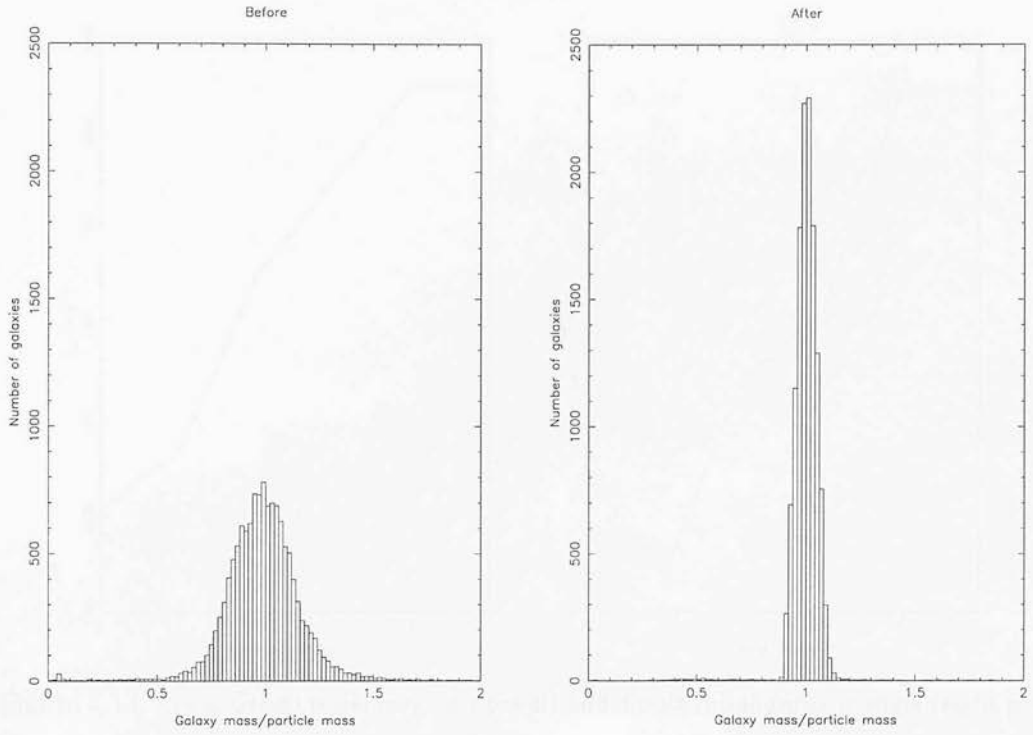

Figure 4.13: Histograms of mass ratios of galaxies in a PSCz simulation before (left hand panel) and after (right hand panel) MASSPIZA has been applied.

angle to increase with mass iteration. The slight decrease in Δ_{CMB} after the first mass iteration is not a general feature of MASSPIZA, and is simply due to the random nature of MASSPIZA.

4.6.3 Reconstructed velocity field

The reconstructed velocity field for one of the simulations using MASSPIZA is shown in Figure 4.15. For comparison, the PIZA velocity field for the same simulation is shown in Figure 4.16. The features in the velocity field after MASSPIZA are in general the same as in the PIZA velocity field. For example, the flow that converges on (SGX, SGY)=(70,-100), and the flow onto a wall that extends from (SGX, SGY)=(20,0) to (SGX, SGY)=(100,-40) are virtually identical in both velocity fields. Generally it is the magnitudes of the velocities that have changed the most. This is most noticeable in the flow towards (SGX, SGY)=(0,110) and the flow towards the wall at (SGX, SGY)=(20,0). The trajectory of the Local Group, as shown by the red arrow, has

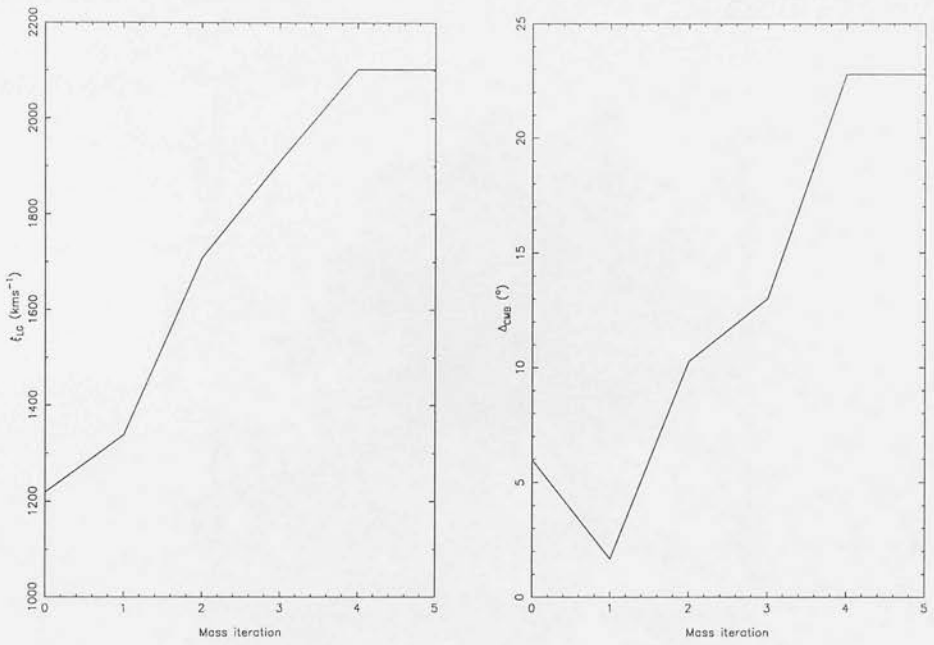

Figure 4.14: Local Group trajectory (left panel) and dipole misalignment angle (right panel) as a function of mass iteration. Note that after mass iteration 4, MASSPIZA has converged.

changed considerably, from a magnitude of $1246 kms^{-1}$ for PIZA and a magnitude of $2102 kms^{-1}$ for MASSPIZA.

4.7 Discussion

In this Chapter I have discussed MASSPIZA, a generalized PIZA for application to realistic redshift surveys, which takes account of the selection function. The constraint of equal particle to galaxy ratios for all galaxies is removed, and particles are assigned to galaxies such that the mass of each galaxy is equal to the total mass of its particles. To avoid the problem of the rocket effect, galaxy masses are found using the inverse selection function at their real space positions.

The method works as follows: after PIZA has been applied to a survey, the galaxy and particle masses are evaluated and those galaxies with too many and too few particles are found. Particles are then reassigned from galaxies with too many to those with too few. Once particles have been reassigned, S is again minimized. This process is

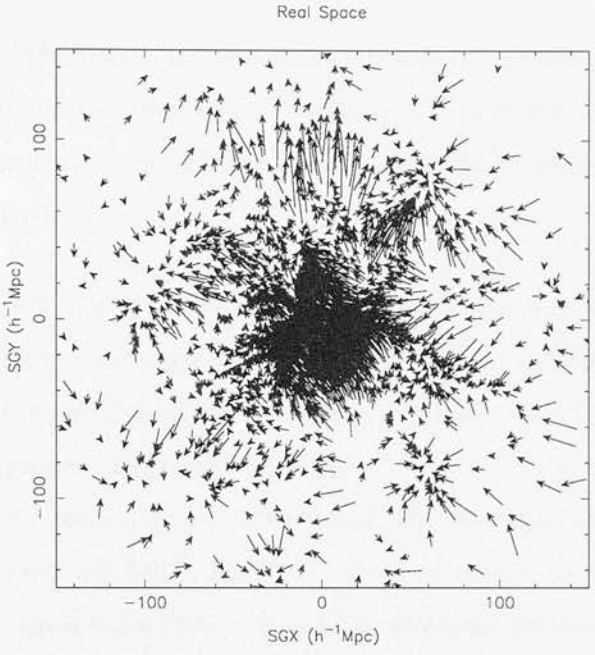

Figure 4.15: MASSPIZA reconstructed velocity field out to $R = 150h^{-1}Mpc$ for a PSCz simulation PIZA results. Arrows indicate magnitude of velocities, arrow heads are at galaxy real space positions. The red arrow shows the velocity of the Local Group galaxy.

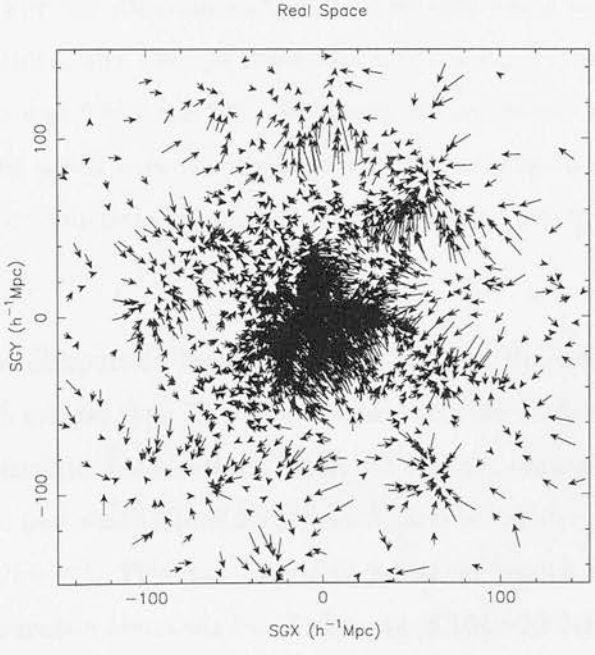

Figure 4.16: PIZA reconstructed velocity field out to $R = 150h^{-1}Mpc$ for PSCz simulation.

repeated until as many galaxies as possible have mass convergence.

It was found that MASSPIZA achieves mass convergence for around 95% of the galaxies within about 50,000 mass iterations. The value of S increases each time particles are reassigned, as long trajectories are introduced, but this increase is soon removed once S is again minimized.

Unfortunately it is found that the MASSPIZA method is unstable, with MASSPIZA runs on the same input converging to very different solutions. The trajectories of the Local Group and other galaxies increase to values generally much larger than those found by PIZA. The dipole misalignment angle also increases. Since the magnitude of the dipole increases, the reconstructed β decreases. For the $\Lambda 0.7$ simulations, the average reconstructed β is 0.258 ± 0.025. For the $\Gamma 0.25$ simulations, the average reconstructed β is 0.861 ± 0.391. Over the 8 PSCz simulations, the average dipole misalignment angle has an average of $22 \pm 7°$.

Since the velocities of all the galaxies are overestimated by MASSPIZA, it was found that the gradient of the slope of the comparison between MASSPIZA and simulation radial peculiar velocities was larger than that found with PIZA, and was occasionally greater than 1. For the $\Lambda 0.7$ simulations the average slope was 0.845 ± 0.143. For the $\Gamma 0.25$ simulations, the average slope was 0.613 ± 0.157. Over all 8 simulations, the average slope was 0.831 ± 0.170. This may be compared with the linear theory reconstructions for which over the 8 simulations the average slope was 0.807 ± 0.201, and the PIZA reconstructions for which the average slope was 0.744 ± 0.083 over the 8 simulations.

The scatter in the comparison between MASSPIZA and the simulations was found to generally be much greater than for PIZA, which is another indication that MASSPIZA is not a good reconstruction method. Over all the simulations, the average scatter about the best fit line was $5.318 \pm 2.357 kms^{-1}$, and the scatter about the $x = y$ line was $7.350 \pm 2.732 kms^{-1}$. This may be compared to the results from linear theory, for which the average scatter about the best fit line was $5.104 \pm 2.974 kms^{-1}$ and the average scatter about the $x = y$ line was $7.322 \pm 6.299 kms^{-1}$, and the PIZA results over all the

simulations for which the average scatter about the best fit line was $5.802 \pm 1.835 kms^{-1}$ and the average scatter about the $x = y$ line was $7.998 \pm 2.204 kms^{-1}$. So not only does MASSPIZA overestimate the magnitudes of the velocities as a whole, it is also very inaccurate compared with both linear theory and generalized PIZA.

There are a few reasons as to why MASSPIZA does not work well and overestimates the peculiar velocities of galaxies. The running away of the dipole and other galaxy velocities may be due to the rocket effect, as described above in Section 4.4. This may also be due to a mismatch between the sphere containing the galaxies and the sphere containing the PIZA particles. Both galaxy and particle distributions are picked in a sphere of radius R. However, the galaxies are picked according to their redshift space positions in the Local Group rest frame. When the galaxy positions are deprojected into real space, the sphere containing these positions, which are mapped to the particles' positions, may not coincide with the sphere of particles. If this is the case, it would lead to long trajectories where galaxies at the edge of the galaxy sphere are mapped to particles at the edge of the particle sphere - see Figure 4.17. As the dipole grows with mass iteration, the mismatch between the two spheres increases and the long trajectories also increase. A possible way around this would be to pick the galaxies and particles in coincident spheres, but to do this requires knowledge of the dipole - one of the things which is to be reconstructed from the survey. For this reason, I have not used this method. Another solution to this problem would be to carry out PIZA on a volume out to a much larger volume than the $R = 300h^{-1}Mpc$ I have used here. Unfortunately this is not an option with either the simulations or the PSCz survey.

Clearly MASSPIZA is not a successful reconstruction method. Whilst MASSPIZA works well at achieving mass convergence, i.e. galaxy mass equal to particle mass, for the majority of galaxies, it does this at the expense of the accuracy of the reconstruction. Therefore it is obvious that MASSPIZA does not overcome the problems of the selection function very well, and either the method needs more development or an entirely new method is needed.

Since MASSPIZA is not a successful reconstruction method, I have chosen not to use it for reconstructing the displacement and velocity fields from the PSCz survey.

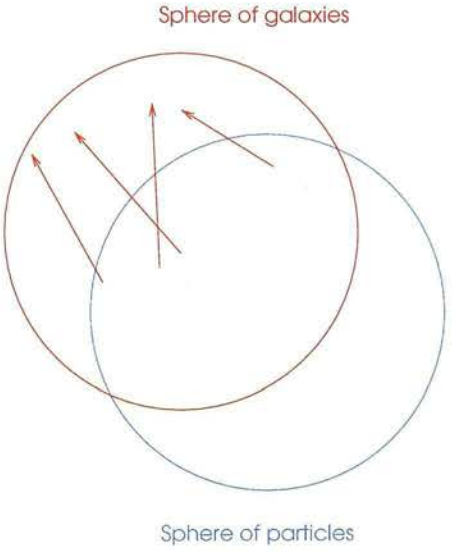

Figure 4.17: Misalignment between particle and galaxy spheres that causes trajectory runaway.

Chapter 5

Application of PIZA to the PSCz survey

In this Chapter I will discuss the reconstruction of the PSCz survey using the new generalized PIZA method I have described in Chapter 3.

In Section 5.1 I will describe the PSCz survey in some detail, and in Section 5.1.1 I discuss the selection function of the PSCz survey. Section 5.2 describes some of the other reconstructions which have been carried out on PSCz, and the results from these reconstructions.

In Section 5.3 I discuss my application of my generalized PIZA method to the PSCz survey. Section 5.3.1 describes the method used to interpolate the galaxy density field over the Galactic Plane, which I have used to fill the mask with galaxies when reconstructing PSCz.

In Section 5.3.2 I present the results of PIZA applied to PSCz with the mask empty. In Section 5.3.3 I present the results of PIZA applied to PSCz with the mask filled with interpolated galaxies. In Section 5.3.5 I present the reconstructed PSCz velocity field, bulk flows and dipole. Section 5.3.6 discusses the comparison between the PIZA reconstructed PSCz peculiar velocity field and the SFI velocity field. These results have

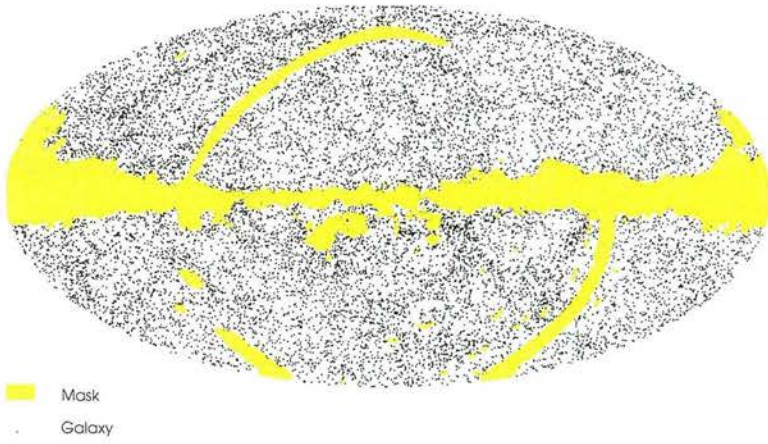

Figure 5.1: Aitoff projection of PSCz galaxies in galactic coordinates showing the sky coverage of the survey. The shaded region is the PSCz mask, the horizontal strip is the Galactic Plane.

been presented in Valentine, Saunders and Taylor (2000) and Saunders *et al.* (2000).

Section 5.4 discusses the results of the reconstruction.

5.1 Point Source Catalogue Redshift Survey

The Point Source Catalogue Redshift survey (PSCz) is a redshift survey of 15,000 *IRAS* galaxies uniformly covering 84% of the sky and flux limited to 0.6 Jy at $60\mu m$. The regions of the sky not covered by the survey are the Galactic Plane, where identification of sources is confusion limited, the Magellanic Clouds, and a strip of the sky that *IRAS* did not survey. The sky coverage of PSCz is shown in Figure 5.1, which shows the survey in Aitoff projection in galactic coordinates. The coloured regions make up the PSCz mask, which is discussed further below. The horizontal stripe is the Galactic Plane.

The main purposes of the PSCz survey were to understand the origin of the local veloc-

ity field; to test whether light traces mass on large scales; to test whether the statistics of the galaxy distribution are compatible with structure formation via inflation and gravitational instability. The specific targets for PSCz were to maximize sky coverage in order to predict the gravity field, and to obtain the best possible completeness and flux uniformity within well defined area and redshift ranges for statistical studies of the *IRAS* galaxy population and its distribution.

The PSCz survey is based on the QMW IRAS Galaxy Catalogue (QIGC; Rowan-Robinson *et al.* 1991). The QIGC is itself based on the IRAS Point Source Catalog (Beichman *et al.* 1988), and was supplemented by sources from the Faint Source Survey (Moshir *et al.* 1989). Sources were included in the sample on the basis of good or moderate quality fluxes greater than $0.6Jy$ at $60\mu m$. This wavelength was chosen as it is the wavelength where contamination from stars and cirrus is minimized. In the Galactic Plane there is the possibility of confusing the extra-galactic sources being searched for with galactic sources, and far infrared colour and identification constraints were used to discriminate against galactic sources such as stars, cirrus and planetary nebulae.

The PSCz survey was started in 1992, when approximately 2/3 of the galaxies had known or unpublished redshifts. This made the survey practicable over a reasonable amount of time. The unknown redshifts were taken using the INT, AAT and CTIO $1.5m$ telescopes.

The PSCz survey is incomplete at low galactic latitudes as dust extinction from the Milky Way makes it difficult for redshifts of galaxies behind the Milky Way to be obtained, and as the *IRAS* data is progressively more confused and less complete at lower latitudes. To take account of this in analyses, there is a PSCz mask which excludes from analysis the unsurveyed sky. The mask is based on the 41167 $1° \times 1°$ lune bins into which the sky was divided for the *IRAS* surveys (Beichman *et al.* 1988). The Behind The Plane survey (Saunders *et al.* 1999a) extends the sky coverage of the PSCz survey into the Galactic Plane.

The galaxies in the PSCz are typical *IRAS* galaxies, spiral galaxies with high infrared

emission due to normal star formation. Early type galaxies, elliptical and S0 galaxies, are not represented in the PSCz survey as they have little dust or star formation and were not detected by *IRAS*.

There is incompleteness in the catalogue for a number of reasons. There is incompleteness in the PSC where sources with a flux greater than $0.6Jy$ failed to get into the catalogue. Incompleteness is introduced at low latitudes, as the PSC is confusion limited in the galactic plane. The major sources of unreliability in the PSCz are incorrect redshifts of galaxies and incorrect identification of sources with galaxies with similar angular positions.

Figure 5.2 shows two-dimensional projections of the x-y, y-z and x-z planes, in galactic coordinates, of the PSCz galaxies. The Local Group is at the origin. The empty regions make up the PSCz mask, and the tapering regions about $z = 0$ are the Galactic Plane. The decrease of galaxy number density with distance is clearly seen in these figures.

5.1.1 The PSCz Selection Function

In the PSCz survey, as in all flux limited catalogues, the number density of sample objects is a decreasing function of redshift. This is quantified with the selection function, $\phi(r)$, the expected number of galaxies seen above the flux limit at distance r in the absence of clustering.

The PSCz selection function is given by (Mann, Saunders and Taylor 1996)

$$\phi = \frac{\phi_* 10^{(1-\alpha)\Delta}}{(1 + 10^{\gamma\Delta})^{\frac{\beta}{\gamma}}} \tag{5.1}$$

where

$$\Delta = \log_{10}(d/d_*) \tag{5.2}$$

The parameters describe various properties of the selection function: ϕ_* the amplitude, α the nearby slope, d_* the break position, γ the breadth and β the distant slope. In this work I have used parameters for a Euclidean Universe, listed in Table 5.1.

Figure 5.3 shows the PSCz selection function.

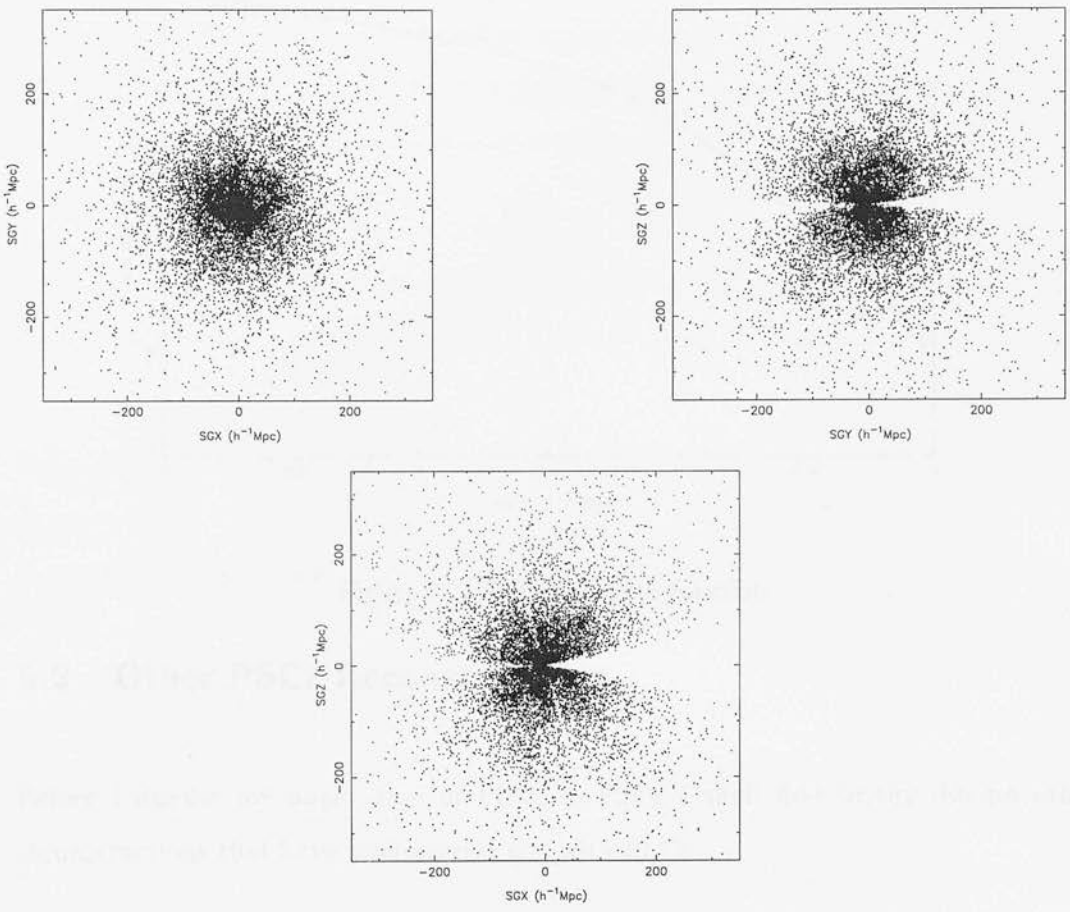

Figure 5.2: 2-d projections of PSCz galaxy distribution in galactic coordinates in x-y, y-z and x-z planes. The empty regions indicate the PSCz mask.

parameter	value
α	1.88654
β	4.38595
γ	1.54554
d_*	1.95113
ϕ_*	0.0067941

Table 5.1: PSCz selection function parameters for a Euclidean Universe.

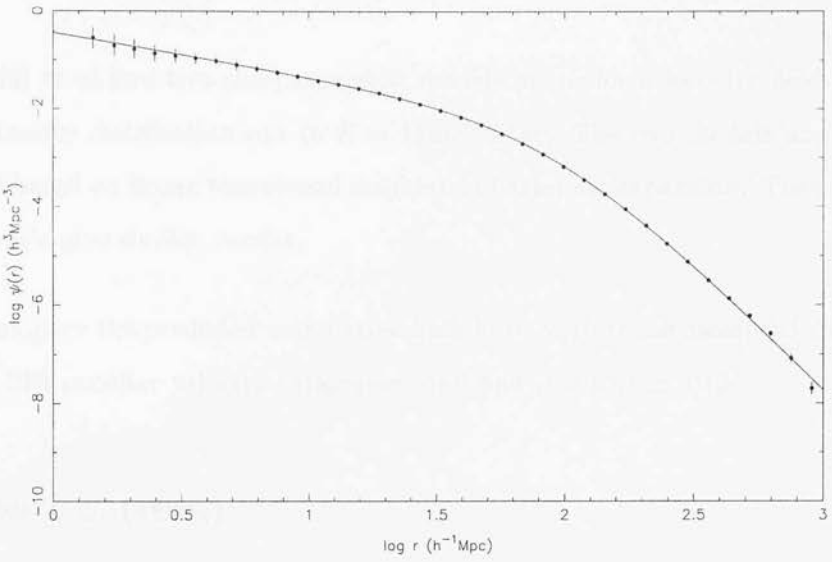

Figure 5.3: PSCz selection function.

5.2 Other PSCz Reconstructions

Before I discuss my application of PIZA to PSCz I shall first briefly discuss other reconstructions that have been carried out with PSCz.

5.2.1 Velocity Field Reconstructions

Sharpe *et al.* (2000)

Sharpe *et al.* use the Least Action principle to reconstruct the peculiar velocities of PSCz galaxies within $cz = 2000 kms^{-1}$. They use linear theory to account for tidal effects out to $cz = 15000 kms^{-1}$, and iterate the galaxy positions to account for redshift distortions. The method provides reliable peculiar velocities for galaxies down to $cz < 500 kms^{-1}$.

They compare these peculiar velocities with the observed velocities of 12 galaxies with Cepheid distances. Under the assumption of no biasing, they find that $\beta \leq 0.75$ at 90% confidence. They also use the peculiar velocities to predict the Hubble constant within the local volume, and find that $H_0 = 65$–$75 kms^{-1} Mpc^{-1}$ at 90% confidence.

Branchini *et al.* (1999)

Branchini *et al.* find two non-parametric models of the local velocity field based on the PSCz density distribution out to $R = 150h^{-1}Mpc$. The two models are: an iterative method based on linear theory and a spherical harmonic expansion. They find that the two models give similar results.

They compare the predicted cumulative bulk flows with those measured from the Mark III and SFI peculiar velocity catalogues, and find $\beta = 0.76 \pm 0.13$.

Schmoldt *et al.* (1999a)

Schmoldt *et al.* reconstruct the velocity and density fields from PSCz using a Fourier Bessel method. They find that their reconstructed velocity field agrees with that of Branchini *et al.* (1999).

Comparing the reconstructed Local group velocity with the CMB dipole, they find that $\beta = 0.7 \pm 0.5$. Performing an anisotropy test on the velocity field, they find that they can exclude $\beta = 1$ CDM models normalized to the current cluster abundance with 90% confidence.

5.2.2 Dipole Reconstructions

Rowan-Robinson *et al.* (2000)

Rowan-Robinson *et al.* use the PSCz to analyse the dipole out to a distance of $R = 300h^{-1}Mpc$. They find the dipole to have converged within $R = 200h^{-1}Mpc$, and to 13° away from the CMB dipole. Their reconstructed dipole gives $\beta = 0.75^{+0.11}_{-0.08}$. If b=1, this leads to $\Omega_0 = 0.43$–1.02.

Schmoldt *et al.* **(1999b)**

Schmoldt *et al.* calculate the acceleration on the Local Group using PSCz galaxies. They put the galaxies at their real space positions using a non-parametric model for the velocity field which uses linear theory and linear biasing.

They find the dipole to be 15° away from the CMB dipole. They carry out a maximum likelihood analysis on the cumulative dipole out to $R = 150h^{-1}Mpc$, and find $\beta = 0.70^{+0.5}_{-0.2}$.

5.3 PIZA applied to PSCz

In this Section I describe the application of PIZA to the PSCz survey, and present the results of the reconstruction. The method applied is the generalized PIZA method presented in Chapter 3. In these reconstructions I have again used a particle to galaxy ratio of $\nu = 10$, and have carried out PIZA on the PSCz out to a radius of $R = 300h^{-1}Mpc$. In this work the input value of β was 0.5. I have reconstructed PSCz both with and without the Galactic Plane filled with galaxies. The method used to fill the Galactic Plane is described below in Section 5.3.1.

In Section 5.3.2 I present the results of the reconstruction of PSCz with the mask empty. Reconstructions were carried out using 6 sets of initial conditions. The dipole and the inferred β are presented.

In Section 5.3.3 the results of the reconstruction of PSCz with the mask filled are presented. Again reconstructions were carried out using 6 sets of initial conditions. The dipole and inferred β are presented.

The reconstructed PSCz velocity field, dipole and bulk flows are presented. These were reconstructed with the mask filled. The reconstructed peculiar velocity field is compared with the SFI peculiar velocities. The reconstructed dipole is used to infer a value for β.

Run	l (°)	b (°)	ξ_{LG} (kms^{-1})	θ_{CMB} (°)	Inferred β
1	230	27	1433	33	0.438
2	233	20	1602	33	0.392
3	229	14	1745	38	0.359
4	229	17	1660	37	0.378
5	230	20	1709	35	0.367
6	232	23	2135	33	0.294

Table 5.2: Reconstructed dipole directions and magnitudes, and reconstructed β for PSCz with empty mask.

5.3.1 Filling the Galactic Plane

As I have mentioned in previous Chapters, the lack of galaxies in the Galactic Plane can cause problems when reconstructing the velocity field from a redshift survey. Of course, this is not as much of a problem when using PIZA to reconstruct the velocity field, as the Galactic Plane may simply be left empty of PIZA particles. However, it is possible to fill the Galactic Plane with galaxies using a variety of methods.

To fill the Galactic Plane when using PSCz, I have used interpolated galaxies produced with a new Fourier Interpolation method (Saunders and Ballinger 2000). The method allows optimal nonlinear interpolation across the plane.

5.3.2 PSCz results with empty mask

The overall results are as follows:

The displacement of the Local Group has a mean of $1714 \pm 70 kms^{-1}$ and a median of $1685 \pm 143 kms^{-1}$.

The misalignment angle has a mean of $35° \pm 2$ and a median of $34° \pm 4$.

The reconstructed β has a mean of 0.371 ± 0.035 and a median of 0.373 ± 0.033 where

Run	l (°)	b (°)	ξ_{LG} (kms^{-1})	θ_{CMB} (°)	Inferred β
1	254	34	1223	14	0.513
2	252	35	1255	16	0.500
3	253	43	1442	20	0.435
4	272	46	1206	19	0.520
5	270	41	1534	15	0.409
6	258	36	1276	12	0.491

Table 5.3: Reconstructed dipole directions and magnitudes, and reconstructed β for PSCz with filled mask.

the errors are due to different initial conditions. Note that this result does not take the underestimation of β by PIZA into account.

5.3.3 PSCz results with filled mask

The overall results are:

The displacement of the Local Group has a mean of $1323 \pm 134 kms^{-1}$ and a median of $1266 \pm 110 kms^{-1}$.

The dipole misalignment angle has a mean of $16° \pm 3$ and a median of $16° \pm 2$.

The reconstructed β has a mean of 0.478 ± 0.045 and a median of 0.496 ± 0.039 where the errors are due to different initial conditions. Again, this result does not take the underestimation of β into account.

5.3.4 Bulk velocities and dipole

The PSCz bulk velocities and dipole out to $R = 150h^{-1}Mpc$ are shown in Figure 5.4. The bulk velocities were found by finding the average velocities in successively larger spheres, and the dipole was found by subtracting the bulk velocities from the bulk

velocity at the origin.

The left hand panel of Figure 5.4 shows the bulk velocities. The bulk velocity at the origin is the velocity of the Local Group, in other words the dipole. The bulk velocities decrease rapidly from this value until a radius of $R \simeq 50h^{-1}Mpc$. After this radius, the bulk velocities decrease more slowly. It may be expected that the bulk velocity at the edge of the survey is zero. From the Figure, it may be seen that this is not the case at $R = 150h^{-1}Mpc$. This may indicate that the survey volume as a whole has a small bulk velocity of the order of $\sim 25kms^{-1}$.

The right hand panel of Figure 5.4 shows the cumulative dipole for the PSCz survey. It can be seen that all the components of the dipole rise fairly rapidly from zero at the origin, with the total rms dipole increasing to $\sim 600kms^{-1}$ at a radius of $R \simeq 50h^{-1}Mpc$. The contribution to the dipole at distances greater than this distance is seen to be negligible.

An average dipole direction of (l,b)=(264.4°,41.7°) was found. This may be compared with the reconstructed dipole of Schmoldt *et al.* (1999b), which has a direction of (l,b)=(260±10°,34±10°), and that of Rowan-Robinson *et al.* (1999) which has a direction of (l,b)=(250°,33°). The reconstructed dipole leads to $\beta = 0.51 \pm 0.14$. This error has 3 sources: random error due to different initial conditions; misalignment between the reconstructed and CMB dipoles; cosmic variance and shot noise on the reconstructed dipole (Taylor and Valentine 1999; Chapter 2).

5.3.5 Reconstructed velocity field

Figure 5.5 shows the reconstructed PSCz velocity field out to $R = 150h^{-1}Mpc$ in a slice $20h^{-1}Mpc$ thick centred on the Supergalactic Plane. The arrow heads are at the galaxy real space positions, and the lengths of the arrows show the velocity magnitudes. The red arrow indicates the trajectory of the Local Group galaxy. Figure 5.6 shows the reconstructed velocity field out to $R = 50h^{-1}Mpc$.

Generally the velocity field at the edge of the volume is quiet, apart from flow towards

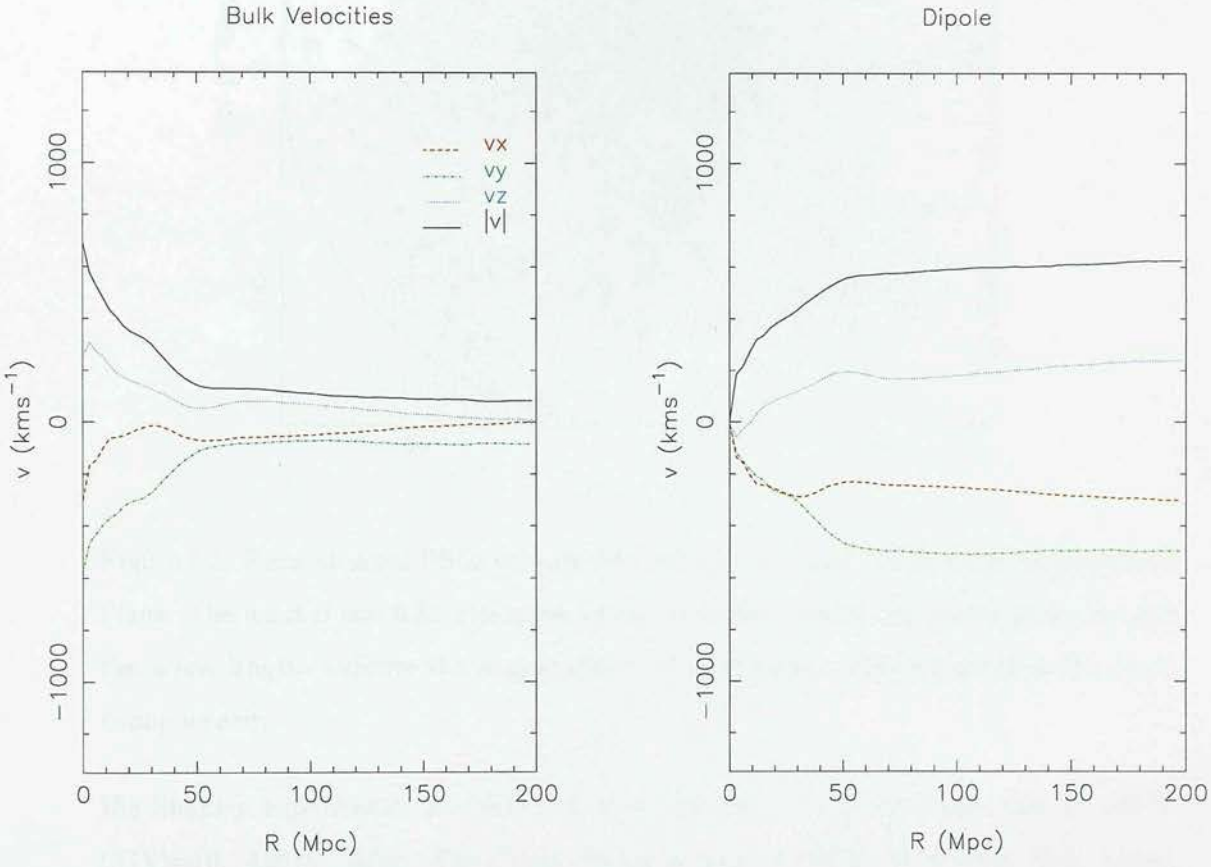

Figure 5.4: Reconstructed PSCz bulk flows and dipole out to $R = 150h^{-1}Mpc$. The input β was 0.5.

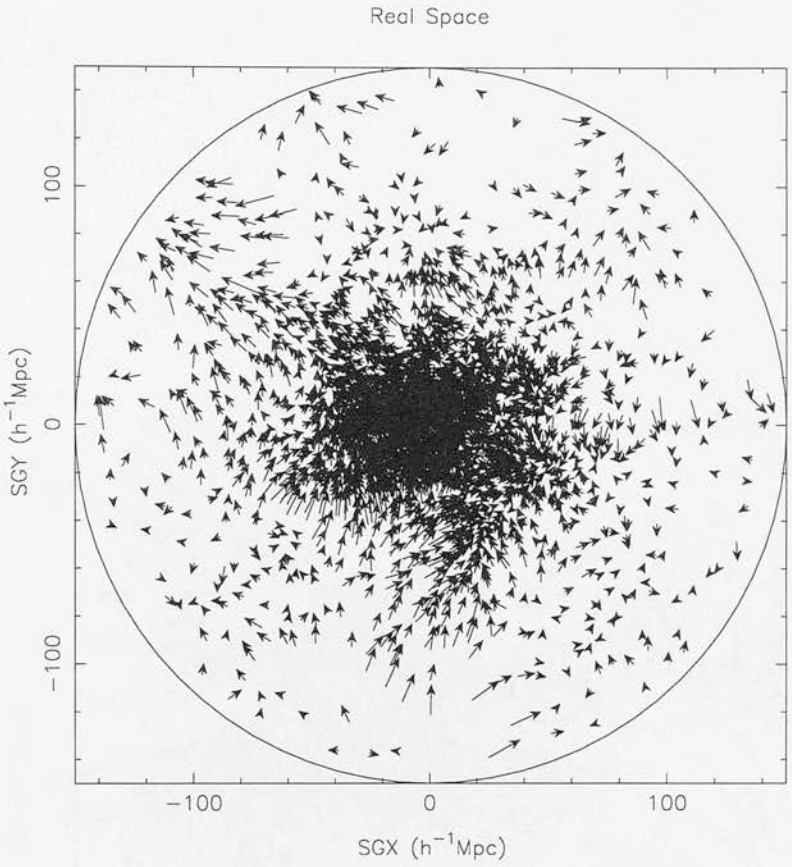

Figure 5.5: Reconstructed PSCz velocity field out to $R = 150h^{-1}Mpc$ in the Supergalactic Plane. The input β was 0.5. The arrow heads are at the present day galaxy positions, and the arrow lengths indicate the magnitudes of the velocities. The red arrow is the Local Group velocity.

the Shapley supercluster at (SGX, SGY)=(120, 90)$h^{-1}Mpc$ and the void at (SGX, SGY)=(0, -120)$h^{-1}Mpc$. The Coma cluster is seen at (SGX, SGY)=(0, 70)$h^{-1}Mpc$. The Cetus wall extends northwards from (SGX, SGY)=(0, -100)$h^{-1}Mpc$ towards Perseus-Pisces at (SGX, SGY)=(50, -20)$h^{-1}Mpc$. Virgo is seen at (SGX, SGY)=(0, 10)$h^{-1}Mpc$. The Great Attractor is at (SGX,SGY)=(-40, 20)$h^{-1}Mpc$, and little evidence of backfall on to it on the opposite side to the Great Attractor from the Local Group is seen.

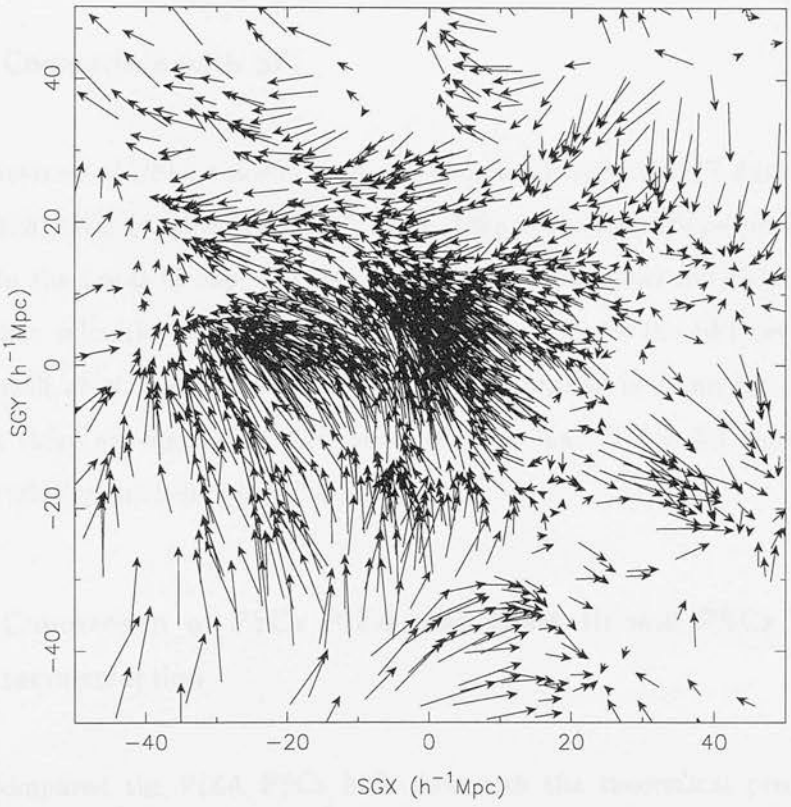

Figure 5.6: Reconstructed PSCz velocity field out to $R = 50h^{-1}Mpc$ in the Supergalactic Plane. The input β was 0.5.

Shell	V_{SFI}	(l,b)$_{SFI}$	V_{PIZA}	(l,b)$_{PIZA}$
0 - 2000	270±80	(245,49)±19	372	(228,45)
1500 - 3500	410±69	(255,21)±12	430	(254,56)
2500 - 4500	620±76	(255,15)±11	485	(271,50)
3500 - 5500	585±92	(265,19)±13	550	(281,39)
4500 - 6500	544±98	(270,16)±15	503	(279,34)

Table 5.4: Comparison between SFI and reconstructed PSCz peculiar velocities with respect to shells of galaxies. The PIZA PSCz reconstruction had $\beta = 0.5$.

5.3.6 Comparison with SFI

The reconstructed PSCz velocity field was compared with the SFI data set of peculiar velocities of spiral galaxies (Giovanelli *et al.* 1998). The average peculiar velocity, with respect to the Local Group, of galaxies in redshift slices was calculated. This was to get peculiar velocities as closely as possible comparable to the SFI peculiar velocities of Giovanelli *et al.*. Reasonable agreement in amplitude is found for $\beta = 0.55 \pm 0.1$, although there are significant differences in direction. Table 5.4 shows the average peculiar velocity in shells for PIZA and SFI.

5.3.7 Comparison of PSCz PIZA with Mark III and PSCz linear theory reconstruction

I have compared the PIZA PSCz bulk flow with the theoretical prediction for the bulk flow, the bulk flow of the Mark III catalogue (Willick *et al.* 1997) and the linear theory reconstructed bulk flow (Branchini *et al.* 1999). The 3 bulk flows are shown in Figure 5.7. The Mark III bulk flow was taken from Dekel *et al.* (1999). The PIZA bulk flow was produced using $\beta = 0.5$. The error bars for the PIZA bulk flow were estimated using the cosmic variance and shot noise expressions derived in Chapter 2. The theoretical bulk flow was calculated using

$$\langle |v_b(R)|^2 \rangle = \frac{\beta^2}{2\pi^2} \int P(k) W(kR)^2 dk \tag{5.3}$$

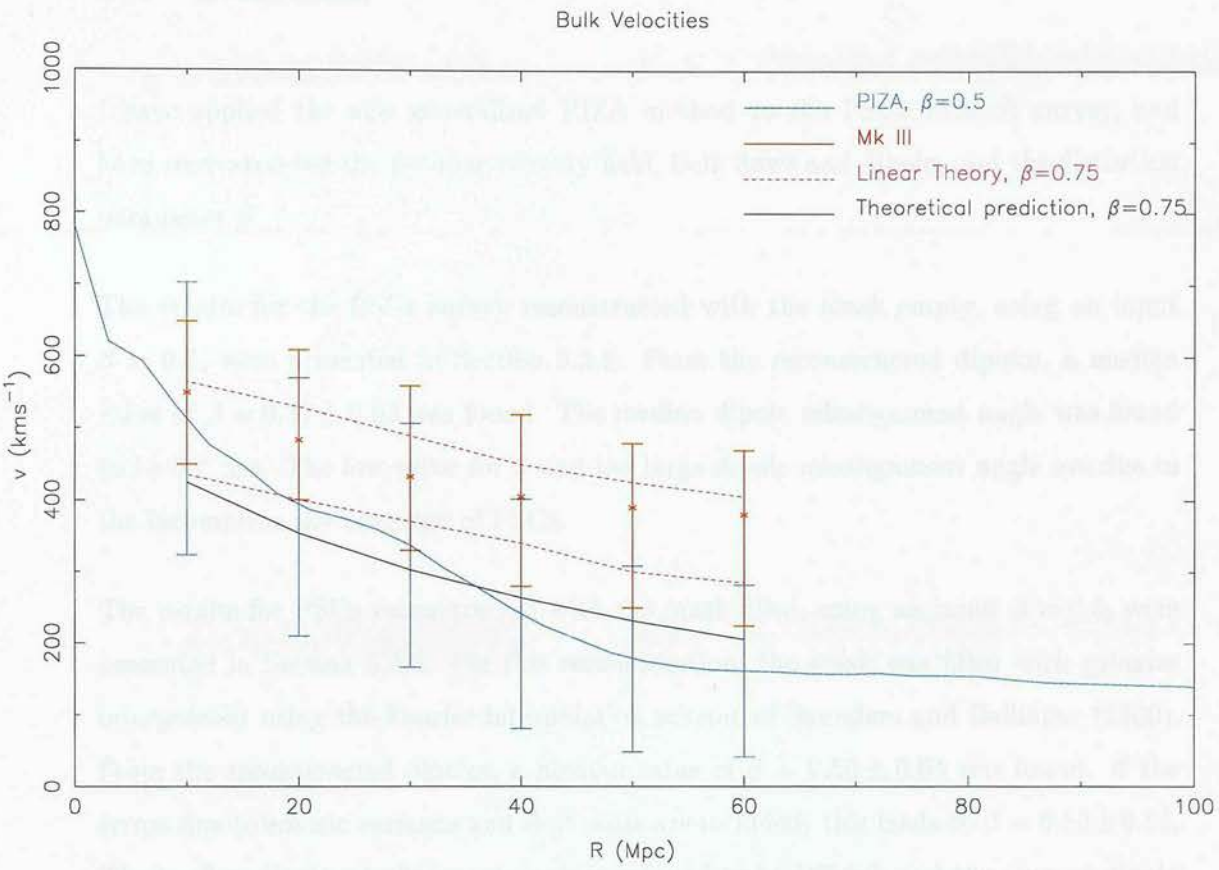

Figure 5.7: Comparison between bulk flows of PSCz using PIZA, PSCz using linear theory (Branchini *et al.* 1999), Mark III (Dekel *et al.* 1999), and theory.

(Dekel 1994). The power spectrum of Peacock and Dodds (1994), Equation(2.85), was assumed, along with $\beta = 0.75$, and a spherical top hat window function. It was found in Branchini *et al.* (1999) from the comparison between the linear theory PSCz bulk flow and the Mark III bulk flow that $\beta = 0.55 \pm 0.25$.

I have found that, within error bars, the PIZA bulk flow is roughly consistent with the other 3 bulk flows. The agreement is far better at radii less than $R \sim 50h^{-1}Mpc$. This may be due to the fact that generally PIZA underestimates galaxy peculiar velocities.

A value for β may be found by requiring that the amplitude of the reconstructed and directly measured bulk flows are the same. Thus comparing the bulk flows, I have found that $\beta = 0.5 \pm 0.3$. This is consistent with the results of Tadros *et al.* (1999) based on the measurement of the degree of redshift space distortion in the PSCz.

5.4 Discussion

I have applied the new generalized PIZA method to the PSCz redshift survey, and have reconstructed the peculiar velocity field, bulk flows and dipole, and the distortion parameter β.

The results for the PSCz survey reconstructed with the mask empty, using an input $\beta = 0.5$, were presented in Section 5.3.2. From the reconstructed dipoles, a median value of $\beta = 0.37 \pm 0.03$ was found. The median dipole misalignment angle was found to be $34° \pm 4$. The low value for β and the large dipole misalignment angle are due to the incomplete sky coverage of PSCz.

The results for PSCz reconstructed with the mask filled, using an input $\beta = 0.5$, were presented in Section 5.3.3. For this reconstruction, the mask was filled with galaxies interpolated using the Fourier interpolation scheme of Saunders and Ballinger (2000). From the reconstructed dipoles, a median value of $\beta = 0.50 \pm 0.04$ was found. If the errors due to cosmic variance and shot noise are included, this leads to $\beta = 0.50 \pm 0.14$. The median dipole misalignment angle was found to be $16° \pm 2$, and the average dipole direction was (l,b)=(264.4°,41.7°). This may be compared with the reconstructed dipole of Schmoldt *et al.* (1999b), which has a direction of (l,b)=(260±10°,34±10°), and that of Rowan-Robinson *et al.* (1999) which has a direction of (l,b)=(250°,33°).

The reconstructed PSCz velocity field was presented in Figure 5.5, and was discussed in Section 5.3.5. The PSCz bulk flows and dipole were presented in Figure 5.4 and discussed in Section 5.3.4.

The reconstructed PSCz peculiar velocity field was compared with both the SFI and Mark III peculiar velocity surveys. The results from these comparisons were presented in Sections 5.3.6 and 5.3.7. From the comparison with SFI, it was concluded that $\beta = 0.55 \pm 0.1$. From the comparison with Mark III it was concluded that $\beta = 0.5 \pm 0.3$.

The values of β that I have found here are consistent with those found by Nusser *et al.* (2000) and Hamilton, Tegmark and Padmanabhan (2000). Nusser *et al.* compare the reconstructed PSCz peculiar velocity field (from Branchini *et al.* 1999) with the ENEAR

$D_n - \sigma$ catalogue (da Costa *et al.* 2000), and find $\beta = 0.5 \pm 0.1$. Hamilton *et al.* carry out a linear redshift distortion analysis of the PSCz, and find that $\beta = 0.41^{+0.13}_{-0.12}$.

Chapter 6

Conclusions

In this Chapter I will discuss the conclusions that may be drawn from the work in this thesis, and discuss further work which may be done in the future based on that presented here.

6.1 Errors on the velocity field

In Chapter 2, expressions for the cosmic variance and shot noise errors on the reconstructed velocity field were presented. The radial and transverse components of the velocity field in terms of the spherical harmonics were derived, and the correlation, cross-correlation and variance terms were found. The cosmic variance in the velocity field due to both internal and external structures was found, both in the CMB and Local Group rest frames, as a function of position in the survey. Figure 2.1 presents the cosmic variance on the velocity field due to external structures, as a function of position for a survey of radius $R = 100h^{-1}Mpc$, in both CMB and Local Group frames. It was found that working in the Local Group rest frame considerably reduces the error on the velocity field, by around $100kms^{-1}$ at any point in the survey volume.

Expressions for the uncertainty in the reconstructed velocity field due to shot noise were derived in both the CMB and Local Group rest frames. Figure 2.2 presents

the shot noise on the velocity field as a function of position for a survey of radius $R = 100h^{-1}Mpc$ in both CMB and Local Group frames. In the case of the shot noise errors, it was found that working in the Local Group rest frame does not have much effect on the errors on the reconstructed velocity field, apart from at distances less than $R = 30h^{-1}Mpc$, and then the reduction in the error is only small.

The combined error on the reconstructed dipole due to both cosmic variance from external sources and shot noise was found. Figure 2.3 presents the cosmic variance, shot noise, and total errors on the dipole, as a function of survey radius, up to a radius of $R = 300h^{-1}Mpc$. It was found that the total error on the dipole has a minimum at a radius of about $R = 150h^{-1}Mpc$, thereafter the error on the dipole becomes dominated by shot noise.

Errors will be introduced into the reconstructed velocity field by the incomplete sky coverage of the survey used. As I have discussed in Section 3.2.4, this may cause problems, and various methods have been employed to take account of this incomplete coverage. It would be possible to quantify the error introduced by the incomplete sky coverage in a similar way to that used in Chapter 2, but carrying out the angular integrals over the sky covered by the survey only.

6.2 Generalized PIZA

In Chapter 3, a generalized PIZA for application to realistic redshift surveys was presented. The problem of using redshifts in the Local Group frame was discussed, and an expression for the mean square particle displacement to be used when applying PIZA to a redshift survey was derived. The problems caused by incomplete sky coverage were discussed, and some solutions to those problems were suggested. To take account of the selection function at this stage, PIZA particles were assigned weights of the inverse of their selection function. Various problems which occurred whilst I was generalizing PIZA, and the solutions I developed for these problems, were discussed. The final version of the generalized PIZA was described.

The new generalized PIZA was applied to a set of PSCz simulations of two cosmologies. The reconstruction of the dipole and of the radial peculiar velocity field were tested. PIZA was tested with and without the Galactic Plane filled to test how this affected the accuracy of the reconstruction. PIZA was also tested on the simulations using different input values for β to see whether this affected the reconstruction of β. The PIZA reconstructions were also compared with linear theory reconstructions of the simulations to test whether PIZA is a more accurate reconstruction method than linear theory.

It was found that the reconstruction of the dipole is unaffected by the input value of β for sensible input values of β. This means that PIZA may be used to reconstruct the true value of β from the dipole of a redshift survey nearly independently of β. However, the reconstructed peculiar velocity field was found to be affected by the input β. This is likely to be due to the fact that in reconstructing the dipole only one trajectory is used, and in reconstructing the peculiar velocity field all the galaxy trajectories are used. A way around this problem of the peculiar velocities being reconstructed incorrectly is to to carry out PIZA iteratively, changing the input β, until it converges.

It was found that, as might be expected, the dipole misalignment angle was affected by the amount of sky coverage. The median misalignment angle over all 8 simulations was found to be $\theta_{CMB} = 17 \pm 8°$ with 84% sky coverage and $\theta_{CMB} = 15 \pm 9°$ for full-sky coverage. It was found that the reconstructed radial peculiar velocity field and the reconstructed β were unaffected by sky coverage. This is most likely because even with PSCz sky coverage 84% of the sky is covered. The amount of sky coverage does affect the accuracy of the reconstruction, the effect is likely to be more noticeable with less sky coverage.

With 84% sky coverage, it was found that, for the $\Lambda 0.7$ simulations the median reconstructed β was 0.419 ± 0.070 and for the $\Gamma 0.25$ simulations the median reconstructed β was 0.953 ± 0.270. With full sky coverage, for the $\Lambda 0.7$ simulations the median reconstructed β was 0.431 ± 0.052 and for the $\Gamma 0.25$ simulations the median reconstructed β was 0.841 ± 0.183. It was found that the value of β reconstructed was underestimated by between 10 to 20% that of the true β. This is possibly due to the effects of the

selection function, which are not taken into account in the generalized PIZA.

For the comparison between linear theory and simulation radial peculiar velocity fields, the median gradient of the slope of this comparison over all 8 simulations was 0.807 ± 0.201 and the median scatter about this slope was $5.104 \pm 2.974 kms^{-1}$. For PIZA with 84% sky coverage, the median gradient over the 8 simulations was 0.682 ± 0.184 and the median scatter about this slope was $5.461 \pm 1.702 kms^{-1}$, and for PIZA with full sky coverage the median gradient over the 8 simulations was 0.744 ± 0.083 and the scatter about this slope was $5.802 \pm 1.835 kms^{-1}$. Obviously for a perfect reconstruction, the gradient of the slope would be equal to 1.

Generally PIZA was found to be slightly worse than linear theory in reconstructing the radial peculiar velocity field. This may be due to the effects of the selection function, which are not explicitly taken into account in generalized PIZA - it was shown in CG97 that PIZA worked better than linear theory in reconstructing surveys without a selection function. It should be noted, however, that individual PIZA reconstructions may be much more accurate than linear theory, due to the randomness of PIZA.

The failure of generalized PIZA to be more accurate than linear theory may also be due in part to the inverse selection function weighting used as effective masses. A weighting that may work better is $1/\phi^{1/3}$, where ϕ is the selection function. The reasoning behind this choice of weighting is as follows. In PIZA, we want to minimize

$$S = \sum_i \xi_i^2 \sim N \bar{n}^{-2/3}$$

where the sum is over all galaxies, N is the total number of galaxies, and $\bar{n}$ is the mean number density of galaxies. However, with a sparsely sampled survey, we do not have all the galaxies and the quantity we actually minimize is

$$S' = \sum_i w_i \xi_i^2$$

where this time the sum is over the sparse galaxies in the survey, and w_i is some weight function. For a sparsely sampled survey, where the sampling factor is ϕ, the mean separation of galaxies is $(\bar{n}\phi)^{-1/3}$, and

$$S' \sim N_{sparse} (\bar{n}\phi)^{-2/3} w.$$

N_{sparse} is the total number of galaxies in the survey, and is equal to ϕN, where N is the total number of galaxies in the surveyed region. Hence,

$$S' \sim N\bar{n}^{-2/3} w \phi^{1/3}.$$

As the quantity we want to minimize is $S \sim N\bar{n}^{-2/3}$, we then take the weighting factor $w = \phi^{-1/3}$.

It has not been possible to use this new weight function in PIZA for inclusion in this thesis. However, preliminary results indicate that it works at least as well as the old ϕ^{-1} weighting, possibly better.

6.3 Generalized PIZA with a selection function

In Chapter 4, a version of PIZA which takes the selection function into account, MASSPIZA, was presented. This method assigns particles to galaxies such that the mass of each galaxy is as close as possible to the mass of its particles. This is done by removing the constraint that each galaxy has an equal number of particles. The method is run after the generalized PIZA has been applied to a survey, and attempts to improve on that reconstruction.

The problems encountered when generalizing PIZA for a selection function were discussed, and possible solutions to these problems were presented. The final MASSPIZA method was presented, and was tested on the PSCz simulations.

MASSPIZA was found to achieve mass equality by reassigning particles very well, with the majority of galaxies getting mass equality within 50,000 mass iterations. However, MASSPIZA was found to be unstable, with the dipole running away as more mass iterations were done. This may occur for a variety of reasons. The dipole may run away due to the rocket effect, or it may occur due to the mismatch between the spheres containing the particles and galaxies used in MASSPIZA. For these reasons, MASSPIZA was not used to reconstruct the PSCz survey.

It was shown that MASSPIZA does not overcome all the problems of the selection func-

tion. The particle reassignment works well, and it is possible that a working version of MASSPIZA, or any PIZA taking the selection function into account, would incorporate particle reassignment in some form. However, MASSPIZA as presented in this thesis is not a successful reconstruction method, and some work is needed before it can reliably be used.

6.4 Application to PSCz

In Chapter 5, the new generalized PIZA method was applied to the PSCz survey using an input $\beta = 0.5$, and the reconstructed velocity field, bulk flow and dipole were presented. The reconstruction was carried out on PSCz both with the mask regions empty and with the mask filled with interpolated galaxies. As would be expected, the reconstruction including the interpolated galaxies produces a dipole closer with the CMB dipole. The results I quote in the rest of this Section are from the reconstruction with interpolated galaxies filling the mask.

The reconstructed velocity field in the supergalactic plane was presented in Figures 5.5 and 5.6. The velocity field is reproduced well, with the flows around clusters and voids in the supergalactic plane, such as Coma, Perseus-Pisces and Virgo, being reconstructed. The velocity field at the edge of the volume is remarkably quiet, apart from flows onto the Shapley supercluster and out of a void in the southern hemisphere. There is little evidence for back flow onto the Great Attractor.

The reconstructed PSCz bulk flow and dipole were presented in Figure 5.4. The average reconstructed dipole direction was (l,b)=(264.4°,41.7°), and the average dipole misalignment angle was $16° \pm 2$. Comparing the reconstructed dipole with the CMB dipole, a value of $\beta = 0.5 \pm 0.14$ was found.

The PSCz reconstructed peculiar velocity field was compared with the SFI catalogue. The average peculiar velocity, with respect to the Local Group, in redshift slices was found, and compared with the SFI peculiar velocities. It was found that there were differences in the direction of the peculiar velocity, but the amplitudes agreed well for

$\beta = 0.55 \pm 0.1$.

The reconstructed bulk flow was compared with that of the Mark III catalogue and the linear theory PSCz reconstruction. It was found that the PSCz bulk flow was consistent with the other 2 bulk flows within the error bars, although there were some differences in amplitude. From this comparison, it was found that $\beta = 0.5 \pm 0.3$.

The results presented here are consistent with the values for β found by other authors using PSCz. For example, Tadros *et al.* (1999) found $\beta = 0.47 \pm 0.16$, Nusser *et al.* (2000) found $\beta = 0.5 \pm 0.1$, and Hamilton *et al.* (2000) found $\beta = 0.41^{+0.13}_{-0.12}$. The values of β presented here are also consistent, assuming no biasing, with current popular cosmological models with a cosmological constant, e.g. $\Omega_m = 0.3$, $\Omega_\Lambda = 0.7$, and with the parameters estimated by combining supernovae and CMB data (see Figure 1.4).

"Beware if you expect truth from astronomy lest you leave this field a greater fool than when you entered."

Preface to Copernicus' De revolutionibus.

Appendix A

Tables: PIZA Results for Simulations with Empty Mask

In this Appendix I present the results for the reconstructed dipoles and the comparisons between PIZA and simulations. In this case PIZA was applied to the simulations with incompltete sky coverage. Each simulation had PIZA run 5 times. Note that units of the angle to the CMB dipole are degrees, and the units of the scatter about the best fit and $x = y$ lines, and the Local Group trajectory, are kms^{-1}.

Run	1	2	3	4	5	Mean	Median	Scatter
Λ0.7/1	919	1405	1003	978	992	1059	992	231
Λ0.7/2	1292	1425	1380	1067	1158	1264	1292	150
Λ0.7/3	1766	1782	1719	1386	1569	1644	1719	167
Λ0.7/4	1246	1334	1313	1399	1395	1337	1334	63
Λ0.7/5	1349	1535	1410	1446	1544	1457	1446	83
Γ0.25/1	656	596	539	595	697	617	596	61
Γ0.25/2	349	641	1336	538	564	686	564	379
Γ0.25/3	632	575	670	583	649	622	632	41

Table A.1: Reconstructed Local Group trajectory for all simulations with empty mask.

Run	1	2	3	4	5	Mean	Median	Scatter
Λ0.7/1	0.594	0.389	0.544	0.588	0.550	0.527	0.550	0.080
Λ0.7/2	0.435	0.395	0.407	0.527	0.486	0.450	0.435	0.056
Λ0.7/3	0.355	0.352	0.365	0.452	0.400	0.385	0.365	0.042
Λ0.7/4	0.469	0.438	0.445	0.417	0.419	0.438	0.438	0.021
Λ0.7/5	0.432	0.380	0.414	0.403	0.378	0.401	0.403	0.023
Γ0.25/1	0.865	0.952	1.053	0.954	0.814	0.928	0.952	0.092
Γ0.25/2	1.769	0.963	0.462	1.147	1.064	1.081	1.064	0.468
Γ0.25/3	0.879	0.966	0.829	0.953	0.856	0.897	0.879	0.060

Table A.2: Reconstructed β for all simulations with empty mask.

Run	1	2	3	4	5	Mean	Median	Scatter
Λ0.7/1	1.195	0.783	1.095	1.123	1.107	1.061	1.107	0.160
Λ0.7/2	0.875	0.795	0.819	1.060	0.978	0.905	0.875	0.112
Λ0.7/3	0.714	0.708	0.734	0.909	0.805	0.774	0.734	0.085
Λ0.7/4	0.943	0.881	0.895	0.839	0.843	0.878	0.881	0.045
Λ0.7/5	0.869	0.765	0.883	0.811	0.761	0.808	0.811	0.046
Γ0.25/1	0.865	0.952	1.053	0.954	0.814	0.928	0.952	0.092
Γ0.25/2	1.769	0.963	0.462	1.147	1.064	1.081	1.064	0.468
Γ0.25/3	0.879	0.966	0.829	0.953	0.856	0.897	0.879	0.060

Table A.3: $\beta_{reconstructed}/\beta_{true}$ for all simulations with empty mask.

Run	1	2	3	4	5	Mean	Median	Scatter
$\Lambda 0.7/1$	30	42	23	27	23	29	27	8
$\Lambda 0.7/2$	31	36	22	44	57	37	36	13
$\Lambda 0.7/3$	12	13	15	17	9	13	13	3
$\Lambda 0.7/4$	14	17	17	16	18	16	17	2
$\Lambda 0.7/5$	21	17	19	14	41	22	19	11
$\Gamma 0.25/1$	10	17	22	22	17	18	17	5
$\Gamma 0.25/2$	10	12	112	15	18	33	15	44
$\Gamma 0.25/3$	10	12	12	15	18	26	27	5

Table A.4: Dipole misalignment angle θ_{CMB} for all simulations with empty mask.

Run	1	2	3	4	5	Mean	Median	Scatter
$\Lambda 0.7/1$	0.578	0.738	0.627	0.594	0.599	0.627	0.599	0.064
$\Lambda 0.7/2$	0.833	0.857	0.894	0.684	0.624	0.778	0.833	0.118
$\Lambda 0.7/3$	0.850	0.842	0.773	0.546	0.690	0.740	0.746	0.126
$\Lambda 0.7/4$	0.737	0.743	0.746	0.778	0.779	0.757	0.773	0.020
$\Lambda 0.7/5$	0.864	0.925	0.882	0.911	0.897	0.896	0.897	0.024
$\Gamma 0.25/1$	0.651	0.680	0.610	0.619	0.689	0.650	0.650	0.035
$\Gamma 0.25/2$	0.463	0.637	-0.176	0.607	0.561	0.418	0.561	0.339
$\Gamma 0.25/3$	0.617	0.599	0.645	0.620	0.590	0.614	0.617	0.021

Table A.5: Gradient of slope of comparison between PIZA and simulations with empty mask.

Run	1	2	3	4	5	Mean	Median	Scatter
$\Lambda 0.7/1$	5.519	9.077	4.645	5.010	4.569	5.764	5.010	1.890
$\Lambda 0.7/2$	7.010	7.746	6.196	8.024	11.04	8.003	7.746	1.840
$\Lambda 0.7/3$	3.855	4.005	4.742	6.188	4.518	4.662	4.518	0.927
$\Lambda 0.7/4$	3.831	4.249	3.609	3.988	4.093	3.954	3.988	0.246
$\Lambda 0.7/5$	5.522	5.037	5.027	4.872	9.199	5.931	5.037	1.843
$\Gamma 0.25/1$	8.179	8.939	8.840	8.818	9.033	8.762	8.840	0.337
$\Gamma 0.25/2$	6.923	4.518	28.56	4.908	5.056	9.993	5.056	10.42
$\Gamma 0.25/3$	5.096	4.929	4.660	3.487	5.845	4.803	4.929	0.857

Table A.6: Scatter about best fit line for comparison between PIZA and simulations with empty mask.

Run	1	2	3	4	5	Mean	Median	Scatter
$\Lambda 0.7/1$	8.918	10.55	7.814	8.597	8.179	8.812	8.597	1.058
$\Lambda 0.7/2$	8.588	8.862	7.436	10.21	13.03	9.625	8.862	2.144
$\Lambda 0.7/3$	5.014	5.076	6.136	8.822	6.380	6.286	6.136	1.545
$\Lambda 0.7/4$	6.515	6.747	6.213	6.202	6.358	6.407	6.358	0.229
$\Lambda 0.7/5$	5.732	4.709	5.038	4.644	9.292	5.883	5.038	0.954
$\Gamma 0.25/1$	10.12	10.74	11.18	11.11	10.03	10.64	10.74	0.540
$\Gamma 0.25/2$	13.59	9.209	36.06	9.727	10.57	15.83	10.57	11.43
$\Gamma 0.25/3$	10.09	10.28	9.274	9.081	10.80	9.905	10.09	0.716

Table A.7: Scatter about $x = y$ line for comparison between PIZA and simulations with empty mask.

Appendix B

Tables: PIZA Results for Simulations with Filled Mask

In this Appendix I present the results for the reconstructed dipoles and the comparisons between PIZA and simulations. In this case PIZA was applied to the simulations with full sky coverage. Each simulation had PIZA run 6 times. Note that units of the angle to the CMB dipole are degrees, and the units of the scatter about the best fit and $x = y$ lines, and the Local Group trajectory, are kms^{-1}.

Run	1	2	3	4	5	6	Mean	Median	Scatter
$\Lambda 0.7/1$	1723	1410	1061	1254	1365	1211	1337	1310	225
$\Lambda 0.7/2$	1286	1312	1351	1250	1299	1226	1287	1293	45
$\Lambda 0.7/3$	1706	1707	1814	1684	1669	1769	1725	1707	55
$\Lambda 0.7/4$	1219	1136	1343	1289	1232	1265	1247	1249	70
$\Lambda 0.7/5$	1349	1580	1616	1677	1153	1300	1446	1465	208
$\Gamma 0.25/1$	554	595	575	1106	698	526	676	585	219
$\Gamma 0.25/2$	621	624	781	540	711	610	648	623	85
$\Gamma 0.25/3$	803	827	771	888	787	858	822	815	44

Table B.1: Reconstructed β for all simulations with filled mask.

Run	1	2	3	4	5	6	Mean	Median	Scatter
$\Lambda 0.7/1$	0.317	0.387	0.515	0.435	0.400	0.451	0.418	0.418	0.067
$\Lambda 0.7/2$	0.437	0.429	0.416	0.450	0.433	0.450	0.436	0.435	0.013
$\Lambda 0.7/3$	0.376	0.376	0.354	0.381	0.385	0.363	0.373	0.376	0.012
$\Lambda 0.7/4$	0.479	0.514	0.435	0.453	0.474	0.462	0.470	0.468	0.027
$\Lambda 0.7/5$	0.432	0.369	0.361	0.348	0.506	0.365	0.367	0.367	0.061
$\Gamma 0.25/1$	1.024	0.954	0.987	0.513	0.813	1.079	0.897	0.971	0.208
$\Gamma 0.25/2$	0.994	0.989	0.790	1.143	0.868	1.012	0.966	0.992	0.123
$\Gamma 0.25/3$	0.692	0.672	0.720	0.625	0.706	0.647	0.677	0.682	0.036

Table B.2: Reconstructed β for all simulations with filled mask.

Run	1	2	3	4	5	6	Mean	Median	Scatter
$\Lambda 0.7/1$	0.638	0.779	1.036	0.875	0.805	0.907	0.840	0.840	0.134
$\Lambda 0.7/2$	0.879	0.863	0.837	0.905	0.871	0.905	0.877	0.875	0.026
$\Lambda 0.7/3$	0.757	0.757	0.712	0.767	0.775	0.730	0.750	0.757	0.024
$\Lambda 0.7/4$	0.964	1.034	0.875	0.811	0.954	0.930	0.945	0.942	0.054
$\Lambda 0.7/5$	0.869	0.742	0.726	0.700	1.018	0.734	0.798	0.738	0.123
$\Gamma 0.25/1$	1.024	0.954	0.987	0.513	0.813	1.079	0.897	0.971	0.208
$\Gamma 0.25/2$	0.994	0.989	0.790	1.143	0.868	1.012	0.966	0.992	0.123
$\Gamma 0.25/3$	0.692	0.672	0.720	0.625	0.706	0.647	0.677	0.682	0.036

Table B.3: $\beta_{reconstructed}/\beta_{true}$ for all simulations with filled mask.

Run	1	2	3	4	5	6	Mean	Median	Scatter
Λ0.7/1	14	11	11	20	14	23	16	14	5
Λ0.7/2	34	31	25	29	20	29	28	29	5
Λ0.7/3	9	14	11	9	12	12	11	12	2
Λ0.7/4	19	9	14	17	8	6	12	16	5
Λ0.7/5	20	27	25	42	30	14	26	29	10
Γ0.25/1	10	12	23	6	12	16	13	14	6
Γ0.25/2	18	26	63	19	19	29	29	28	17
Γ0.25/3	3	1	4	15	7	4	6	4	5

Table B.4: Dipole misalignment angle θ_{CMB} for all simulations with filled mask.

Run	1	2	3	4	5	6	Mean	Median	Scatter
Λ0.7/1	0.992	0.763	0.534	0.722	0.758	0.697	0.744	0.740	0.148
Λ0.7/2	0.776	0.751	0.790	0.760	0.789	0.764	0.772	0.770	0.016
Λ0.7/3	0.723	0.721	0.741	0.704	0.696	0.720	0.728	0.722	0.016
Λ0.7/4	0.747	0.651	0.775	0.767	0.701	0.725	0.728	0.736	0.047
Λ0.7/5	0.825	0.860	0.844	0.855	0.665	0.813	0.810	0.835	0.073
Γ0.25/1	0.589	0.608	0.602	0.850	0.630	0.607	0.648	0.608	0.100
Γ0.25/2	0.577	0.619	0.693	0.414	0.676	0.614	0.599	0.617	0.100
Γ0.25/3	0.817	0.819	0.799	0.856	0.795	0.841	0.821	0.818	0.024

Table B.5: Gradient of slope of comparison between PIZA and simulations with filled mask.

Run	1	2	3	4	5	6	Mean	Median	Scatter
$\Lambda 0.7/1$	5.593	4.362	3.360	3.905	5.783	4.497	4.583	4.430	0.946
$\Lambda 0.7/2$	6.464	7.382	6.841	5.848	6.946	6.274	6.626	6.653	0.543
$\Lambda 0.7/3$	4.736	4.486	5.104	4.587	4.019	4.799	4.622	4.662	0.363
$\Lambda 0.7/4$	4.205	5.541	3.910	3.912	5.399	4.353	4.553	4.279	0.732
$\Lambda 0.7/5$	2.860	4.851	5.825	5.789	6.534	5.843	5.284	5.807	1.303
$\Gamma 0.25/1$	9.678	10.05	10.11	13.08	9.771	9.711	10.40	9.911	1.325
$\Gamma 0.25/2$	6.627	4.761	5.708	9.375	4.610	4.635	5.953	5.235	1.854
$\Gamma 0.25/3$	5.459	5.422	6.332	5.222	6.572	4.702	5.618	5.441	0.704

Table B.6: Scatter about best fit line for comparison between PIZA and simulations with filled mask.

Run	1	2	3	4	5	6	Mean	Median	Scatter
$\Lambda 0.7/1$	6.234	6.141	7.996	6.366	7.523	6.965	6.871	6.666	0.761
$\Lambda 0.7/2$	8.033	9.042	8.263	7.684	8.408	8.000	8.238	8.148	0.465
$\Lambda 0.7/3$	5.847	5.709	5.974	6.117	5.831	6.134	5.935	5.911	0.170
$\Lambda 0.7/4$	6.909	8.615	6.554	6.409	8.209	7.448	7.357	7.179	0.901
$\Lambda 0.7/5$	3.639	5.136	6.090	6.050	8.225	6.234	5.896	6.070	1.501
$\Gamma 0.25/1$	11.89	11.73	11.67	11.44	11.12	11.58	11.57	11.63	0.267
$\Gamma 0.25/2$	10.95	9.697	8.897	15.16	8.705	9.541	10.49	9.619	2.420
$\Gamma 0.25/3$	8.246	8.038	9.016	7.617	9.384	7.706	8.335	8.142	0.717

Table B.7: Scatter about $x = y$ line for comparison between PIZA and simulations with filled mask.

Appendix C

Tables: PIZA Results for Simulations using wrong β

In this Appendix I present the results for the reconstructed dipoles and the comparisons between PIZA and simulations using the wrong inout β. In this case PIZA was applied to the simulations with full sky coverage. Each simulation had PIZA run 5 times. Note that units of the angle to the CMB dipole are degrees, and the units of the scatter about the best fit and $x = y$ lines are kms^{-1}.

Run	1	2	3	4	5	Mean	Median	Scatter
$\Lambda 0.7/4$	1377	1359	1465	1352	1551	1421	1377	86
$\Gamma 0.25/1$	662	618	643	701	682	661	662	33

Table C.1: Reconstructed Local Group displacement for simulations $\Gamma 0.25/1$ and $\Lambda 0.7/4$ using wrong input β.

Run	1	2	3	4	5	Mean	Median	Scatter
$\Lambda 0.7/4$	0.424	0.430	0.399	0.432	0.377	0.412	0.424	0.024
$\Gamma 0.25/1$	0.857	0.918	0.883	0.810	0.832	0.860	0.857	0.042

Table C.2: Reconstructed β for simulations $\Gamma 0.25/1$ and $\Lambda 0.7/4$ using wrong input β.

Run	1	2	3	4	5	Mean	Median	Scatter
$\Lambda 0.7/4$	0.853	0.865	0.803	0.869	0.759	0.830	0.853	0.048
$\Gamma 0.25/1$	0.857	0.918	0.883	0.810	0.832	0.860	0.857	0.042

Table C.3: $\beta_{reconstructed}/\beta_{true}$ for simulations $\Gamma 0.25/1$ and $\Lambda 0.7/4$ using wrong input β.

Run	1	2	3	4	5	Mean	Median	Scatter
$\Lambda 0.7/4$	17	14	17	20	15	17	17	2
$\Gamma 0.25/1$	28	25	14	30	16	23	25	7

Table C.4: PIZA reconstructed dipole misalignment angle for simulations $\Gamma 0.25/1$ and $\Lambda 0.7/4$ using wrong input β.

Run	1	2	3	4	5	Mean	Median	Scatter
$\Lambda 0.7/4$	1.228	1.175	1.249	1.137	1.297	1.217	1.228	0.063
$\Gamma 0.25/1$	0.447	0.448	0.446	0.574	0.486	0.480	0.448	0.055

Table C.5: Gradient of slope of comparison between PIZA and simulation for simulations $\Gamma 0.25/1$ and $\Lambda 0.7/4$ using wrong input β.

Run	1	2	3	4	5	Mean	Median	Scatter
$\Lambda 0.7/4$	5.454	5.265	5.598	5.827	5.830	5.595	5.598	0.244
$\Gamma 0.25/1$	6.659	6.389	5.452	10.16	6.401	7.012	6.401	2.219

Table C.6: Scatter about best fit line for comparison between PIZA and simulation for simulations $\Gamma 0.25/1$ and $\Lambda 0.7/4$ using wrong input β.

Run	1	2	3	4	5	Mean	Median	Scatter
$\Lambda 0.7/4$	7.854	7.220	8.142	7.528	8.697	7.888	7.854	0.569
$\Gamma 0.25/1$	13.13	12.96	12.59	13.05	12.57	12.86	12.96	0.263

Table C.7: Scatter about $x = y$ line for comparison between PIZA and simulation for simulations $\Gamma 0.25/1$ and $\Lambda 0.7/4$ using wrong input β.

Appendix D

References

Albrecht A., *et al.*, 1982, Phys.Rev.Lett, 48, 1437

Alcock C., *et al.*, 1993, Nature, 365, 470

Ammar R., *et al.*, 1998, Physics Letters B, 431, 209

Arfken G., 1985, Mathematical Methods for Physicists, Academic Press

Baker J.E., *et al.*, 1998, ApJ, 508, 6

Bardeen J.M, *et al.*, 1983, Phys.Rev.D, 28, 679

Beichman C.A., *et al.*, 1988, IRAS Explanatory Supplement, NASA RP-1190, Vol 1, US Government Printing Office, Washington DC

Binney J.J., Quinn T., 1991, MNRAS, 249, 678

Branchini E., Carlberg R.G., 1994, ApJ, 434, 37

Branchini E., *et al.*, 1999, MNRAS, 308, 1

Branchini E., *et al.*, 2000, in preparation

Charlier C.L.V., 1925, PASP, 37, 177

Cole S., *et al.*, 1997, MNRAS, 289, 37

Croft R.A.C., Gaztañaga, E., 1997, MNRAS, 285, 793 (CG97)

da Costa L.N., *et al.*, 2000, AJ, in press, astro-ph/9912201

Davis M., Huchra J., 1982, ApJ, 254, 437

Davis M., *et al.*, 1991, ApJ, 372, 394

Davis M., Nusser A., Willick J., 1996, ApJ, 473, 22

Davis M., Peebles P.J.E., 1983, ARA&A, 21, 109

Dekel A., 1991, In Observational Tests of Cosmological Inflation, eds Shanks T. *et al.*, NATO ASI Series

Dekel A., 1993, ApJ, 412, 1

Dekel A., 1994, ARA&A, 32, 371

Dekel A., Lahav O., 1999, ApJ, 520, 24

Dekel A., *et al.*, 1999, ApJ, 522, 1

de Vaucouleurs G., 1953, AJ, 58, 30

de Vaucouleurs G., 1958, AJ, 63, 252

de Vaucouleurs G., 1986, ApJ, 308, 487

Efstathiou G.P., 1990, in Physics of the Early Universe, eds., Peacock J.A., Heavens A.F., Davies A.T.

Ferrarese L. *et al.*, 2000, In Towards an Understanding of Cosmic Flows, Victoria, July 1999, eds Courteau, S., Strauss, M., Willick, J., PASP

Fisher K.B., 1992, Ph.D. thesis, University of California, Berkeley

Fisher K.B., Scharf C.A., Lahav O., 1994, MNRAS, 266, 219

Fisher K.B., *et al.*, 1995, MNRAS, 272, 885

Giovanelli R., *et al.*, 1998, ApJ, 505, 91

Giavalisco M., *et al.*, 1993, ApJ, 411, 9

Gramman M., 1993a, ApJ, 405, 449

Gramman M., 1993b, ApJ, 405, L47

Guth A.H., 1981, Phys.Rev.D, 23, 347

Hamilton A.J.S., 1998, in Hamilton D., ed., Ringberg Workshop on Large-Scale Structure. The Evolving Universe. Kluwer, Dordrecht

Hamilton A.J.S., Tegmark M., Padmanabhan N., 2000, submitted to MNRAS, astro-ph/0004334

Heavens A.F., Taylor A.N., 1997, MNRAS, 290, 456

Hill E.H., 1954, Am. J. Phys, 22, 211

Hubble E.P., 1925, ApJ, 62, 409

Hubble E.P., 1926, ApJ, 64, 321

Hubble E.P., 1929, Proc. Nat. Acad. Sci., 15, 168

Hudson M.J., 1993, MNRAS, 265, 72

Humason M.L., Mayall N.U., Sandage A.R., 1956, AJ, 61, 97

Juszkiewicz R., Vittorio N., Wyse R.F.G., 1990, ApJ, 349, 408

Kaiser N., 1984, ApJ, 284, L9

Kaiser N., 1987, MNRAS, 227, 1

Kaiser N., Lahav O., 1989, MNRAS, 237, 129

Kaiser N., *et al.*, 1991, MNRAS, 252, 1

Kaiser N., Stebbins A., 1991, In Large Scale Structures and Peculiar Motions in the Universe, ASP Conference Series, Vol 15, eds Latham D.W., da Costa L.N.

Lahav O., Kaiser N., Hoffman Y., 1990,ApJ, 352, 448

Lahav O., *et al.*, 1994, ApJ, 423, L93

Lawrence A., *et al.*, 1999, MNRAS, 308, 897

Liddle A.R., Lyth D., 1993, Physics Reports, 231, 1

Lynden-Bell D., *et al.*, 1988, ApJ, 326, 19

Mann R.G, Saunders W., Taylor A.N., 1996, MNRAS, 279, 636

Meiksin A., Davis M., 1986, AJ, 91, 191

Monaco P., Efstathiou G., 1999, MNRAS, 308, 763

Moshir M., *et al.*, 1989, Explanatory Supplement to the IRAS FSS

Narayanan V.K., Croft R.A.C., 1999, ApJ, 515, 471

Narayanan V.K., Weinberg D.H., 1998, ApJ, 508, 440

Narayanan V.K., *et al.*, 1999, astro-ph/9910229

Nusser A., Dekel A., 1992, ApJ, 391, 443

Nusser A., Branchini E., 2000, MNRAS, 313, 587

Nusser A., *et al.*, 2000, submitted to MNRAS, astro-ph/006062

Öpik E., 1922, ApJ, 55, 406

Peacock J.A., Heavens A.F., 1985, MNRAS, 217, 805

Peacock J.A., 1992, MNRAS, 258, 581

Peacock J.A., 1996, The Structure of the Universe, Summer School, Leiden, July 1995

Peacock J.A., 1999, Cosmological Physics, Cambridge University Press

Peebles P.J.E., 1976, ApJ, 205, 318

Peebles P.J.E., 1980, The Large Scale Structure of the Universe, Princeton University Press, Princeton, NJ

Peebles P.J.E., 1989, ApJ, 344, L53

Peebles P.J.E., 1990, ApJ, 362, 1

Peebles P.J.E., 1993, Principles of Physical Cosmology, Princeton University Press, Princeton, NJ

Peebles P.J.E., 1994, ApJ, 429, 43

Peebles P.J.E., 1995, ApJ, 449, 52

Penzias A.A., Wilson R.W., 1965, ApJ, 142, 419

Perlmutter S., *et al.*, 1999, ApJ, 517, 565

Regös E., Szalay A.S., 1989, ApJ, 345, 627

Riess A.G., *et al.*, 1998, AJ, 116, 1009

Rowan-Robinson M., *et al.*, 1990, MNRAS, 247, 1

Rowan-Robinson M., *et al.*, 1991, MNRAS, 253, 483

Rowan-Robinson M., *et al.*, 2000, MNRAS, 314, 375

Sandage A.R., 1978. AJ, 83, 904

Sandage A.R., Tammann, G., 1985, In Supernovae as distance indicators; Proceedings of the workshop Cambridge MA, Springer-Verlag

Santiago B.X., *et al.*, 1995, ApJ, 461, 38

Saunders W. *et al.*, 1995, In Wide Field Spectroscopy and the Distant Universe, eds Maddox S.J., Aragon-Salamanca A., World Scientific, Singapore

Saunders W., *et al.*, 1999a, In Towards an Understanding of Cosmic Flows, Victoria, July 1999, eds Courteau, S., Strauss, M., Willick, J., PASP

Saunders W., *et al.*, 1999b, In Towards an Understanding of Cosmic Flows, Victoria, July 1999, eds Courteau, S., Strauss, M., Willick, J., PASP

Saunders W., Ballinger W.E., 2000, In 'The Hidden Universe', procs Guanajuarto conference 2/00. ASP Conference series, eds R.C. Kraan-Korteweg, P.A. Henning and H. Andernach, astro-ph/0005606

Saunders W., *et al.*, 2000, submitted to MNRAS, astro-ph/0001117

Saunders W., *et al.*, 2000, In 'The Hidden Universe', procs Guanajuarto conference 2/00. ASP Conference series, eds R.C. Kraan-Korteweg, P.A. Henning and H. Andernach, astro-ph/0006005

Schmoldt I., *et al.*, 1999a, AJ, 118, 1146

Schmoldt I., *et al.*, 1999b, MNRAS, 304, 893

Scharf C., Hoffman Y., Lahav O., Lynden-Bell D., 1992, MNRAS, 256, 229

Schramm D.N., 1991, Physica Scripta, T36, 22

Schramm D.N., Turner M.S., 1998, Rev. Mod. Phys., 70, 303

Shapley H., Ames A., 1932, Annals of the Harvard College Observatory, 88, 41

Sharpe J., *et al.*, 2000, submitted to MNRAS

Shaya E.J., Peebles P.J.E., Tully R.B., 1995, ApJ, 454, 15

Smoot G.F., *et al.*, 1977, Phys.Rev.Lett, 39, 898

Smoot G.F., 1991, In Observational Tests of Cosmological Inflation, eds Shanks T. *et al.*, NATO ASI Series

Smoot G.F., *et al.*, 1992, ApJ, 396, L1

Strauss M.A., *et al.*, 1990,, ApJ, 361, 49

Strauss M.A., *et al.*, 1992a, ApJS, 83, 29

Strauss M.A., *et al.* 1992b, ApJ, 385, 421

Strauss M.A., *et al.*, 1992c, ApJ, 397, 395

Tadros H., *et al.*, 1999, MNRAS, 305, 289

Taylor A.N., Hamilton, A.J.S., 1996, MNRAS, 282, 767

Taylor A.N., Rowan-Robinson, M., 1992, Nature, 359, 396

Taylor A.N., Rowan-Robinson, M., 1993, MNRAS, 265, 809

Taylor A.N., Valentine, H.E.M., 1999, MNRAS, 306, 491 (TV99)

Tegmark M., *et al.*, 1998, submitted to ApJ, astro-ph/9805117

Tegmark M., 1999, ApJ, 514, 69

Teodoro L., *et al.*, 1999, astro-ph/9908358

Trimble V., 1987, ARA&A, 25, 425

Tully R.B., Fisher J.R., 1977, A&A, 54, 661

Turner M.S., 1997, astro-ph/9704062

Valentine H.E.M., Saunders W., Taylor A.N., 1999, In Towards an Understanding of Cosmic Flows, Victoria, July 1999, eds Courteau, S., Strauss, M., Willick, J., PASP

Valentine H.E.M., Saunders W., Taylor A.N., 2000, submitted to MNRAS

Webster M., Lahav O., Fisher K., 1997, MNRAS, 287, 425

Weinberg D.H., 1992, MNRAS, 254, 315

Willick J.A., *et al.*, 1997, ApJS, 109, 333

Yahil A., Tammann, G., Sandage, A.R., 1977, ApJ, 217, 903

Yahil A., Sandage A.R., Tammann G.A., 1980, ApJ, 242,448

Yahil A., *et al.*, 1986, ApJ, 301, L1

Yahil A., *et al.*, 1991, ApJ, 372, 380

Zel'dovich Ya.B., 1970, A&A, 5, 84

Appendix E

Reconstructing PSCz with a Generalized PIZA

This Appendix contains a copy of the recently published MNRAS paper "Reconstructing PSCz with a Generalized PIZA", which includes some of the material presented in Chapters 3, 4 and 5.

Mon. Not. R. Astron. Soc. **319**, L13–L17 (2000)

Reconstructing the *IRAS* Point Source Catalog Redshift Survey with a generalized PIZA

Helen Valentine,* Will Saunders and Andy Taylor
Institute for Astronomy, University of Edinburgh, Royal Observatory, Blackford Hill, Edinburgh EH9 3HJ

Accepted 2000 October 11. Received 2000 October 5; in original form 2000 June 6

ABSTRACT

We present a generalized version of the path interchange Zel'dovich approximation (PIZA), for use with realistic galaxy redshift surveys. PIZA is a linear particle-based Lagrangian method which uses the present-day positions of galaxies to reconstruct both the initial density field and the present-day peculiar velocity field. We generalize the method by mapping galaxy positions from redshift space to real space in the Local Group frame, and take the selection function into account by minimizing the mass-weighted action. We have applied our new method to mock galaxy catalogues, and find that it offers an improvement in the accuracy of reconstructions over linear theory. We have applied our method to the all-sky *IRAS* Point Source Catalog Redshift Survey (PSCz). Applying PIZA to PSCz, we are able to obtain the peculiar velocity field, the dipole, bulk velocities, and the distortion parameter. From the dipole, we find that $\beta = 0.51 \pm 0.14$. We compare the PSCz bulk velocity with that of the Mark III velocity survey, and conclude that $\beta = 0.5 \pm 0.15$. We compare the PSCz dipole with that of the SFI Tully Fisher Survey and find that $\beta = 0.55 \pm 0.1$.

Key words: cosmology: theory – large-scale structure of Universe.

1 INTRODUCTION

Cosmological density and velocity fields may be reconstructed using the radial velocity information from a galaxy redshift survey. To do this, assumptions must be made about the way in which the peculiar velocity field is produced, the relations between the velocity and density fields, and the relationship between galaxies and the underlying mass distribution. The reconstructed fields may then be compared with the directly measured fields, e.g. from a peculiar velocity survey, and used to place constraints on cosmological parameters.

The structures seen in the Universe today formed by the growth via gravitational instability of small density perturbations present in the early Universe. The growth and evolution of these structures may be studied using methods of two types: Eulerian methods which solve the gravitational instability equations (see Peebles 1980); and Lagrangian methods which follow individual galaxy displacements. These methods may be used to deduce the velocity field from the density field and vice versa.

Eulerian methods include those that use linear perturbation theory applied to the gravitational instability equations. The iterative reconstruction methods of Yahil et al. (1991), who studied the 1.2-Jy redshift survey, and Kaiser et al. (1991) and Taylor & Rowan-Robinson (1993), who studied the QDOT redshift survey, use this method to reconstruct the peculiar velocity field from galaxy redshift surveys. Branchini et al. (1999) used a similar method to reconstruct the peculiar velocity of the PSCz.

Lagrangian methods include the Zel'dovich approximation (ZA: Zel'dovich 1970), which was suggested as a way to study the evolution of structure in the non-linear regime. Within the ZA the linear displacement field of galaxies is extrapolated from initial, Lagrangian coordinates to final, Eulerian coordinates. The galaxy peculiar velocity is simply the time derivative of the linear displacement.

The use of Hamilton's principle, that the action is minimized during the evolution of a collection of particles under gravity, was introduced as a reconstruction method to cosmology by Peebles (1989) and developed by Peebles (1994, 1995), Shaya, Peebles & Tully (1995); Giavalisco et al. (1993) and Susperregi & Binney (1994). Sharpe et al. (1998) recently used Peebles' numerical action method to reconstruct the peculiar velocities of PSCz galaxies within $cz = 2000\,\mathrm{km\,s^{-1}}$, while Monaco & Efstathiou (1999) have developed ZTRACE, an iterative reconstruction method based on Lagrangian perturbation theory.

A method combining the ZA and the least action principle is the path interchange Zel'dovich approximation (PIZA) of Croft & Gaztañaga (1997, hereafter CG97). They showed that, using the ZA, the least action solution is that which minimizes the total mean square particle displacement between initial and final galaxy positions. Hence, given a set of final galaxy positions and a random distribution of initial coordinates, the least action trajectories are those that minimize the total displacement.

Previously PIZA has been used to reconstruct the initial density

* E-mail: hemv@roe.ac.uk

fields from simulated real-space density fields (CG97; Narayanan & Croft 1999). Here we wish to apply PIZA to a redshift survey in order to reconstruct the peculiar velocity and real-space density fields. We apply our new PIZA method to the Point Source Catalog Redshift survey (PSCz: Saunders et al. 2000), a survey of 15 000 *IRAS* galaxies to a flux limit of 0.6 Jy at 60 μm, covering 84 per cent of the sky.

The outline of the paper is as follows. We review PIZA in Section 2. In Section 3 we describe the problems encountered when applying PIZA to redshift surveys, and the generalizations that we have made to the method in order to overcome these problems. In Section 4 we test PIZA using PSCz-like simulations, and compare the predictions for the fields with those given by linear theory. In Section 5 we apply our new method to the PSCz survey. In Section 6 we discuss our results and present our conclusions.

2 PATH INTERCHANGE ZEL'DOVICH APPROXIMATION

Here we briefly review the original PIZA method. For more details, we refer the reader to CG97.

We define a galaxy position in terms of its initial position and displacement:

$$\boldsymbol{r}(\boldsymbol{q},t) = \boldsymbol{q} + \boldsymbol{\xi}(\boldsymbol{q},t), \tag{1}$$

where $\boldsymbol{r}$is the Eulerian coordinate, $\boldsymbol{q}$is the initial Lagrangian coordinate and $\boldsymbol{\xi}$is the galaxy displacement.

CG97 (section 2.1) showed that the action is proportional to the mass-weighted squared particle displacement,

$$S = \sum_i m_i \xi_i^2, \tag{2}$$

where m_i is the mass of the ith particle. The least action principle then requires the minimization of this quantity. In CG97 it is assumed that the galaxies are of equal mass, simplifying the minimization of equation (2). Assuming that the final, Eulerian galaxy positions are known, the initial positions are drawn from a homogeneous distribution and assigned at random to the Eulerian galaxy positions. We shall refer to the initial objects as PIZA particles. It is not necessary that there be only one particle per galaxy; CG97 found that increasing the number of particles per galaxy improved the accuracy of the reconstruction. Applying PIZA is very simple. Two galaxies are then picked at random and their PIZA particles interchanged. If this decreases S the interchange is kept, and if not the particles are swapped back. Interchanges are attempted until the rate of change of S with attempted swaps, the cooling rate, is very low.

3 PIZA WITH REALISTIC GALAXY REDSHIFT SURVEYS

The PIZA method cannot be immediately applied to a realistic galaxy redshift survey. In the first instance the radial positions of galaxies are estimated from their redshift, which introduces distortions in galaxy positions owing to the peculiar velocities of galaxies. This distortion will depend on the rest frame of the observer, which we shall assume is the Local Group frame. To apply PIZA we must first deal with this distortion. Secondly, most galaxy redshift surveys are flux-limited, so that the observed number of galaxies drops off with distance as only the brightest galaxies can be seen. This affects the number density of galaxies, which must now be regarded as sampling the total galaxy population. This means that the galaxies must be assigned effective masses which must be included in the PIZA minimization. Finally, the sky coverage of galaxies may not be complete and some way must be included in the reconstruction to account for regions of incompleteness. In this section we shall discuss each of these effects in turn.

3.1 PIZA in redshift space

The peculiar motions of galaxies, $\boldsymbol{v}$, mean that in the cosmic microwave background (CMB) frame the radial coordinate in redshift space is a mixture of spatial position and projected velocity,

$$\boldsymbol{s}(\boldsymbol{r},t) = \boldsymbol{r} + [\hat{\boldsymbol{r}} \cdot \boldsymbol{v}(\boldsymbol{r},t)]\hat{\boldsymbol{r}}, \tag{3}$$

where $\boldsymbol{s}$is the redshift position. In the ZA the velocity field of galaxies is a linear extrapolation, and related to the displacement field by

$$\boldsymbol{v} = \dot{\boldsymbol{\xi}} = f(\Omega)\boldsymbol{\xi}, \tag{4}$$

where $f \equiv \mathrm{d}\ln\delta/\mathrm{d}\ln a \approx \Omega^{0.6}$ is the growth rate of linear perturbations (Peebles 1980). If galaxies are a locally biased representation of the density field then $\delta_{\mathrm{gal}} = F[\delta_{\mathrm{mass}}] \approx b\delta_{\mathrm{mass}}$ to first order. We can then define a galaxy displacement field which is related to the velocity field by

$$\boldsymbol{v} = \beta\boldsymbol{\xi}, \tag{5}$$

where

$$\beta = \frac{f(\Omega)}{b} \tag{6}$$

is the redshift distortion parameter. The redshift-space displacement field is related to the real-space displacement field by (Taylor & Hamilton 1996)

$$\xi_i^s = \mathcal{P}_{ij}\xi_j, \tag{7}$$

where $\mathcal{P}_{ij} \equiv \delta_{ij}^{\mathrm{K}} + \beta\hat{r}_i\hat{r}_j$ is the redshift-space projection tensor, and δ_{ij}^{K} is the Kronecker tensor. Inverting equation (7) gives (Taylor & Valentine 1999)

$$\xi_i = \mathcal{P}_{ij}^{-1}\xi_j^s, \tag{8}$$

where

$$\mathcal{P}_{ij}^{-1} \equiv \delta_{ij}^{\mathrm{K}} - \frac{\beta}{1+\beta}\hat{r}_i\hat{r}_j \tag{9}$$

is the inverse redshift-space projection tensor. Squaring this gives us the expression for the linear displacement field in terms of linear redshift displacements and β:

$$\xi^2 = \xi^{s^2} - \left[1 - \frac{1}{(1+\beta)^2}\right]\xi_r^{s^2}, \tag{10}$$

where $\xi_r^s = \boldsymbol{\xi}\cdot\hat{\boldsymbol{r}}$ is the displacement vector in redshift space projected along the line of sight. Thus we must assume an a priori value for β.

3.2 PIZA with local group frame redshifts

Redshift-space distortions should also take into account the motion of the observer, in this case the Local Group motion. The

transformation from real to redshift space in the Local Group rest frame is (Taylor & Valentine 1999)

$$\xi_i = \mathcal{P}_{ij}^{-1}\xi_j^{s,\mathrm{LG}} + (\delta_{ij}^{\mathrm{K}} - \mathcal{P}_{ij}^{-1})\xi_j(\mathbf{0}), \tag{11}$$

where the super- or subscript LG denotes a variable measured in the Local Group frame, and $\boldsymbol{\xi}(\mathbf{0})$ is the displacement of the Local Group. The real-space displacement field can now be expressed in terms of redshift displacements in the Local Group frame as

$$\xi^2 = \xi_{\mathrm{LG}}^{s^2} - \xi_{r,\mathrm{LG}}^{s^2} + \frac{[\beta\xi_r(\mathbf{0}) + \xi_{r,\mathrm{LG}}^s]^2}{(1+\beta)^2}. \tag{12}$$

To apply equation (12) we require the displacement of the Local Group. We find this by placing a galaxy representing the Local Group at the origin and using its displacement as the Local Group displacement.

3.3 Incomplete sky coverage

The incomplete sky coverage may cause problems with PIZA, as with other reconstruction methods, since in these regions we do not know the true galaxy distribution. A number of choices for filling in these regions present themselves. One could populate the incomplete regions randomly on the sky, assuming no information, or leave the regions empty of both particles and galaxies. These are equivalent except for particles adjacent to the mask. Alternatively, one could interpolate across using correlations in the density field to fill in the gaps. In reconstructing PSCz we use the Fourier interpolation scheme of Saunders et al. (1999) which allows optimal, non-linear interpolation across these regions.

3.4 PIZA with a selection function

In a flux-limited survey, the number density of survey objects decreases with increasing redshift, as galaxies at greater distances must be brighter to be seen above the flux limit. This is quantified by the survey selection function, $\phi(r)$, the expected number of galaxies seen at distance r above the flux limit in the absence of clustering.

In order to account for this change in the number density with distance, we pick initial PIZA particles with the same selection function as the galaxies. To take account of those galaxies that fall below the flux limit, we assign each galaxy a mass of $1/\phi(r)$ and each PIZA particle a mass of

$$m_i = 1/[\nu\phi(r_i)], \tag{13}$$

where ν is the mean number of particles assigned per galaxy. We use $\nu = 10$ in order to reduce the shot noise in the reconstruction. Equations (12) and (13) are used in equation (2) to minimize the displacement squared.

With the inclusion of particle masses, it is possible for S to decrease but light particles to acquire unrealistically large trajectories. We have therefore added an additional constraint that the rms displacement squared in redshift space should also decrease.

3.5 Second-order effects

The masses that we have assigned to the galaxies are based on the selection function at their redshift distance. Because of peculiar velocities, these can be in error. We therefore developed a modified version of PIZA, MASSPIZA, whereby, after PIZA is run, particles are randomly reassigned from galaxies where the mass has been overestimated to those where it has been underestimated. PIZA is then rerun and the whole process iterated until the masses are acceptable and the trajectories minimized. Unfortunately, this procedure is in general unstable to the rocket effects described by Kaiser (1987). In the section below, we show that PIZA without mass reassignment gives acceptable results in comparison with simulations; the agreement is in general not improved by the second, MASSPIZA stage. Therefore we have not incorporated it in any of the results quoted in this paper.

4 TESTS ON SIMULATIONS

In order to test the new PIZA method, we have applied it to a set of PSCz-like mock catalogues. For more details of these mock catalogues, we refer the reader to Branchini et al. (in preparation). The catalogues are of two cold dark matter (CDM) cosmologies, a critical model, ($\Omega_{\mathrm{matter}} = 1$, $\beta = 1$, with $\Gamma = 0.25$) and a flat model ($\Omega_{\mathrm{matter}} = 0.3$ and $\Omega_\Lambda = 0.7$, $\beta = 0.50$), and are limited to $v < 15\,000\,\mathrm{km\,s^{-1}}$. We tested the reconstruction of the radial peculiar velocity field, comparing it with that of the simulation. To compare the fields, the peculiar velocities were binned in real space and smoothed with a Gaussian smoothing kernel. We have also compared the PIZA reconstructions with the linear theory reconstructions for the mock catalogues from Branchini et al. (in preparation) Fig. 1 shows typical results from comparing PIZA and linear theory reconstructions with the simulations. The dot–dashed line indicates the least-squares fit to the data. The velocity fields were smoothed with a Gaussian of radius $20\,h^{-1}$ Mpc. With a smaller smoothing radius, say of $5\,h^{-1}$ Mpc, the slope of the least-squares fit is similar, but the scatter about that slope is approximately twice as large.

We find that generally the gradient reconstructed by PIZA is less biased than that reconstructed by linear theory, but that the scatter is somewhat worse. This is probably one of the limitations of PIZA, as the scatter in redshift-space reconstructions produced by PIZA is quite large (see CG97). As seen in Fig. 1, PIZA tends to underestimate the reconstructed velocities. Both this underestimation and the large scatter are due to the effects of the selection function, which are not taken into account.

As stated above, we must assume an a priori value for β. The reconstruction works well for any sensible value of β. We find that PIZA works better for low-density models as they are less dynamically evolved.

The accuracy of the reconstruction varies between different sets

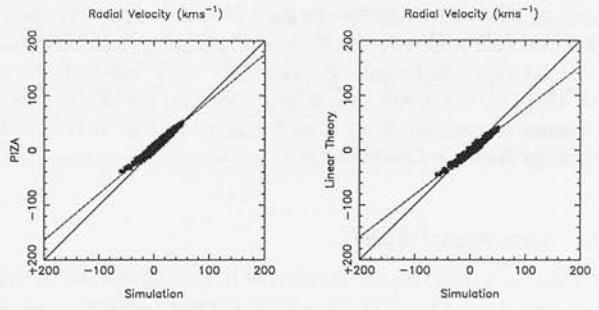

Figure 1. Typical simulation results: comparison of PIZA and linear theory reconstructions. The left-hand panel shows PIZA radial velocities compared with simulation; the right-hand panel shows linear theory compared with simulation. Velocities were smoothed with a Gaussian of radius $20\,h^{-1}$ Mpc. The dot–dashed line indicates the least-squares fit.

Table 1. Results from tests on simulations. Λ0.7 denotes the Ω_Λ model, and Γ0.25 the critical model. P denotes simulations with PSC*z* sky coverage and 4π simulations with full sky coverage.

Mock	β_R	Scatter	θ_{CMB}	Slope	Scatter
Λ0.7 P	0.42	0.07	22	0.76	0.10
Γ0.25 P	0.95	0.27	26	0.61	0.14
Λ0.7 4π	0.43	0.05	14	0.74	0.04
Γ0.25 4π	0.84	0.18	13	0.65	0.13

of initial conditions (i.e. PIZA particles) owing to the random positioning of particles. The resulting scatter in the reconstructed parameters is shown in Table 1. There is also a scatter between reconstructions using the same initial conditions, owing to the random swaps made by PIZA. This is around the same size as that arising from random initial conditions, and probably reflects the fact that there is not a simple minimum for the action, S, but that the configuration space is complicated by the particle discreteness. We estimate β from the trajectory of the Local Group galaxy using equation (5) and assuming the magnitude of the CMB dipole. Table 1 shows the reconstructed β, the dipole misalignment angle, and the slope of the peculiar velocity comparison, with the scatter arising from different initial conditions. We have tested the effects of having the Galactic plane filled or empty. This is important for PSC*z* as we know that there are large structures, such as the Great Attractor, in the plane. With the simulations we have tested PIZA using 4π sky coverage, and with the PSC*z* mask applied. With the mask empty we find that the average misalignment angle is 24°, and with full-sky coverage it is 14°.

5 RECONSTRUCTING PSC*z*

We have applied our new PIZA method to the PSC*z* survey (Saunders et al. 2000) out to $R = 300\,h^{-1}$ Mpc, using the parametrized *IRAS* selection function of Mann, Saunders & Taylor (1996). For the reconstructions we have filled the masked regions with interpolated galaxies.

Fig. 2 shows the reconstructed PSC*z* velocity field in a slice $20\,h^{-1}$ Mpc thick centred on the Supergalactic plane. Fig. 3 shows the same slice out to $50\,h^{-1}$ Mpc. The arrows show the galaxy trajectories, with the arrows starting at the initial positions and the arrow heads at the galaxy real-space positions. Generally the velocity field at the edge of the volume is quiet, apart from flow towards Shapley at (120, 90) and the void at (0, −120). The Coma cluster is seen at (0, 70). The Cetus wall extends northwards from (0, −100) towards Perseus–Pisces at (50, −20). Virgo is seen at (0, 10). The Great Attractor is at (−40, 20), and we see little evidence of backfall on to it on the opposite side to the Great Attractor from the Local Group.

5.1 Cosmological dipole

We find an average dipole direction of $(l, b) = (264^\circ.4, 41^\circ.7)$. We find that $\beta = 0.51 \pm 0.14$. This error has three sources: random errors caused by PIZA (see Section 4); misalignment between the reconstructed and CMB dipoles; and cosmic variance and shot noise on the reconstructed dipole (Taylor & Valentine 1999). A similar result is found by using only the z-component of the dipole.

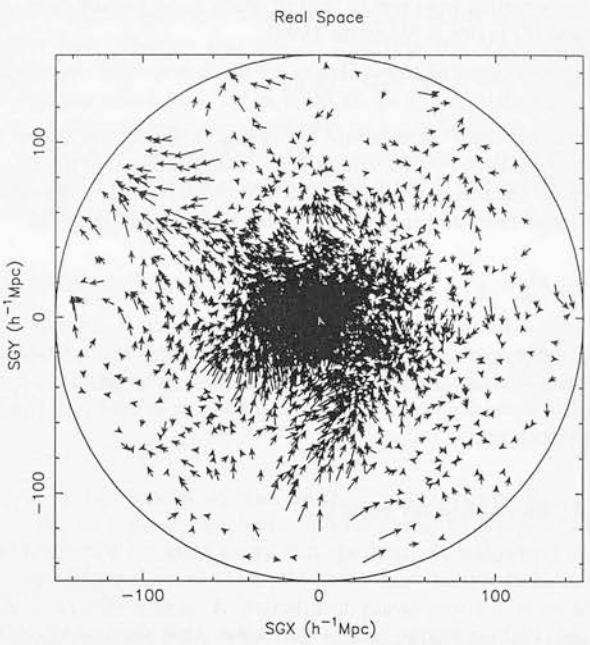

Figure 2. PSC*z* velocity field within $150\,h^{-1}$ Mpc.

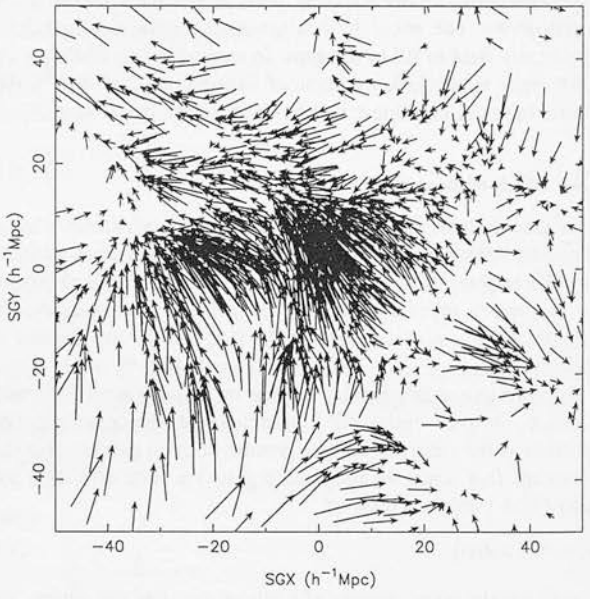

Figure 3. PSC*z* velocity field within $50\,h^{-1}$ Mpc.

5.2 Radial velocity field

The reconstructed dipole and bulk flows are shown in Fig. 4. We have compared our bulk flows with those from the Mark III Catalogue (Willick et al. 1997) and the linear theory PSC*z* reconstruction (Branchini et al. 1999), and conclude that $\beta = 0.5 \pm 0.15$. This is consistent with the results of Tadros et al. (1999) based on the measurement of the degree of redshift-space distortion in the PSC*z*.

5.3 Comparison with the SFI Tully Fisher Survey

We have undertaken a comparison of the reconstructed PSC*z*

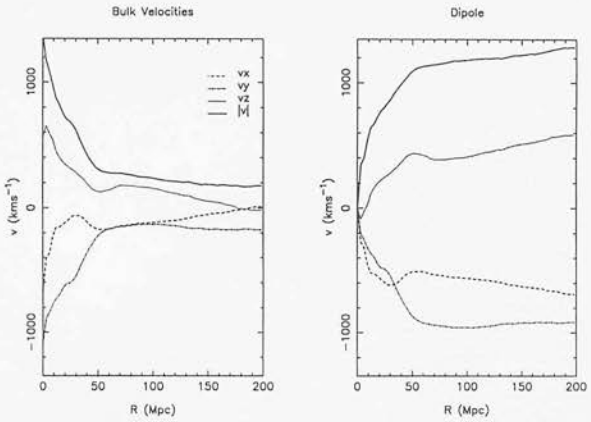

Figure 4. PSCz bulk velocities and dipole within $150\,h^{-1}$ Mpc.

Table 2. SFI versus PSCz peculiar velocities with respect to shells of galaxies. PSCz reconstruction assumes $\beta = 0.5$.

Shell	$V_{\rm SFI}$	$(l, b)_{\rm SFI}$	$V_{\rm PIZA}$	$(l, b)_{\rm PIZA}$
0–2000	270±80	(245, 49)±19	372	(228, 45)
1500–3500	410±69	(255, 21)±12	430	(254, 56)
2500–4500	620±76	(255, 15)±11	485	(271, 50)
3500–5500	585±92	(265, 19)±13	550	(281, 39)
4500–6500	544±98	(270, 16)±15	503	(279, 34)

velocity field with the SFI data set of peculiar velocities of spiral galaxies (Giovanelli et al. 1998). We have calculated the average peculiar velocity, with respect to the Local Group, of galaxies in redshift slices, to be as closely as possible comparable to Giovanelli et al. We find reasonable agreement in amplitude, although there are significant differences in direction, for $\beta = 0.55 \pm 0.1$. Table 2 shows the average peculiar velocity in shells for PIZA and SFI.

6 DISCUSSION

We have presented a generalized version of the PIZA method for reconstructing velocity and density fields from galaxy surveys. These modifications to the original method are necessary if it is to be applied to realistic galaxy redshift surveys with a selection function. We have used the inverse redshift space operator of Taylor & Valentine (1999) to write the mean square particle displacement in terms of the redshift-space positions of galaxies, and to map redshifts from the Local Group rest frame to real space. The PIZA particles obey the same selection function as the galaxies. Doing this we can reconstruct the real-space density field, the galaxy initial positions and the peculiar velocity field.

We have tested the method using PSCz-like CDM simulations, testing the reconstruction of the real-space positions and the peculiar velocities. We have also compared our reconstructions with linear theory reconstructions of the simulations. We have applied our method to the PSCz survey, and reconstructed the local velocity field out to $300\,h^{-1}$ Mpc from the Local Group, and have calculated the bulk flow and the dipole. We find the reconstructed dipole to be $16° \pm 4°$ away from the CMB dipole. From comparison between the PIZA reconstruction and the Mark III bulk flow, we find that $\beta = 0.5 \pm 0.15$, while from a dipole analysis of the PIZA reconstruction we find that $\beta = 0.51 \pm 0.14$.

ACKNOWLEDGMENTS

HV thanks PPARC for a studentship. We thank Enzo Branchini for the simulations and linear theory reconstructions.

REFERENCES

Branchini E. et al., 1999, MNRAS, 308, 1
Croft R. A. C., Gaztañaga E., 1997, MNRAS, 285, 793 (CG97)
Giavalisco M., Mancinelli B., Mancinelli P. J., Yahil A., 1993, ApJ, 411, 9
Giovanelli R., Haynes M. P., Freudling W., da Costa L. N., Salzer J. J., Wegner G., 1998, ApJ, 505, L91
Kaiser N., 1987, MNRAS, 227, 1
Kaiser N., Efstathiou G., Saunders W., Ellis R., Frenk C., Lawrence A., Rowan-Robinson M., 1991, MNRAS, 252, 1
Mann R. G., Saunders W., Taylor A. N., 1996, MNRAS, 279, 636
Monaco P., Efstathiou G., 1999, MNRAS, 308, 763
Narayanan V. K., Croft R. A. C., 1999, ApJ, 515, 471
Peebles P. J. E., 1980, The Large Scale Structure of the Universe. Princeton Univ. Press, Princeton, NJ
Peebles P. J. E., 1989, ApJ, 344, L53
Peebles P. J. E., 1994, ApJ, 429, 43
Peebles P. J. E., 1995, ApJ, 449, 52
Saunders W. et al, 1999, in Courteau S., Strauss M., Willick J., eds, ASP Conf. Ser. Vol. 201, Towards an Understanding of Cosmic Flows. Astron. Soc. Pac., San Francisco, p. 228
Saunders W. et al., 2000, MNRAS, 317, 55
Sharpe J. et al., 1998, in Giuricin G., Mezzetti M., Salucci P., eds, ASP Conf. Ser. Vol. 176, Observational Cosmology: The Development of Galaxy Systems. Astron. Soc. Pac., San Francisco, p. 280
Shaya E. J., Peebles P. J. E., Tully R. B., 1995, ApJ, 454, 15
Susperregi M. P., Binney J. J., 1994, MNRAS, 271, 719
Tadros H. et al., 1999, MNRAS, 305, 527
Taylor A. N., Hamilton A. J. S., 1996, MNRAS, 282, 767
Taylor A. N., Rowan-Robinson M., 1993, MNRAS, 265, 809
Taylor A. N., Valentine H. E. M., 1999, MNRAS, 306, 491
Willick J. A., Courteau S., Faber S. M., Burstein D., Dekel A., Strauss M. A., 1997, ApJS, 109, 333
Yahil A., Strauss M. A., Davis M., Huchra J. P., 1991, ApJ, 372, 380
Zel'dovich Ya. B., 1970, A&A, 5, 84

This paper has been typeset from a TEX/LATEX file prepared by the author.